1995

High Temperature X-ray Diffraction Investigation Of The Beta-(bismuth(2) Oxygen(3))(1-x)(strontium Oxide)(x) Solid Solution

Edward Andrew Payzant

High Temperature X-Ray Diffraction Investigation of the β-$(Bi_2O_3)_{1-x}(SrO)_x$ Solid Solution

by

Edward Andrew Payzant

Faculty of Engineering Science

Department of Materials Engineering

Submitted in partial fulfillment
of the requirements for the degree of
Doctor of Philosophy

Faculty of Graduate Studies
The University of Western Ontario
London, Ontario
February 1995

ISBN 0-315-99272-7

ABSTRACT

To investigate the controversial $\beta_1 \leftrightarrow \beta_2$ phase transformation in the β-$(Bi_2O_3)_{1-x}(SrO)_x$ phase, a series of compositions across the phase were prepared by conventional grinding, pressing and firing ceramic techniques. Electrical conductivity measurements demonstrated that the samples were comparable to those used in other laboratories. X-ray diffraction analysis confirmed that the cations are located on a hexagonal sublattice, but details of the anion sublattice could not be resolved, because of the low X-ray scattering factor of O^{2-}.

The compositional dependence of the lattice parameters of the hexagonal crystal structure of the β-$(Bi_2O_3)_{1-x}(SrO)_x$ phase, which was determined at 27 °C using X-ray diffraction, revealed two distinct trends. The *a* and *c* parameters were both approximately constant for compositions below $x = 0.28$, whereas for compositions greater than $x = 0.28$, the *c* parameter increased progressively with the amount of substituted strontium, while the *a* parameter showed no significant changes.

An investigation into the temperature dependence of the lattice parameters revealed reversible discontinuities in the *a* and *c* lattice parameters at high temperatures, although the basic hexagonal crystal structure was unchanged. The *c* parameter discontinuity was greatest at low values of x, whereas the *a* parameter discontinuity was greatest in the middle of the phase and both effects decreased to the detection limit at $x < 0.40$. These discontinuities are not caused by changes in the cation subiattice, as the X-ray diffraction peak intensities were not modified on cycling through the transformation. Instead, the discontinuities are attributed to modifications in the O^{2-} occupancy of the anion sublattice, or, more precisely, in the distribution of O^{2-} vacancies among these sites. The $\beta_1 \leftrightarrow \beta_2$ phase boundary, omitted from the most recent published phase diagram for the Bi_2O_3-SrO system, was found to be asymmetric with respect to composition, in contrast to earlier reports. A revised phase diagram is presented incorporating these results.

ACKNOWLEDGMENTS

I would like to thank Dr. Hubert Wylam King for his supervision of this project. I also acknowledge the advice and support of Drs. Sankar Das Gupta and James K. Jacobs, and Mr. Oliver Gross, all of the Electrofuel Manufacturing Company, Ltd. of Toronto. My interest in the bismuth strontium oxide solid solution developed from collaborative experiments initiated by the research group of Dr. C.B. Alcock at the Center for Sensor Materials, University of Notre Dame.

My doctoral studies at the University of Western Ontario were made financially possible owing to support from the following sources : NSERC PGS3 and PGS4 Post Graduate Scholarships, an Ontario Graduate Scholarship, a U.W.O. Entrance Scholarship, part-time teaching assistantships at U.W.O., and my supervisor's research grant, and I am indebted to all of the persons and agencies involved.

On a personal note, I wish to thank my wife, Linda Twohig, without whose support and encouragement I would never have attempted doctoral studies, our daughter Catherine, whose arrival provided additional incentive to complete this work, and my parents, who always took an active role in promoting their children's educational development. Also a debt of thanks is owed to Dr. J.O. Bustamante, then at Dalhousie University, who was instrumental in developing my interest in scientific research during my undergraduate studies in Halifax.

TABLE OF CONTENTS

LIST OF SYMBOLS AND ABBREVIATIONS

T	temperature
K	Kelvins
℃	degrees Celcius
DTA	differential thermal analysis
XRD	X-ray diffraction
T_t	transformation temperature
σ	electrical conductivity
σ_i	ionic conductivity
σ_e	electronic conductivity
λ	wavelength
Å	Ångstrom (1 Å = 10^{-10} m)
hkl	Miller indices
hk•l	Miller-Bravais indices (for hexagonal cell only)
Ω	Ohms
a	lattice parameter along x axis of a unit cell
b	lattice parameter along y axis of a unit cell
c	lattice parameter along z axis of a unit cell
β	angle between z axis and x axis of a unit cell
emf	electromotive force
P_{O_2}	oxygen partial pressure
esd	estimated standard deviation
NBS	National Bureau of Standards, USA
NIST	National Institute of Standards and Technology, USA
SEM	scanning electron microscopy

LIST OF FIGURES

LIST OF TABLES

CHAPTER 1 - Introduction

The β-phase solid solutions $(Bi_2O_3)_{1-x}(MO)_x$, where M refers to the solute ions Ca, Sr, or Ba were first synthesized in the late 1930's and characterized with respect to structure. Interest in these materials was renewed in the 1970's when it was found that the electrical conductivity was ionic, rather than electronic, and of a magnitude significantly greater than for other known oxygen ion conductors, as shown in Figure 1.1.

Such solid state fast ion conductors are characterized by enhanced anionic or cationic conductivity relative to the ionic conductivity of most crystalline solids and which in some cases approaches the ionic conductivity of the liquid phase. These materials, also known as solid electrolytes, have a specific ion which is not confined to designated lattice sites, but is essentially free to move throughout the three dimensional structure. Since the atomic arrangement of the mobile ion is random, it is sometimes referred to as a "molten substructure" and often is described by a crystal structure with a significant surplus of lattice sites assigned to the mobile ion. The detailed mechanism of fast ion conduction has not yet been fully understood, since it includes the interaction of various factors which can affect intersite mobility, such as open channels in the crystal structure lattice, disorder, the number of activated mobile ions per unit volume, the relative size of mobile ions and vacancies, ion-ion interactions, the number and accessibility of vacant sites, intersite distances, etc. Any one of these factors can play a dominant role by itself, or in combination with another.

Mixed electronic-ionic conductors have many diverse applications in the development of devices such as oxygen sensors, high temperature fuel cells, and steam electrolyzers. For solid oxide fuel cells, it is desirable to develop mixed conductors in

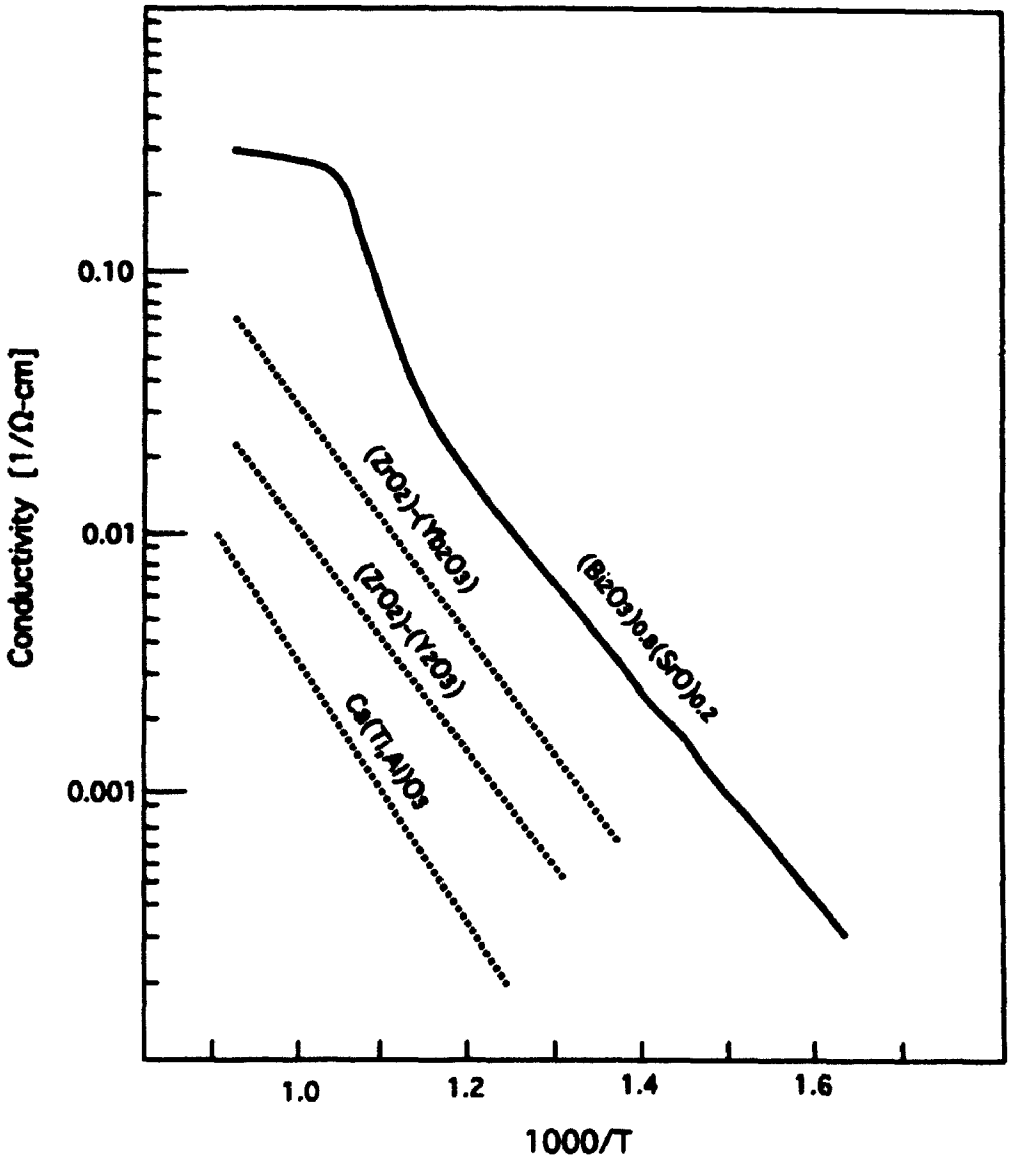

Figure 1.1 Anionic conductivities of selected materials [after Takahashi et al.]

which both electrons and ions are mobile charge carriers for the interconnection material. A considerable effort has thus been made to increase the electronic conductivity of β-alumina compounds, while maintaining their high ionic conductivity to allow oxygen ions to diffuse to the electrolyte. Other applications, such as semipermeable membranes for oxygen separation, require materials with very low electronic conductivity. In oxygen sensors, for example, any electronic conduction will act as a short circuit and cause the sensor characteristics to differ from the ideal model, but, on the other hand, the electronic conduction does have the advantage of increasing the response time of the sensor.

Other considerations in the development of effective solid state electrolyte devices are the thermal stability of the material, to permit long service life, and the thermal expansivity, which must be accommodated in the design of the solid state device. The equilibrium phase diagram, as a statement of the stability range of the potential electrolyte phase, is a useful tool for the engineer / scientist in the selection of appropriate materials and operating temperatures for such devices. The number of published phase diagrams has grown steadily throughout this century, yet there are still some systems for which no diagram exists and many others for which the published diagram is inaccurate, or incomplete. In the following chapters, this will be shown to be the case for the solid solution β-$(Bi_2O_3)_{1-x}(SrO)_x$.

In concluding this introduction, it is noted that a number of materials undergo solid-solid phase transformations accompanied by a sharp jump in ionic conductivity on entering the high temperature phase. Such a conductivity jump is apparent from Figure 1.1 for the β-$(Bi_2O_3)_{1-x}(SrO)_x$ solid solution, which strongly suggests the existence of a structural transformation. It is hoped that the following detailed characterization of the transformation with respect to structure will be of value in further development of these materials.

CHAPTER 2 - Background and Theory

2.1 Introduction

Pure bismuth oxide, Bi_2O_3, is known to exist in four crystal structures [1]. The monoclinic α-phase is stable from room temperature up to 730 °C, where it transforms to the cubic δ-phase, which is stable to the melting temperature of 825 °C. Cooling the α-phase below 650 °C can produce a transformation into a tetragonal β-phase or a cubic γ-phase. The factors influencing the transformation into either of these metastable phases are not well understood, but impurities are considered to play a significant role. For this reason, the β and γ-phases are not included in the equilibrium phase diagrams of bismuth oxide systems. The α-phase is essentially an electronic p-type semiconductor, but the β, γ, and δ phases are predominantly ionic conductors, with oxygen ions as the major charge carriers.

Sillén and Aurivillius [2-3] attempted to stabilize the tetragonal form of β-Bi_2O_3 through partial substitutions of Bi^{3+} by cations with similar ionic radii, such as Pb^{2+} and Sr^{2+}. These authors found that substitutions of Bi^{3+} by Pb^{2+} form a stable tetragonal solid solution over the range 29 - 53 at% Pb, whereas substitutions of Bi^{3+} by Sr^{2+} form a stable rhombohedral solid solution over the range 11 - 28 at% Sr. The latter structure was also observed by Aurivillius [4] for substitutions of Bi^{3+} by the other alkali earths, Ba^{2+} and Ca^{2+}. For the remainder of the thesis, the designation "β-phase" is used to indicate the rhombohedral intermediate solid solution, while the alternate tetragonal structure of Bi_2O_3 will be referred to as β-Bi_2O_3.

The composition of the β-phase may be conveniently described in terms of the molar ratio, x, of the constituent oxides, *i.e.*, $(Bi_2O_3)_{1-x}(MO)_x$, where M refers to the solute ion. An alternate description frequently found in the literature is based on the cation ratio, y, *i.e.*, $Bi_{1-y}M_yO_{1.5-y/2}$, which is related to the molar ratio by :

$$y = \frac{x}{2-x} \qquad \text{or} \qquad x = \frac{2y}{1+y} \qquad \text{[eqn. 1]}$$

2.2 Crystal Structure Determinations

Laüe X-ray patterns of small single crystals indicated [3] that the point group symmetry of the β-phase is 3m. Additional X-ray diffraction measurements using Rotation, Weissenberg, and Guinier methods enabled the space groups to be limited to R32, R3m, or R$\bar{3}$m. The nonprimitive hexagonal cell provides a more useful description of the structure since the hexagonal c-axis is normal to the atom layers. The rhombohedral indices, the equivalent hexagonal indices, and the observed intensities of the observed diffracting planes of the β-phase structure are shown in Table I.

However due to the complex form of the rhombohedral structure, with nine atom positions per unit cell, it is more convenient to express the structure in terms of the equivalent hexagonal reference axes, as shown in Figure 2.1. X-ray densities calculated on the basis of the lattice parameters, show that a crystal structure modelled on nine cations per unit cell fits very well to the observed density measurements for various strontium concentrations across the β-phase. The hexagonal cell is particularly helpful in the present context as it clearly shows that the structure is composed of interleaved anion and cation layers oriented normal to the c-axis of the unit cell.

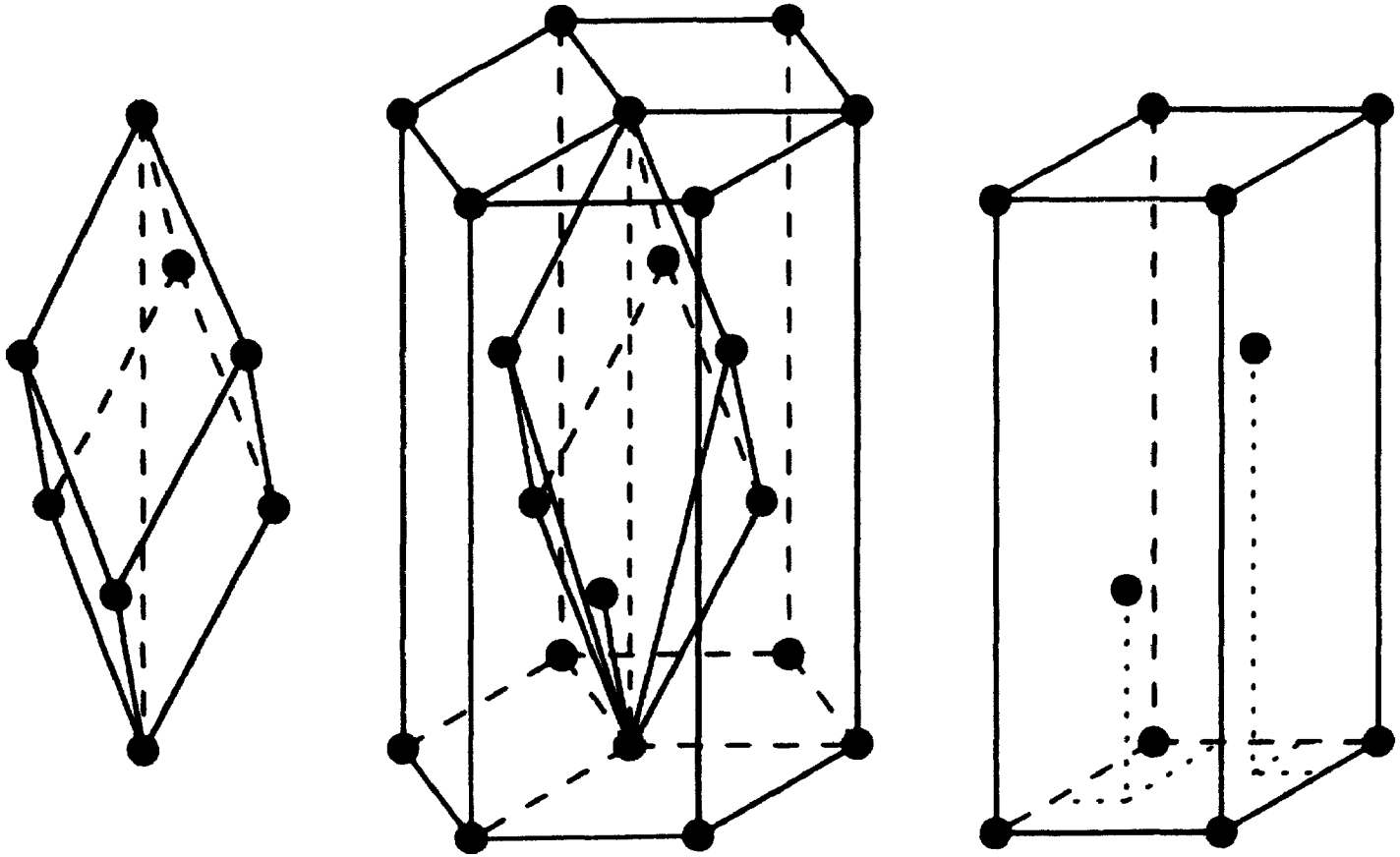

Figure 2.1 Relationship between rhombohedral and hexagonal unit cells

Table I

X-Ray Diffraction Results of Sillén and Aurivillius for β-$(Bi_2O_3)_{0.587}(SrO)_{0.413}$

hkl_{rh}	$hk\cdot l_{hex}$	I_{obs}	hkl_{rh}	$hk\cdot l_{hex}$	I_{obs}
100	10·1	m	554	10·14	m+
110	10·2	m	200	20·$\bar{2}$	vvw
333	00·9	st	432	11·9	m
211	10·$\bar{4}$	m+	220	20·4	vvw
221	10·5	m	311	20·$\bar{5}$	vvw
322	10·$\bar{7}$	w+	666 / 655	00·18 / 10·$\bar{16}$	st
332	10·8	w+	665	10·17	m
444	00·12	vw	533	20·$\bar{11}$	vvw
433	10·$\bar{10}$	w	654	11·15	vvw
443	10·11	m	777	00·21	vvw
1$\bar{1}$0	11·0	m	553	20·13	vw
555	00·15	m+	766	10·20	m
544	10·$\bar{13}$	st	765	11·18	m
321	11·6	vvw	877	10·$\bar{22}$	m+

As indicated by the crystal structure data in Table II, the cations are located on three "a" sites [at equivalent lattice points +(0,0,0)] and six "c" sites [at equivalent lattice points +(0,0,±z)] with respect to the equivalent lattice positions of the hexagonal cell. The calculated and observed intensities of diffraction lines with the same *hk* hexagonal indices, which permit direct comparison between intensities without regard to errors due to preferred orientation, can be correlated with Sr ions and Bi ions being randomly distributed on the three "a" sites, while the six "c" sites contain only Bi ions. The position of the bismuth "c" site was refined to a displacement a fractional distance equal to ±0.226 along the c-axis for a sample of composition x = 0.413. This site is slightly displaced from the "ideal" geometric position of z = 2/9, or z_{Bi} = 0.222, in further support of the

hypothesis that the composition of the (Bi,Sr) "a" sites are different from the (Bi) "c" sites. The resultant cation sublattice of the β-phase structure is illustrated in Figure 2.2, from which it is evident that the strontium substituted layers (the "a" sites) are sandwiched between two bismuth layers (the "c" sites).

Table II

Structural Data for β-$(Bi_2O_3)_{0.587}(SrO)_{0.413}$ [after Sillén and Aurivillius]

hR27	S.G.: R$\bar{3}$m		Equivalent lattice positions : $(000, \frac{1}{3}\frac{2}{3}\frac{1}{3}, \frac{2}{3}\frac{1}{3}\frac{2}{3})+$	
3	(Sr, Bi_1)	in 3(a)	000	
6	Bi_2	in 6(c)	00z, 00$\bar{z}$,	$z_{Bi} = 0.226$
6	O_1	in 6(c)	00z, 00$\bar{z}$,	$z_1 = 0.135$
6	O_2	in 6(c)	00z, 00$\bar{z}$,	$z_2 = 0.308$
6	O_3	in 6(c)	00z, 00$\bar{z}$,	$z_3 = 0.413$

On the basis of their X-Ray data, Sillén and Aurivillius further proposed [3] that the oxygen ions are distributed among eighteen "c" sites displaced from the equivalent lattice positions along the c-axis of the hexagonal cell by: $z_1 = \pm 0.135$, $z_2 = \pm 0.308$, and $z_3 = \pm 0.413$, as indicated in Table II. If all of the available cation sites in the β-phase are fully occupied, as proposed by Sillén and Aurivillius, the equivalent occupation of the oxygen ion sites would require a composition $(Bi,Sr)O_2$. Therefore, even with no substitution of Sr^{2+} for Bi^{3+}, at least 4.5 of the oxygen sites must be vacant at a composition Bi_2O_3 (*i.e.*, $BiO_{1.5}$). In order to balance the ionic charges, the substitution of Sr^{2+} for Bi^{3+} further reduces the number of oxygen ions in the β-phase such that at x = 0.413 only 12.33 of the possible eighteen oxygen sites are occupied, *i.e.*, approximately one third are empty. However since the atomic scattering factors of the cations Bi (Z =

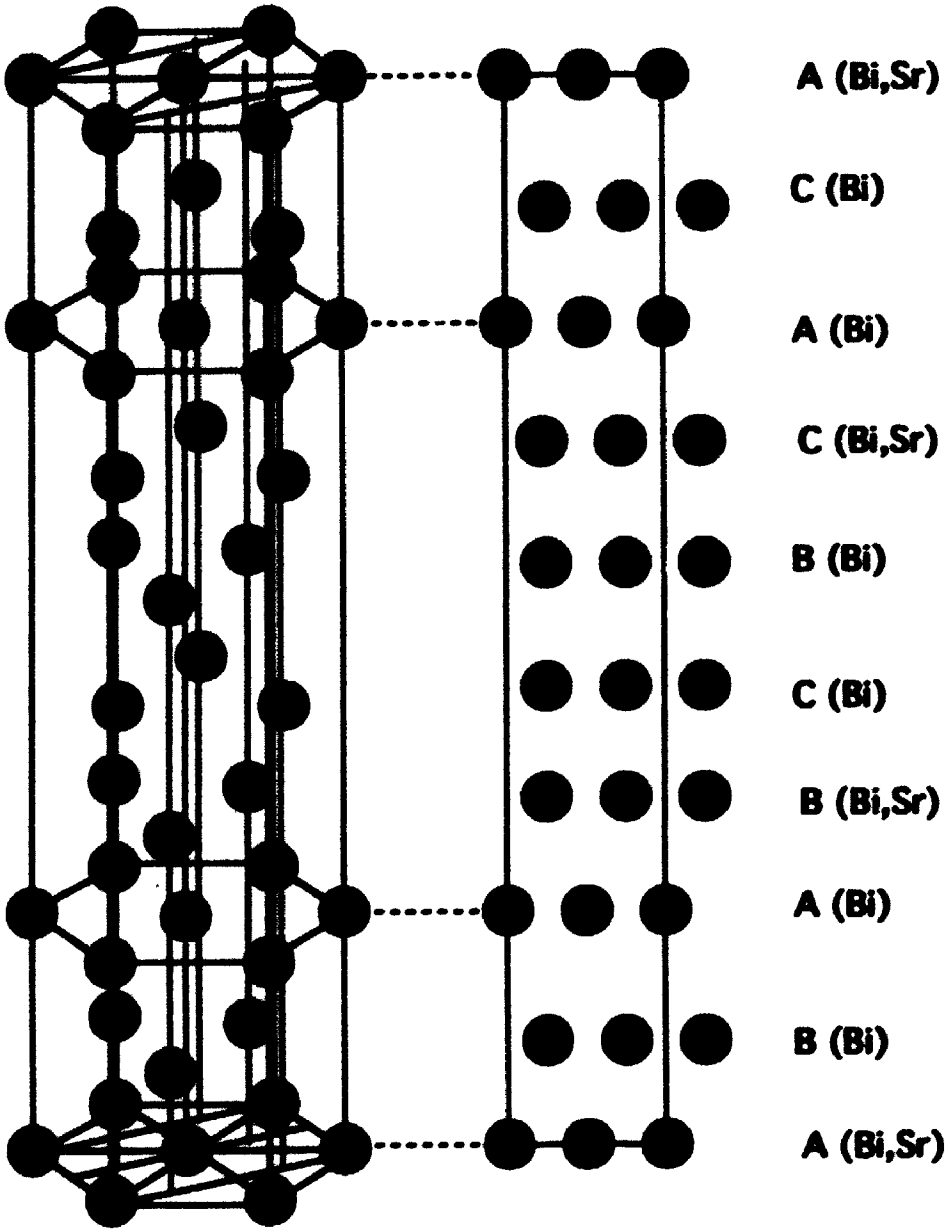

Figure 2.2 β-phase hexagonal cation sublattice [after Sillén and Aurivillius]

83) and Sr (Z = 38) are very much greater than for O (Z = 8), the oxygen ions have only a small influence on diffracted peak intensities, so that the distribution of the oxygen ions among the available "c" sites could not be established. The complete structure of the β-phase showing the layers of the occupied cation sites and double layers of available oxygen ion sites sandwiched between them is shown in Figure 2.3.

The structure of $Bi_{0.765}Sr_{0.235}O_{1.383}$ (x = 0.38) was later determined by Conflant *et al.* [5] from single crystal X ray diffraction data by Fourier synthesis and least squares refinement. As indicated in Table III, the Sr ions are constrained to substitute for Bi only at the three "a" sites [at equivalent lattice points +(0,0,0)] in agreement with the earlier prediction of Sillén and Aurivillius. The remaining Bi ions were refined to six "c" sites [at equivalent lattice points $+(0,0,\pm z_{Bi})$] with $z_{Bi} = 0.22397$, similar to $z_{Bi} = 0.226$ which was determined by Sillén and Aurivillius for the composition x = 0.413.

Table III

Refined Structural Parameters of β-$(Bi_2O_3)_{0.62}(SrO)_{0.38}$ [after Conflant *et al.*]

hR27 S.G.: R$\bar{3}$m Equivalent lattice positions : $(000, \frac{1}{3}\frac{2}{3}\frac{1}{3}, \frac{2}{3}\frac{1}{3}\frac{2}{3})+$

3	(Sr, Bi_1)	in 3(a)	000	
6	Bi_2	in 6(c)	00z, 00$\bar{z}$,	$z_{Bi} = 0.22397$
6	O_1	in 6(c)	00z, 00$\bar{z}$,	$z_1 = 0.29459$
< 6	O_2	in 6(c)	00z, 00$\bar{z}$,	$z_2 = 0.09907$
<< 6	O_3	?	?	z_3 = ?

The oxygen ion positions were refined at six "c" sites [at equivalent lattice points $+(0,0,\pm z_{O_1})$]. The first set of oxygen positions are located at $z_{O_1} = 0.29459$, which is

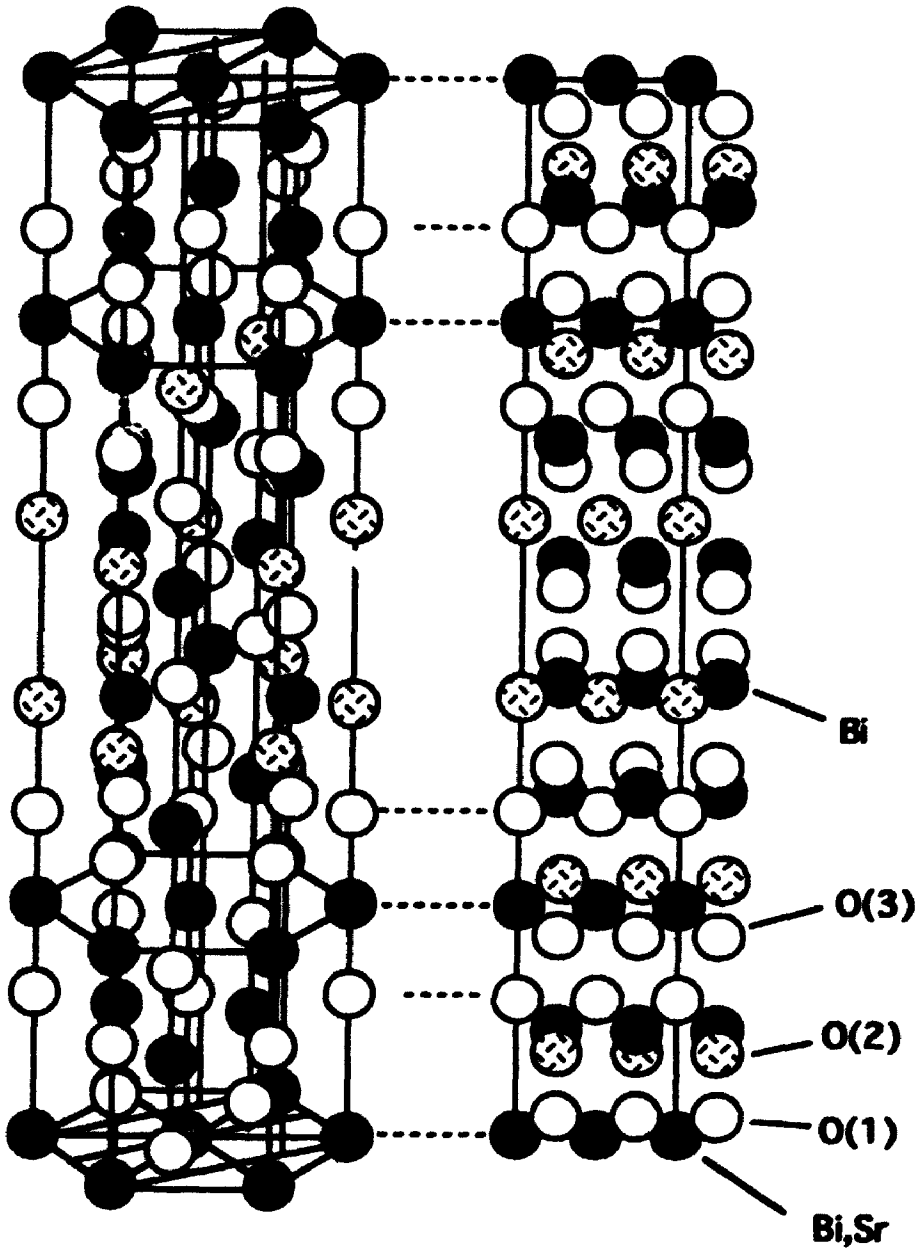

Figure 2.3 Full β-phase hexagonal structure [after Sillén and Aurivillius]

close to the site $z_2 = 0.308$ suggested by Sillén and Aurivillius [3]. A second set of oxygen positions was located at $z_{O2} = 0.09907$, but this refinement required an unusually large thermal coefficient, indicating low occupancy and/or weak bonding. Since these anions coordinate with both Bi^{3+} and Sr^{2+} cations, the sites cannot be fully occupied, and furthermore the occupancy must decrease as a function of solute concentration. This site may be considered to be equivalent to the O_1 site at $z_1 = 0.135$ proposed by Sillén and Aurivillius. The remaining oxygen ion sites, O_3, could not be determined from the X-ray diffraction results, but, from the geometry of the structure, Conflant *et al.* suggested [5] that these anions are loosely bound in the space between the consecutive bismuth layers.

The revised structure proposed by these authors [5] is illustrated in Figure 2.4. The six pure Bi^{3+} "c" sites have significantly shorter Bi_1 - O_1 bond lengths (2.01 Å) compared to the lengths (2.35 Å) predicted by Sillén and Aurivillius. This contraction of the bond length was attributed to an increase in the covalency of the bond. In the three substituted "a" sites, each cation is coordinated to six near-neighbour fully occupied oxygen O_1 sites, and two more distant partially occupied O_2 sites, as illustrated in Figure 2.5, with the nearest neighbour oxygen anions forming a distorted octahedron surrounding the (Bi,Sr) site.

An electron diffraction examination of β-$(Bi_2O_3)_{1-x}(BaO)_x$ was reported by R.J.D. Tilley [6]. Single phases were produced from quenched melts, as per Sillén and Aurivillius [3], but multiphase mixtures were observed after annealing for 1000 hours at 725 K in air. Complementary X-ray diffraction patterns of the quenched samples had peaks which were "...broad and poorly defined...", but in annealed samples "...the lines were slightly more diffuse..." [6]. In addition to the rhombohedral β-phase, an annealed sample with composition $x = 0.20$ sample also contained well resolved diffraction lines of

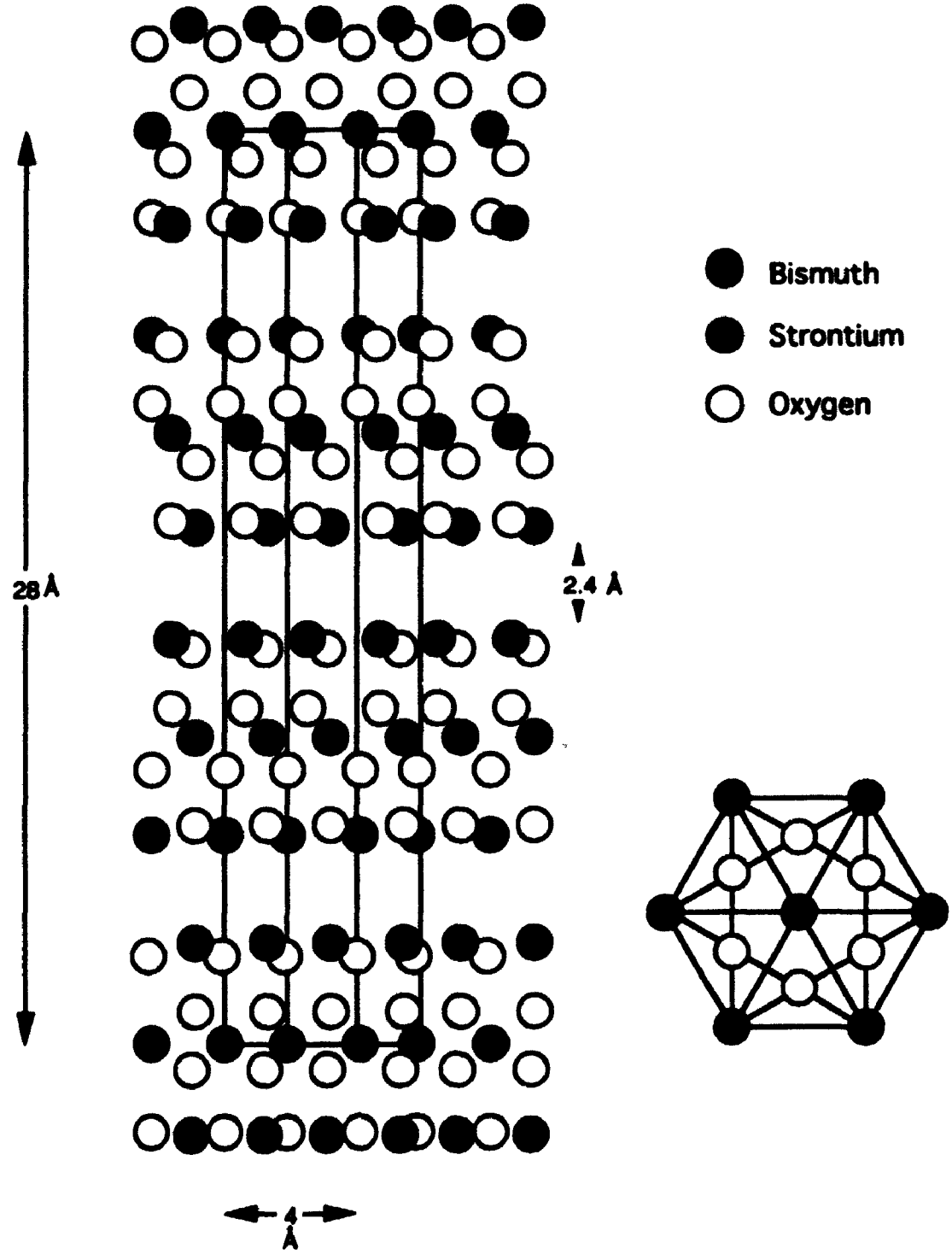

Figure 2.4 Revised β-phase hexagonal structure [after Conflant et al.]

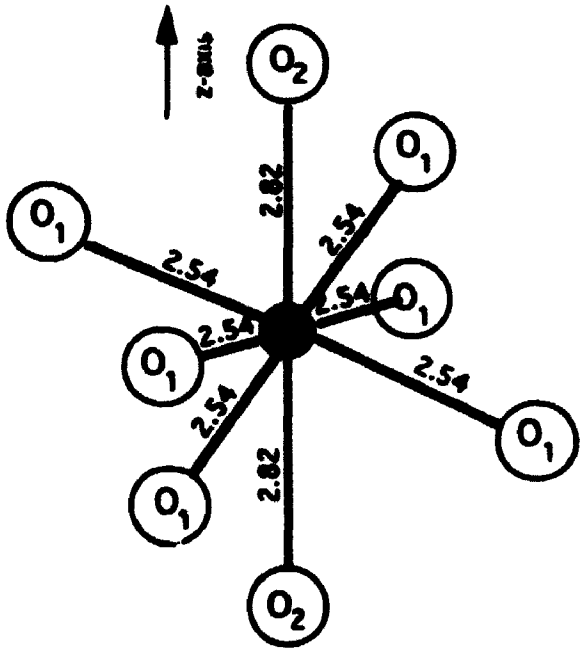

Figure 2.5a (Bi,Sr) site coordination [after Conflant et al.]

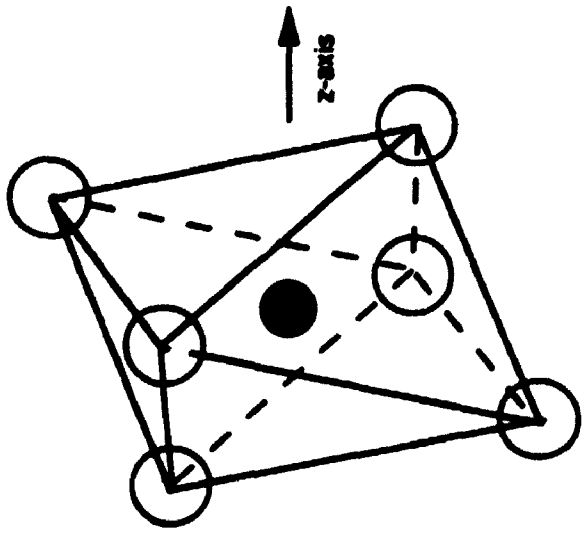

Figure 2.5b Six-fold coordination octahedron of nearest neighbour oxygen anions surrounding the (Bi,Sr) cation site

α-Bi_2O_3, whereas an equivalent sample with x = 0.333 contained sharp lines of an unknown tetragonal phase.

Forbidden reflections such as 01•0, 20•0, 21•0 were always observed in (00•1) lattice plane diffraction patterns, and were attributed to the well-known "double diffraction" effect in the crystal [6]. In addition, superlattice reflections, which were observed in the majority of the crystals, were interpreted to indicate the presence of microdomains of Bi/Ba ordering, as oxygen vacancy ordering was deemed to make too small a contribution to the electron diffraction. On the presumption that the barium only substitutes for bismuth on three "a" sites, a simple model was proposed for the x = 0.20 composition in which every third "a" site was occupied by a Ba^{2+} cation. It was suggested that a further TEM study would be undertaken, but a search of the literature has not located any subsequent publication on the β-phase at this laboratory.

A neutron diffraction study was conducted on β-$(Bi_2O_3)_{1-x}(CaO)_x$ by Blower and Greaves [7]. As discussed previously, X-rays are diffracted due to interaction with electrons, and the cation lattice sites can thus be determined with some confidence, but the anion sites are less well defined because of the relatively low atomic number of oxygen. In contrast to X-ray diffraction, the scattering lengths for neutron diffraction are $l_{Bi} = 8.53$, $l_{Ca} = 4.7$, and $l_O = 5.81$, and the neutron diffraction pattern is consequently much more sensitive to the oxygen ion positions. Their neutron diffraction pattern showed three additional reflections, that could not be indexed in accordance with the previously accepted R3m rhombohedral space group symmetry. By assuming that these additional lines are the result of oxygen ordering, a new larger unit cell (superlattice) was proposed, based on the monoclinic space group C2/m. This monoclinic structure is related to the rhombohedral lattice, but its lower symmetry permits the location of additional oxygen lattice sites so that a significantly better Rietveld refinement of the

neutron diffraction data could be achieved. The detailed refined structure data derived from the neutron diffraction analysis are given in Table IV. As discussed previously, the total number of lattice sites requires a composition $(Bi,Ca)O_2$, so that a number of oxygen ion sites will be vacant in the β-phase. These vacancies are identified by fractional numbers of oxygen ions located in sites O_4 to O_9.

Table IV

Refined Parameters for β-$(Bi_2O_3)_{0.7}(CaO)_{0.3}$ [after Blower and Greaves]

mC56 S.G.: C2/m Equivalent lattice positions : $(000, \frac{1}{2}\frac{1}{2}0)+$

2	$(Ca, Bi)_1$	in 2(a)	000	
2	$(Ca, Bi)_2$	in 2(b)	$0\frac{1}{2}0$	
4	$(Ca, Bi)_3$	in 4(e)	$0\frac{1}{4}0$	
4	Bi_1	in 4(i)	x0z, $\bar{x}0\bar{z}$,	x = .379, z = .319
4	Bi_2	in 4(i)	x0z, $\bar{x}0\bar{z}$,	x = .880, z = .323
8	Bi_3	in 8(j)	xyz, $x\bar{y}z$, $\bar{x}yz$, $\bar{x}\bar{y}\bar{z}$,	x = .137, y = .248, z = .327
4	O_1	in 4(i)	x0z, $\bar{x}0\bar{z}$,	x = .323, z = .108
4	O_2	in 4(i)	x0z, $\bar{x}0\bar{z}$,	x = .839, z = .121
8	O_3	in 8(j)	xyz, $x\bar{y}z$, $\bar{x}yz$, $\bar{x}\bar{y}\bar{z}$,	x = .101, y = .243, z = .089
2.24	O_4	in 4(i)	x0z, $\bar{x}0\bar{z}$,	x = .043, z = .286
2.24	O_5	in 4(i)	$x\frac{1}{2}z$, $\bar{x}\frac{1}{2}\bar{z}$,	x = .075, z = .254
4.48	O_6	in 8(j)	xyz, $x\bar{y}z$, $\bar{x}yz$, $\bar{x}\bar{y}\bar{z}$,	x = .308, y = .266, z = .280
2.24	O_7	in 4(i)	x0z, $\bar{x}0\bar{z}$,	x = .249, z = .382
2.24	O_8	in 4(i)	$x\frac{1}{2}z$, $\bar{x}\frac{1}{2}\bar{z}$,	x = .129, z = .375
4.48	O_9	in 8(j)	xyz, $x\bar{y}z$, $\bar{x}yz$, $\bar{x}\bar{y}\bar{z}$,	x = .474, y = .219, z = .315

The results of this neutron diffraction investigation strongly suggest that the rhombohedral structure originally proposed for β-$(Bi_2O_3)_{1-x}(CaO)_x$ should be regarded as a first approximation, and this conclusion can be extended to the related β-phase solid solutions containing strontium or barium. However, the relatively limited access to neutron diffraction facilities, has meant that no further neutron diffraction studies have been reported in the literature to confirm the monoclinic structure.

2.3 Composition Dependence of Lattice Parameters

The lattice parameters of β-$(Bi_2O_3)_{1-x}(BaO)_x$, β-$(Bi_2O_3)_{1-x}(SrO)_x$, and β-$(Bi_2O_3)_{1-x}(CaO)_x$ determined by various authors [3-13] over a period of fifty years are remarkably consistent as shown by the summary of results in Figure 2.6. The *a* and *c* lattice parameters for β-$(Bi_2O_3)_{1-x}(BaO)_x$ are both increased with concentration, x, which is consistent with the relatively large size of the Ba^{2+} ion compared to Bi^{3+}, as indicated in Table V by the ionic sizes for the relevant six fold coordination environment of the three "a" sites at which the substitution occurs [14]. In the β-$(Bi_2O_3)_{1-x}(SrO)_x$ phase the change in c parameter with x, is greater than one would expect solely on the basis of the relative size of the Sr^{2+} ion, but no measurable change is observed for the *a* parameter in this solid solution. It is also noted that this system has a greater scatter in the experimental data for the *c* parameter. In the β-$(Bi_2O_3)_{1-x}(CaO)_x$ system, the *c* parameter increases with x, however, the *a* parameter shows a decrease with x. Since the size of the Ca^{2+} ion is slightly smaller than Bi^{3+} these results indicate that the increase in the *c* parameter of the β-phase is not directly linked to the physical size of the solute ion.

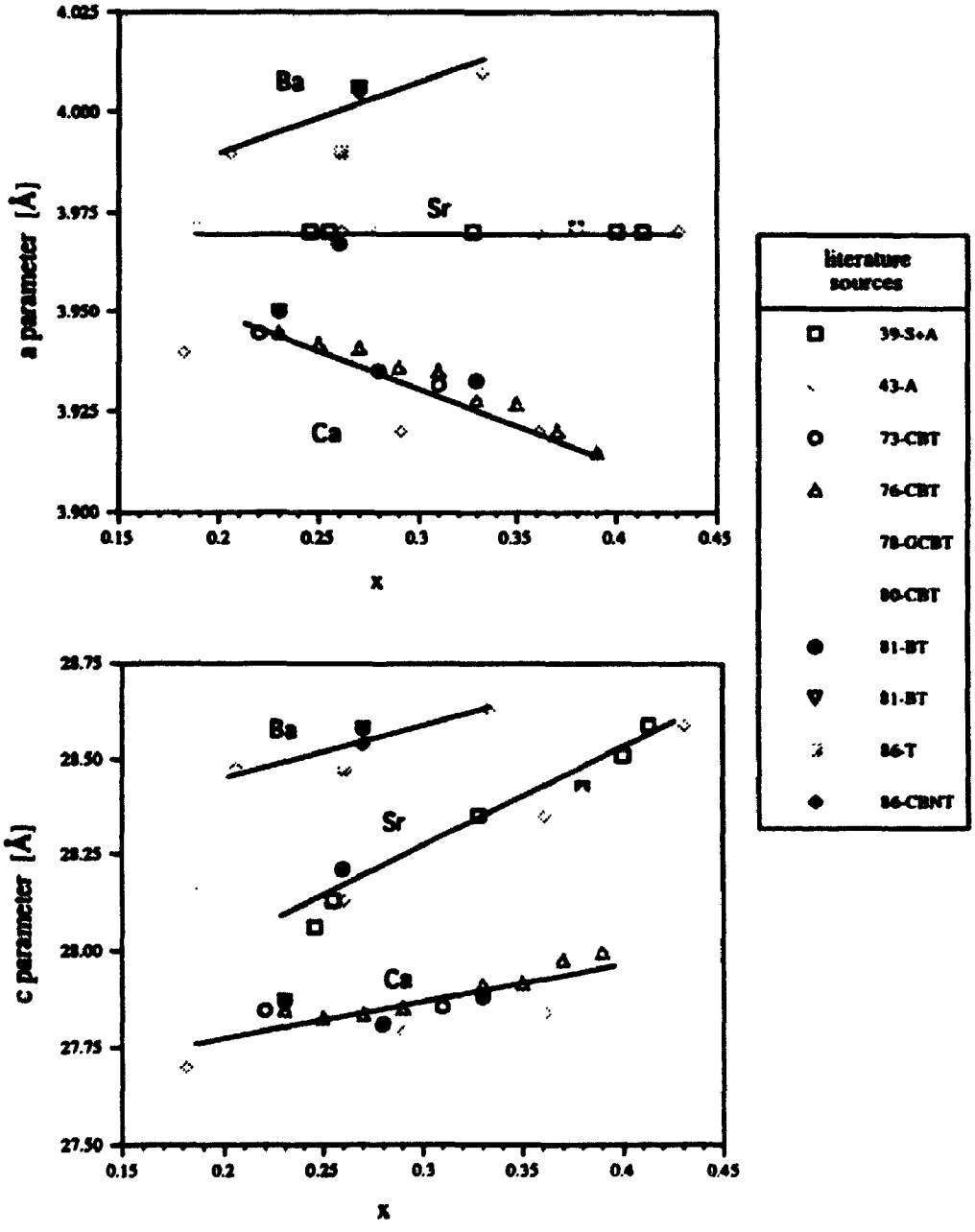

Figure 2.6 Compositional dependence of β-$(Bi_2O_3)_{1-x}(MO)_x$ lattice parameters

Table V

Ionic Radii [after Shannon and Prewitt]

Ion	Electronic Configuration	Ionic Radius [Å] CN = 6
O^{-2}	$3p^6$	1.40
Ba^{+2}	$5p^6$	1.36
Pb^{+2}	$6s^2$	1.18
Sr^{+2}	$4p^6$	1.16
Bi^{+3}	$6s^2$	1.02
Ca^{+2}	$3p^6$	1.00
Y^{+3}	$4p^6$	0.892

2.4 Temperature Dependence of Electrical Conductivity

While studying a number of oxide systems with intermediate or terminal solid solutions with the fluorite structure containing oxygen anion vacancies, Neuimin *et al.* [15] noted the β-phase in the (Bi_2O_3)-(SrO) system and examined its electrical conductivity. The ionic fraction of the conductivity was determined in an electrochemical cell by comparing the measured emf, E, with the thermodynamic value, E_o, given by the Nernst equation :

$$E_o = \frac{RT}{4F} \ln \frac{(P_{O_2})_{cathode}}{(P_{O_2})_{anode}} \qquad \text{[eqn. 2]}$$

where P_{O_2} represents the oxygen partial pressure, R is the molar gas constant constant, T is the temperature, and F is Faraday's constant. In a mixed-mode conductor the emf is lower than that for a purely ionic conductor, since the cell is discharged by the electronic conduction, σ_e. The ion transference number, t_i, which is the ratio of the ionic

conductivity, σ_i, to the total conductivity is determined from the ratio of the measured emf to the thermodynamic emf, *i.e.*,:

$$t_i = \frac{\sigma_i}{\sigma_i + \sigma_e} = \frac{E}{E_0} \qquad \text{[eqn. 3]}$$

It follows from equation 3 that a strictly ionic conductor has an ion transference ratio t_i = 1.00, while a strictly electronic conductor has t_i = 0.00. The electrical conductivity of the β-phase samples was relatively high compared to other oxygen ion conductors, as shown in Fig. 2.7, with a greater than 50% ionic component, at temperatures above 500 °C.

Takahashi *et al.* [16] followed up these experiments with a study which suggested that the conductivity of β-$(Bi_2O_3)_{1-x}(SrO)_x$ was 4-5 times greater than reported by Neuiman *et al.*. The increased conductivity was attributed to a higher sintering temperatures of 800 - 1000 °C used to prepare their ceramics, as compared to 720 - 750 °C used by Neuimin *et al.*. The conductivity of the β-phase was also demonstrated to be almost completely ionic, such that the ion transference ratio, t_i, was found to be greater than 0.9 over the whole range from 500 - 800 °C. In addition, the ratio E/E_0 was strongly dependent on the oxygen partial pressure, and this observation was attributed to an increase in the electronic conduction due to reduction of the samples in low P_{O_2} environments. The need for high P_{O_2} to stabilize the β-phase was illustrated by the rapid reduction of samples under hydrogen atmosphere at temperatures as low as 600 °C.

A significant reversible increase in conductivity was observed in the range 620 - 670 °C, and, in addition, a small endothermic DTA peak was reported at the same temperature. No structural change was identified by comparing high temperature X-ray diffraction patterns at 400 °C and 750 °C, *i.e.*, below and above the supposed transition

temperature, however, in the closely related $(Bi_2O_3)_{1-x}(BaO)_x$ system, where a similar DTA peak was found around 580 °C [17], an irreversible increase in the intensity of the 00•l diffraction peak was observed after cycling to high temperatures. These results were interpreted to indicate a reversible order:disorder transition in the β-phase.

The stability of the ionization states of Bi^{3+} and Ba^{2+} was confirmed by a lack of mass change during thermogravimetric analysis [17], since a valence change in either case would cause a change in mass due to an increase or decrease in oxygen content to maintain the required charge balance. This means that the reversible increase in conductivity observed at 620 - 670 °C cannot be ascribed to a change in the valence state of either of the cations in the material and is therefore more likely to be caused by some form of structural transformation.

Boivin *et al.* published high temperature conductivity measurements [13] for nine samples of β-$(Bi_2O_3)_{1-x}(SrO)_x$ over the range $0.20 \leq x \leq 0.42$, as shown in Figure 2.7. There is probably a mislabeling of the conductivity data in the original paper, since two different curves are attributed to the x=0.22 composition. A careful examination of a later paper by the same authors clearly indicates that one of the curves should be relabelled as x = 0.26, which is the label given in Figure 2.8. All of these samples show an increase in conductivity in the temperature range $620°C \leq T \leq 720°C$, in confirmation of the results of Takahashi *et al.* [16] referred to above. The conductivities shown in Figure 2.8 conform to an Arrhenius-type law, from which the activation energy barriers, E_a, may be estimated from the slopes of the lines of each composition, above and below the conductivity change. These values are plotted in Figure 2.8, from which it may be seen, as noted by Boivin *et al.* [13], that the activation energy increases slightly with strontium concentration. In addition, it is clear that the activation energy barrier of the

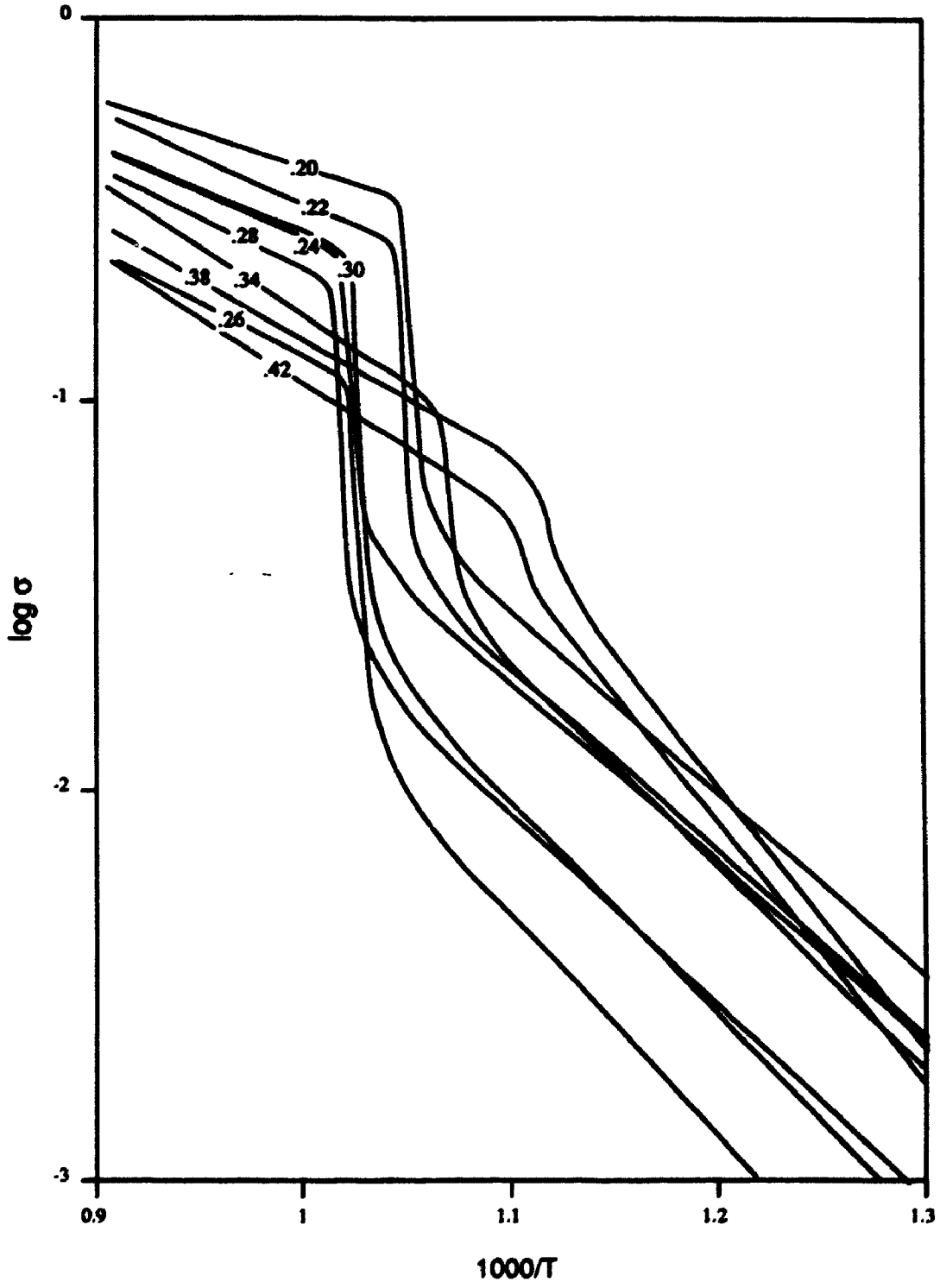

Figure 2.7 High temperature conductivity measurements [after Boivin et al.]

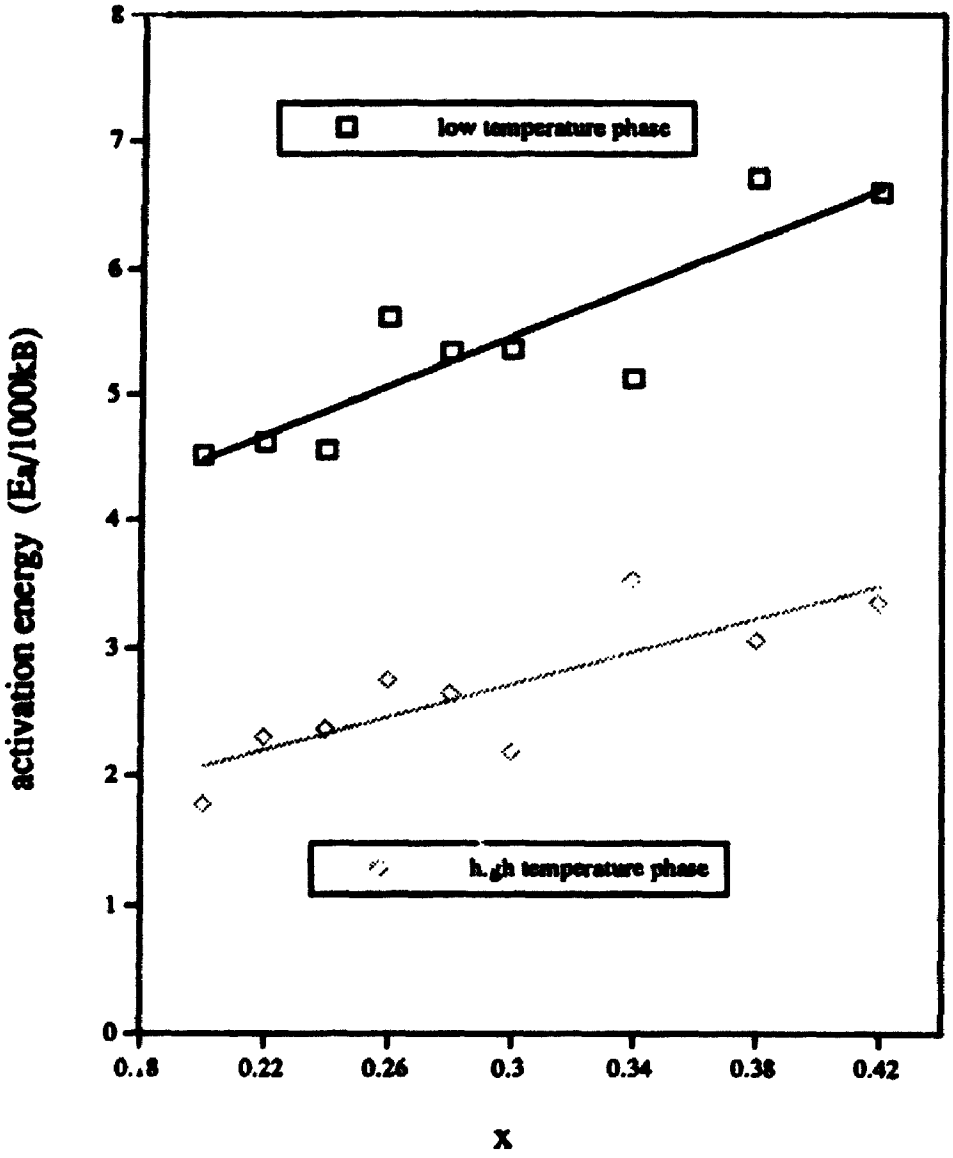

Figure 2.8 Activation energies derived from the data of Figure 2.7

low temperature phase is greater than for the high temperature phase, a feature not previously noted in the literature.

Boivin *et al.* [12] also obtained single crystal conductivity data for the composition x = 0.26. The conductivity parallel to the c-axis was found to be two orders of magnitude greater than the conductivity perpendicular to the c-axis, and about an order of magnitude greater than the value obtained for an equivalent polycrystalline ceramic. This finding is consistent with the extreme anisotropy of the structure of the β-phase.

2.5 Temperature Dependence of Lattice Parameters

As part of a general study of the systems β-$(Bi_2O_3)_{1-x}(CaO)_x$, β-$(Bi_2O_3)_{1-x}(SrO)_x$, and β-$(Bi_2O_3)_{1-x}(BaO)_x$, Conflant *et al.* [9] and Guillermo *et al.* [10] conducted high temperature X-ray diffraction experiments. These results confirmed the presence of a high temperature phase, β_1, which is also rhombohedral, but with a significantly increased *c* parameter in all three of these systems. As shown by the plot of their lattice parameter data in Figure 2.9, a sharp discontinuity was observed in the *c* parameter at a temperature which correlates with the increase in electrical conductivity (see Figure 2.7). Similar, but very small, discontinuities were also reported at the same temperature for the *a* parameters of these systems. This structural modification was reversible, and the β_1 phase could not be retained on quenching to room temperature. The authors attributed this effect to a rearrangement of the oxygen vacancy network, which would consequently permit greater anion mobility, *i.e.*, increased oxygen ion conductivity.

Takahashi *et al.* [16,17] included high temperature X-ray diffraction experiments in their earlier investigations into the abrupt increase in conductivity with temperature in β-$(Bi_2O_3)_{1-x}(SrO)_x$, and β-$(Bi_2O_3)_{1-x}(BaO)_x$. Diffraction data was obtained at

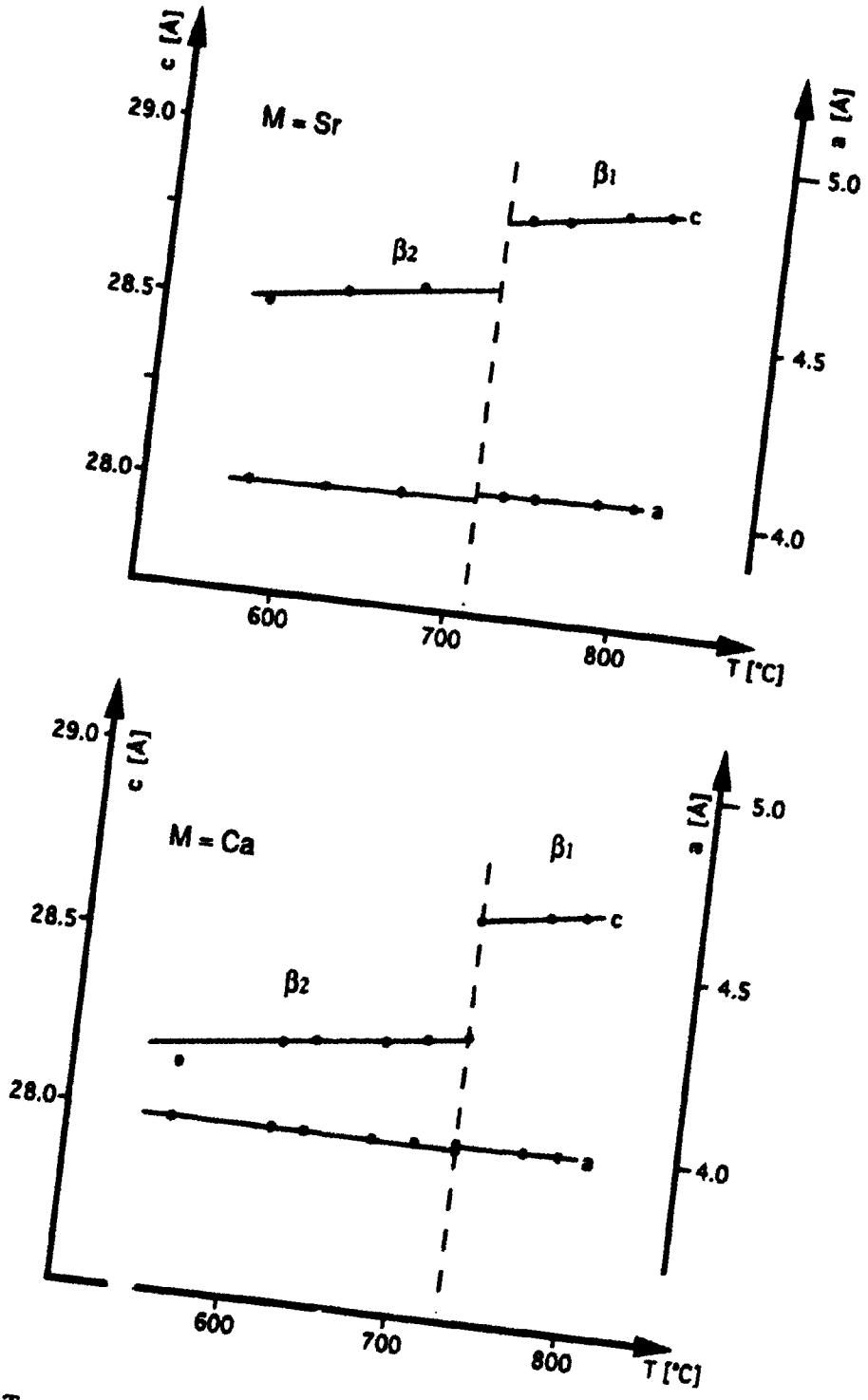

Figure 2.9 Temperature dependence of lattice parameters in β-$(Bi_2O_3)_{1-x}(MO)_x$ for M = Ca and Sr [after Conflant *et al.* and Guillermo *et al.*]

temperatures above and below the supposed transformation temperature, as indicated by conductivity and DTA measurements, but no structural change was observed. Instead, an increase in the intensities of the 00•3, 00•6, and 00•9 diffraction peaks after thermal cycling of their samples was interpreted [17] as indicating an order:disorder transformation.

2.6 Phase Diagrams

On the basis of X-ray structural studies, Aurivillius [4] gave the range of composition of β-$(Bi_2O_3)_{1-x}(SrO)_x$ as $0.18 \leq x \leq 0.42$. The lower composition boundary of this phase was confirmed by Levin and Roth [18] on the basis of high temperature X-ray diffraction studies in the two phase region at $x = 0.095$, as shown in Figure 2.10, which represents the first attempt at a phase diagram for the Bi_2O_3-SrO system.

Using a combination of differential thermal analysis and high temperature X-ray diffraction, Guillermo *et al.* [10] obtained the phase diagram shown in Figure 2.11, in which the limits of three solid solutions, α (based on the high temperature δ-phase of Bi_2O_3), β, and γ were established, and three intermediate compounds were identified at the compositions Bi_2SrO_4, $Bi_2Sr_2O_5$, and $Bi_2Sr_3O_6$. The limits defined for the β-phase, $0.18 \leq x \leq 0.43$, agree almost exactly with those proposed 35 years earlier by Aurivillius [4]. On the basis of discontinuities in conductivity, lattice parameters, and DTA, a reversible structural transformation was proposed from the known low temperature rhombohedral solid solution, β_2, to a modified rhombohedral solid solution, β_1.

A revised phase diagram was later presented by Huang *et al.* [19] and Roth *et al.* [20], as shown in Figure 2.12. An additional phase, $Sr_6Bi_2O_9$, was added in the SrO-rich region of the diagram. The stability of the compounds $Sr_3Bi_2O_6$ and $Sr_2Bi_2O_5$ were also

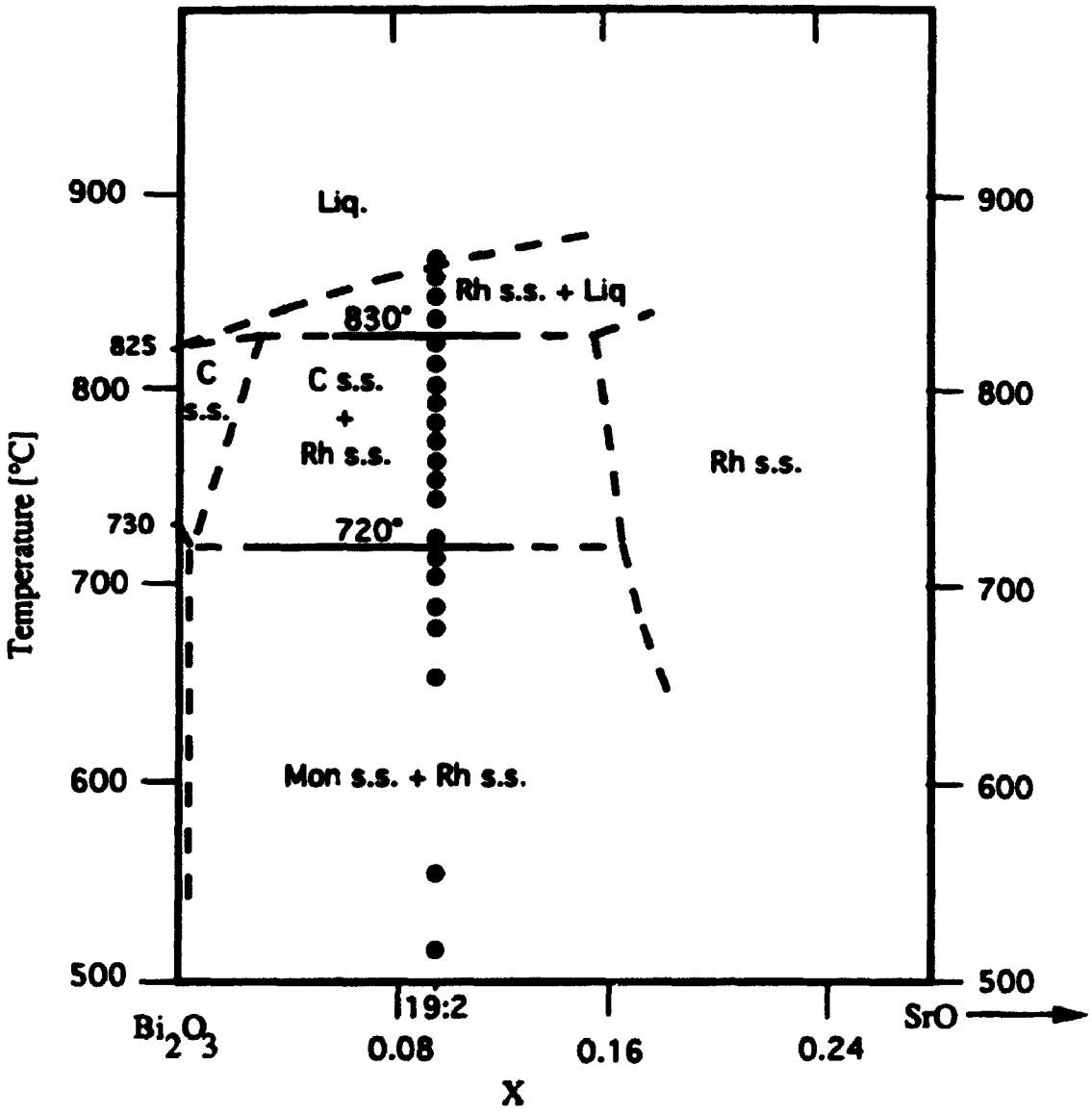

Figure 2.10 Bi_2O_3-SrO phase diagram [proposed by Levin and Roth]

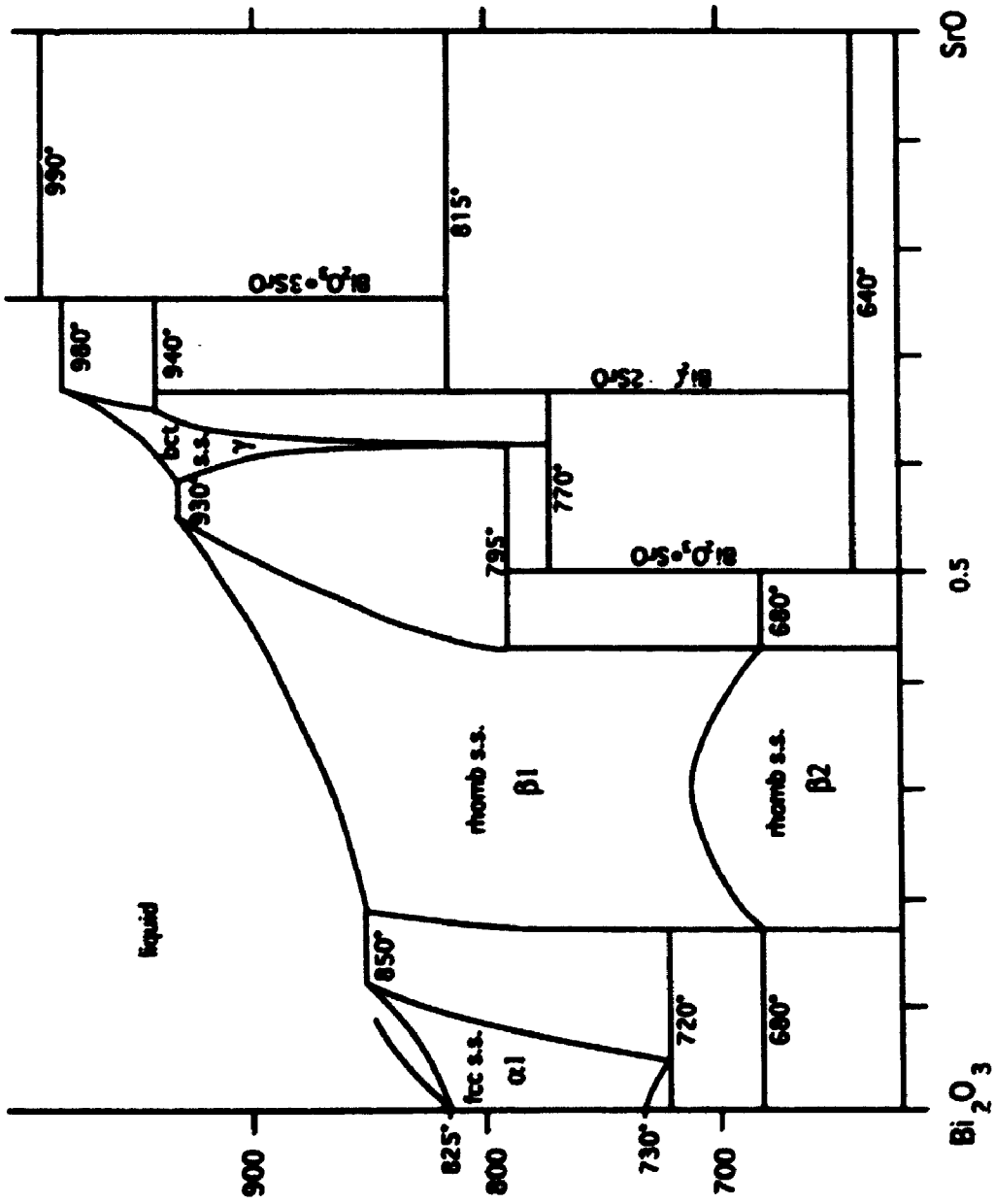

Figure 2.11 Bi_2O_3-SrO phase diagram [proposed by Guillermo *et al.*]

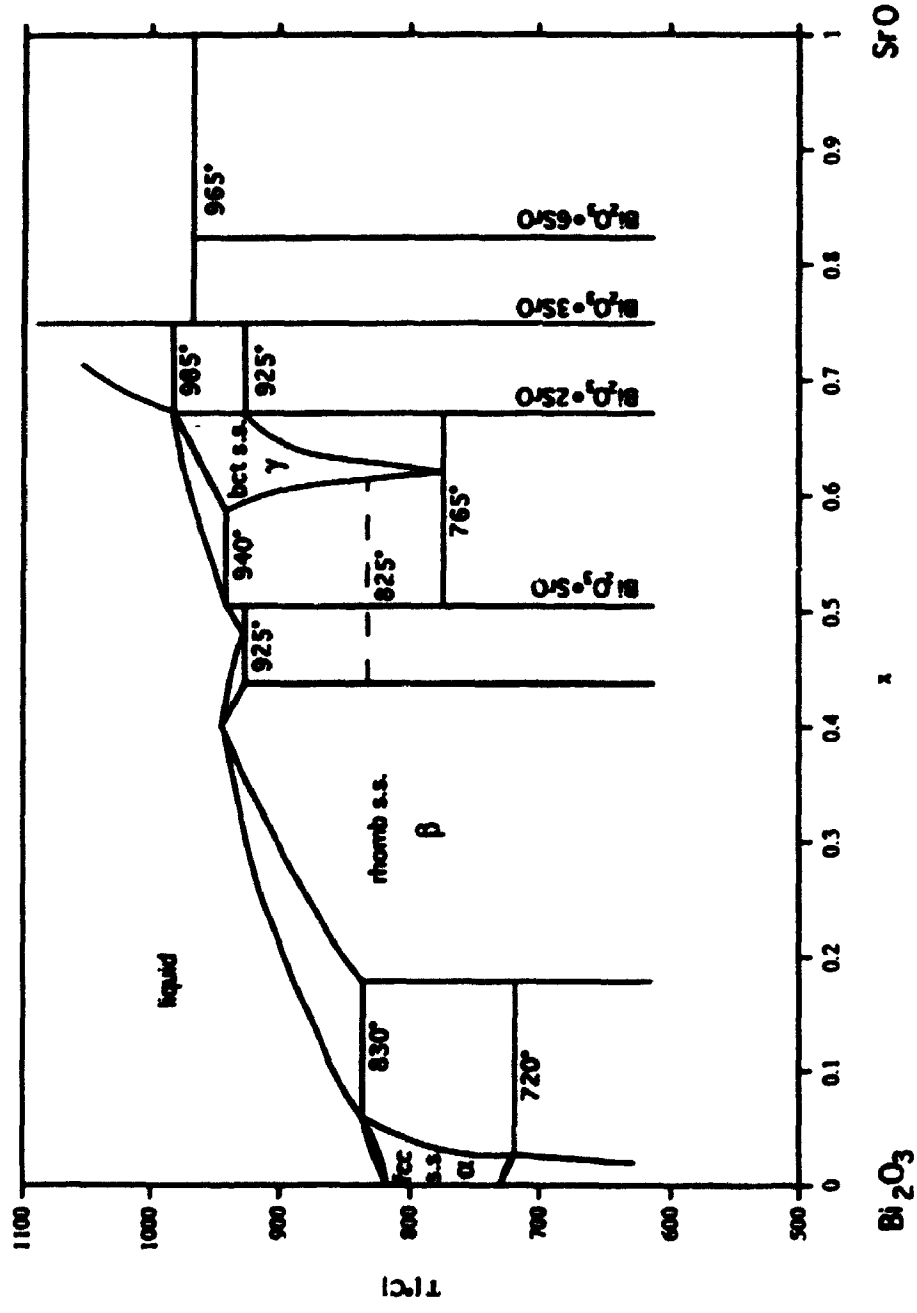

Figure 2.12 Bi_2O_3-SrO phase diagram [proposed by Roth *et al.* and Huang *et al.*]

extended to temperatures just above 600°C and the γ-solid solution boundaries were slightly altered. The composition range of the β-phase solid solution was again confirmed to be $0.18 \leq x \leq 0.43$ but the form of the liquidus and solidus were redrawn to incorporate a congruent maximum at 960 °C and $x \cong 0.42$, but the significance of this composition was not discussed. The authors ignored the high temperature experimental results of Guillermo *et al.* [10], which indicated a $\beta_1 \leftrightarrow \beta_2$ phase transformation, by claiming that no such transition was observed in their study, which was based on the analysis of quenched samples. This conclusion is surprising since Guillermo *et al.* [10] specifically stated that the high temperature β_1 structure could not be retained on quenching, and further, Levin and Roth [18] have questioned studies of Bi_2O_3-MO phase diagrams in which the phases were not studied at temperature and, consequently, might not represent true equilibrium.

A reversible endothermic DTA peak has been observed at T = 626 °C by Watanabe [21] on a sample of β-$(Bi_2O_3)_{1-x}(SrO)_x$ at x = 0.38, in confirmation of the $\beta_2 \leftrightarrow \beta_1$ transformation proposed by Guillermo *et al.* [10].

In addition, Watanabe [21] investigated the stability of the β-phases when heated in air or subjected to high humidity atmospheres. It was found that the barium β-phase decomposed into α-Bi_2O_3 and an unknown phase when heated at 500 °C in air for one week, but that the strontium and calcium β-phases were not affected. All three solid solutions decomposed to α-Bi_2O_3 and an unidentified phase when exposed to water vapour at 50 °C for a few days, or after prolonged storage in plastic bottles at ambient temperatures. In both of these cases, the decomposition was least for Ca and greatest for Ba β-phases . Since this follows the order of the polarizability of the solutes (*i.e.*, Ca>Sr>Ba), it was concluded that the M-O bonds are more important than the Bi-O bonds for the stability of the β-phase.

2.7 β-Phases in Related Systems

The rhombohedral β-phase structure has also been reported [22-23] in the systems $(Bi_2O_3)_{1-x}(Y_2O_3)_x$ and $(Bi_2O_3)_{1-x}(Ln_2O_3)_x$ where Ln = La, Pr, Nd, Sm, Gd, Dy, Er. These systems are of interest because an increase in the solute concentration does not cause an increase in the number of oxygen vacancies. The β-phase containing Y^{3+} in the range $0.215 < x < 0.235$ is of particular interest because of the small size of the Y^{3+} ion, which was included in Table V. This β-phase solid solution is a relatively poor ionic conductor, but at high temperatures it transforms to the cubic α_1-phase which is a good ionic conductor. The reverse transformation from $\alpha_1 \rightarrow \beta$ is highly irreversible, so α_1 can be retained to room temperature and long annealing times are required at intermediate temperatures to restore the β-phase. This annealing time is reduced when $(Bi_2O_3)_{1-x}$ $(Y_2O_3)_x$ is doped with divalent cations such as Ca and Sr . In this context, however, it should be noted that at a molar composition, x, the ratio of bismuth to yttrium is not the same as the ratio of bismuth to the divalent ions, as there are two moles of Y^{3+} ions per molar unit of Y_2O_3 compared to only one mole of Sr^{2+} ions per molar unit of SrO.

The composition dependence of the lattice parameters of $(Bi_2O_3)_{1-x}(Y_2O_3)_x$ are shown in Figure 2.13. The *a* parameters are close agreement with those of the alkali earth doped materials, presented previously in Figure 2.6. The *c* parameters are significantly lower, despite the lower number of oxygen vacancies and decrease as a function of yttrium concentration, in contrast to the trends for $(Bi_2O_3)_{1-x}(MO)_x$. These trends in *c* parameter can be attributed to the much smaller ionic radius of Y^{3+} compared to Bi^{3+}.

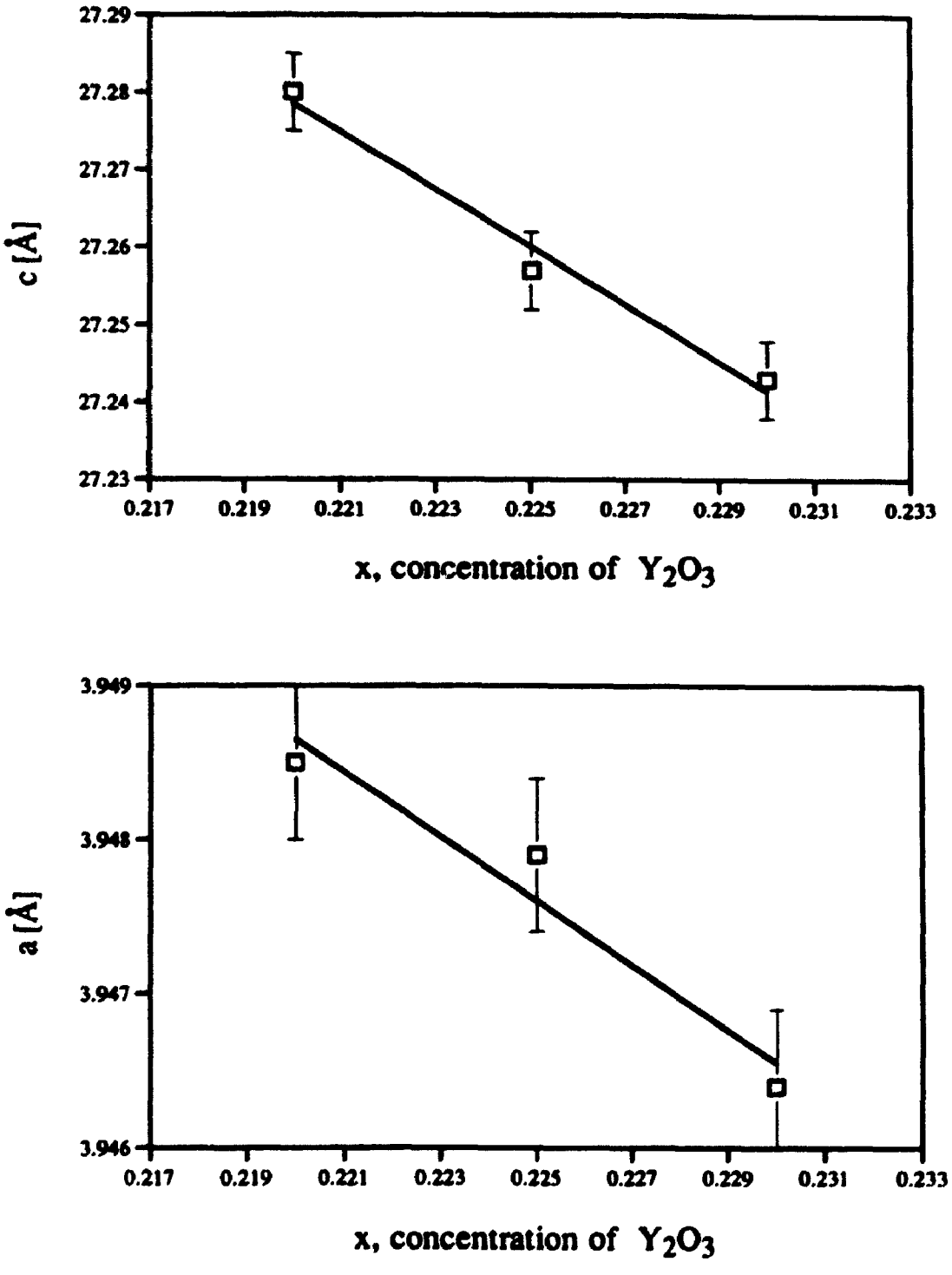

Figure 2.13 Compositional dependence of β-$(Bi_2O_3)_{1-x}(Y_2O_3)_x$ lattice parameters [after Watanabe and Kikuchi]

2.8 Summary

The review of the literature has shown that the rhombohedral cation sublattice of the β-phase has been well established by X-ray and neutron diffraction, while the positions of the oxygen anions have only been explicitly defined in a single neutron diffraction study. The composition dependence of the *c* parameter for β-$(Bi_2O_3)_{1-x}(SrO)_x$ has an anomalously greater slope and an apparently greater scatter in the experimental data compared to the solid solutions containing barium or calcium. A $\beta_1 \leftrightarrow \beta_2$ phase transformation, as evidenced by DTA and a sharp discontinuity in the temperature dependence of the *c* parameters, has been observed at a temperature related to an increase in ionic conductivity. These findings have been incorporated into a succession of equilibrium phase diagrams, the most recent of which has cast doubt on the $\beta_1 \leftrightarrow \beta_2$ phase transformation, leaving the origin of the conductivity increase unexplained.

The present work is focused on a detailed X-ray diffraction investigation of the composition and temperature dependence of the lattice parameters of the β-$(Bi_2O_3)_{1-x}(SrO)_x$ phase to establish the nature of the alleged $\beta_1 \leftrightarrow \beta_2$ phase transformation, and its significance with respect to the high ionic conductivity of this material.

CHAPTER 3 - Experimental Procedures

3.1 Sample Preparation

Three sets of β-phase samples were prepared for this investigation. The first set was composed of β-$(Bi_2O_3)_{1-x}(SrO)_x$ ceramics with compositions x = 0.20, 0.28, 0.32, and 0.40, which were prepared by Dr. Y. Shen at the University of Notre Dame. Proportionate amounts of Bi_2O_3 (99.9%) and $Sr(NO_3)_2$ (99.9%) powders were reacted in the solid state to produce 20 g samples of the required compositions. The powders were mixed and ground, and then calcined in air for 20 h at 800 °C. The reacted powders were uniaxially pressed at 62 MPa to produce discs 25 mm in diameter and 5 mm in thickness, which were sintered for 20 h in air at 800 °C. After sintering, the disks were crushed, ground, pressed and refired two additional times, to obtain improved homogeneity.

The second set of β-$(Bi_2O_3)_{1-x}(SrO)_x$ samples, with compositions x = 0.18, 0.20, 0.24, 0.28, 0.32, 0.36, 0.40, and 0.42, was prepared at UWO by the solid state reaction of proportionate mixtures of 99.9% Bi_2O_3 [ÆSAR] and 99.9% $SrCO_3$ [ÆSAR] to yield 20 g samples. This level of precursor purity was considered sufficient to investigate the phase transformation. The precursor powders were mixed by hand in an agate mortar, uniaxially pressed at 62 MPa and reacted at 727 °C (*i.e.*, below the solidus) for 20 h followed by air-cooling in the furnace. The slightly sintered compacts were reground in the agate mortar, pressed and refired at 727 °C two additional times, to obtain improved powder homogeneity. An SEM examination of the final powders, as used in the diffraction experiments, revealed irregularly shaped particles with no indication of a platey morphology from 2 - 30 μm in diameter with no indication of second phases.

The third set of samples was composed of ceramics from the ternary system (Bi_2O_3)-(Y_2O_3)-(SrO), which was investigated to compare the relative effects of ionic size and ionic valence on the lattice parameters of the β-phase. As shown by the compositions listed in Table VI, the ratio of trivalent to divalent cations was held constant in two sub-sets of these compositions, while in a third sub-set the ratio of solvent (Bi^{3+}) ions to solute (Y^{3+},Sr^{2+}) ions was held constant. These samples were prepared at UWO by the solid state reaction of proportionate mixtures of 99.9% Bi_2O_3 [ÆSAR], 99.9% Y_2O_3 [ÆSAR] and/or 99.9% $SrCO_3$ [ÆSAR] to produce 20 g samples of the desired compositions. Powders of the precursors were mixed by hand in an agate mortar, uniaxially pressed at 62 MPa and reacted at 700 °C for 10 h, followed by air-cooling in the furnace. Since X-ray examination showed that some of these samples included peaks of the δ-Bi_2O_3 phase structure after this treatment, these ceramics were further annealed at 680 °C for 48 hr in order to produce the β-phase.

Table VI

Compositions of (Bi_2O_3)-(Y_2O_3)-(SrO) Samples

Composition	Specifications
$(Bi_2O)_{0.64}(SrO)_{0.36}$ $[(Bi_2O_3)_{0.496}(Y_2O_3)_{0.144}](SrO)_{0.36}$	Constant trivalent : divalent cation ratio at 0.64:0.36
$(Bi_2O_3)_{0.8}(SrO)_{0.2}$ $[(Bi_2O_3)_{0.62}(Y_2O_3)_{0.18}](SrO)_{0.2}$	Constant trivalent : divalent cation ratio at 0.80:0.20
$(Bi_2O_3)_{0.64}(SrO)_{0.36}$ $(Bi_2O_3)_{0.703}[(Y_2O_3)_{0.099}(SrO)_{0.198}]$ $(Bi_2O_3)_{0.78}(Y_2O_3)_{0.22}$	Constant solvent : solute ratio at 0.78(Bi^{3+}):0.22 (Y^{3+},Sr^{2+})

3.2 X-Ray Diffraction under Ambient Conditions

Room temperature X-ray diffraction experiments were performed with a Philips PW1050/65 diffractometer, with the theta : two theta geometry illustrated in Figure 3.1. This diffractometer was modified by incorporating a Bicron scintillation detector and a Superior Electric stepper motor (with a minimum step size of 0.005 °) controlled by a Radix Databox, which enabled the angle and intensity coordinates of step scanned diffraction patterns to be recorded on the hard drive of a 486DX66ii Mustang PC computer. The copper target X-ray tube was operated at 34 kV and 24 mA, with a nickel foil diffracted beam filter to remove the Cu K_β radiation. The instrumental settings and step scanning conditions to provide optimum intensities for crystal structure identification and optimum resolution for precision lattice parameter determination are given in Table VII.

Table VII

Instrumental Settings for the Philips Diffractometer

Setting	Structure Identification	Lattice Parameters
Goniometer radius	170 mm	170 mm
Limiting resolution	0.035 °2θ	0.035 °2θ
Soller slits	Both beams	Both beams
Divergent slit	1 ° (<90 °2θ); 4 ° (>90 °2θ)	1 ° (<90 °2θ); 4 ° (>90 °2θ)
Receiving slit	0.2 mm	0.1 mm
Angular step width	0.05 °	0.03 °
Preset time	2 sec	1 sec
Effective scanning rate	1.5 °/min	1.8 °/min

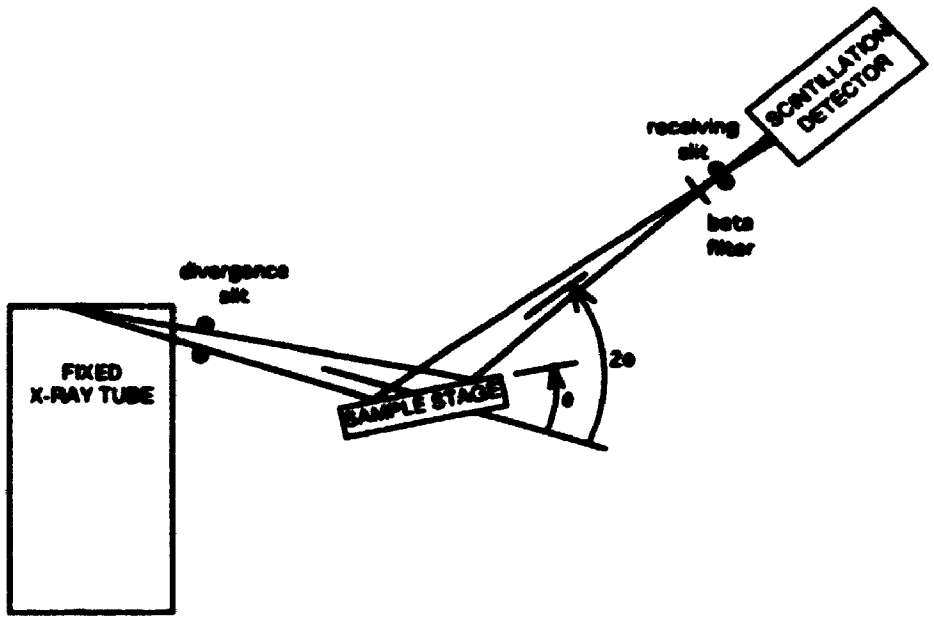

Figure 3.1 Schematic of the theta : 2theta geometry of the Philips diffractometer

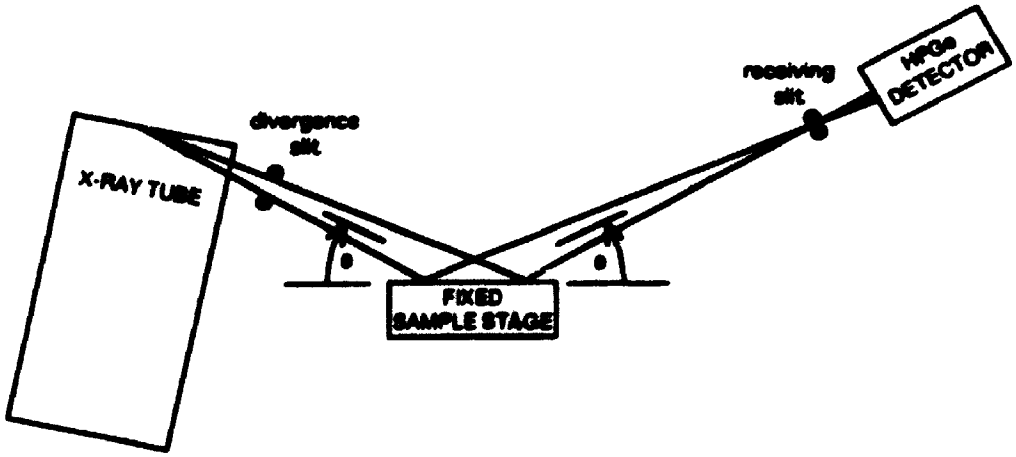

Figure 3.2 Schematic of the theta : theta geometry of the Scintag diffractometer

X-ray samples for examination under ambient conditions were prepared by the so-called "smear" technique, in which a small quantity of finely ground powder is sprinkled onto a glass slide smeared with a thin film of silicon grease. Excess powder is removed by inverting and gently tapping the slide. This technique has previously been demonstrated to yield highly reliable and reproducible X-ray diffraction patterns for precision lattice parameter determination, while minimizing errors due to preferred orientation.

3.3 High Temperature X-Ray Diffraction

High temperature X-ray diffraction was performed with a Bühler high temperature chamber mounted on a Scintag XDS2000 automated diffractometer, equipped with an EE&G Ortec HPGe detector. The copper target X-ray tube was operated at 45 kV and 40 mA. Since the solid state detector has very high signal to noise characteristics, and sufficient energy resolution to permit pulse height discrimination of the Cu K_β radiation, the need for a nickel foil β filter was eliminated, which effectively doubled the intensity of the Cu K_{α_1} radiation. The Scintag goniometer was set in the theta : theta mode, in which the X-ray tube and detector move while the sample remains fixed in the horizontal position, as illustrated in Figure 3.2. When used in this mode, the radius of the goniometer is increased to 250 mm, which increases its inherent resolution and also provides additional space for accommodating the high temperature attachment with its associated electrical leads, water cooling tubes, and vacuum pumps, as shown in Figure 3.3. The sample was mounted within the high temperature chamber on a platinum-rhodium heater strip, the temperature of which was measured and controlled to ±1 °C over the experimental range from 27 °C to 800 °C, using a Pt/Pt-13Rh thermocouple.

The instrumental settings to provide optimum intensities for crystal structure identification and optimum resolution for precision lattice parameter determination are give

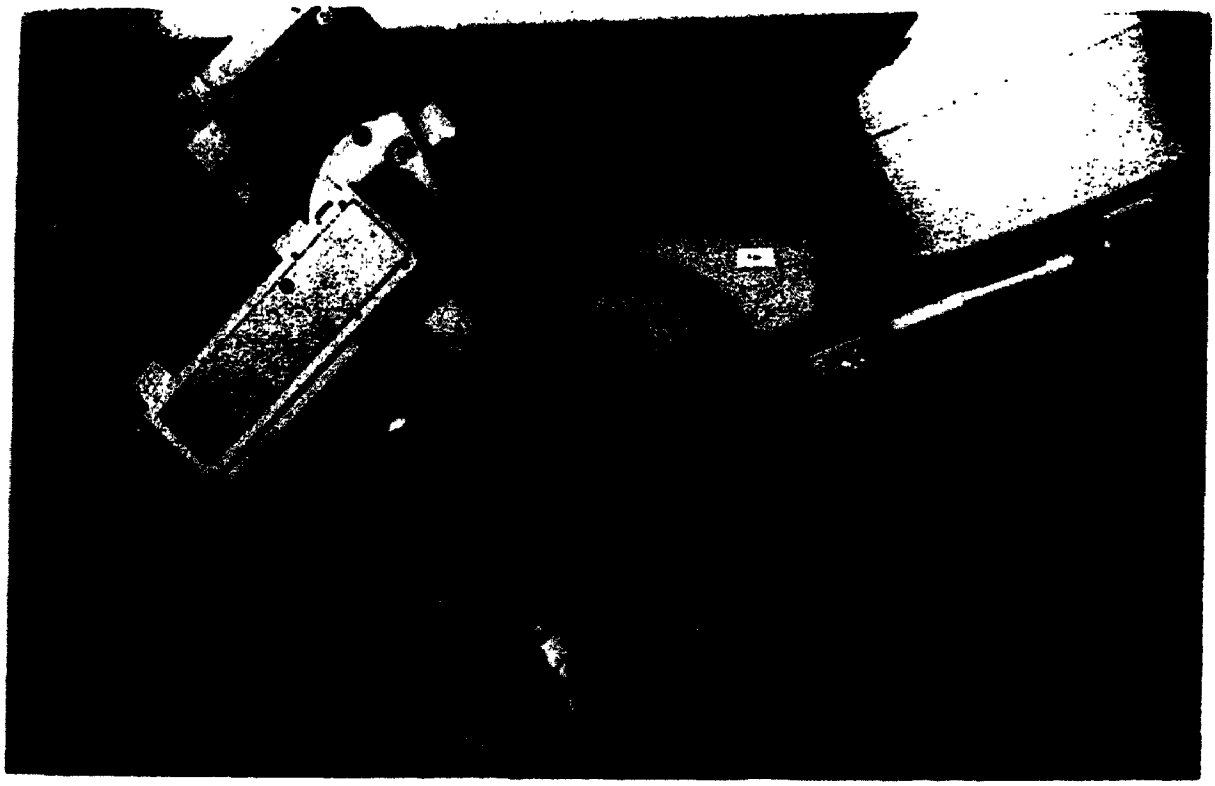

Figure 3 3 Photograph of the Bühler high temperature chamber

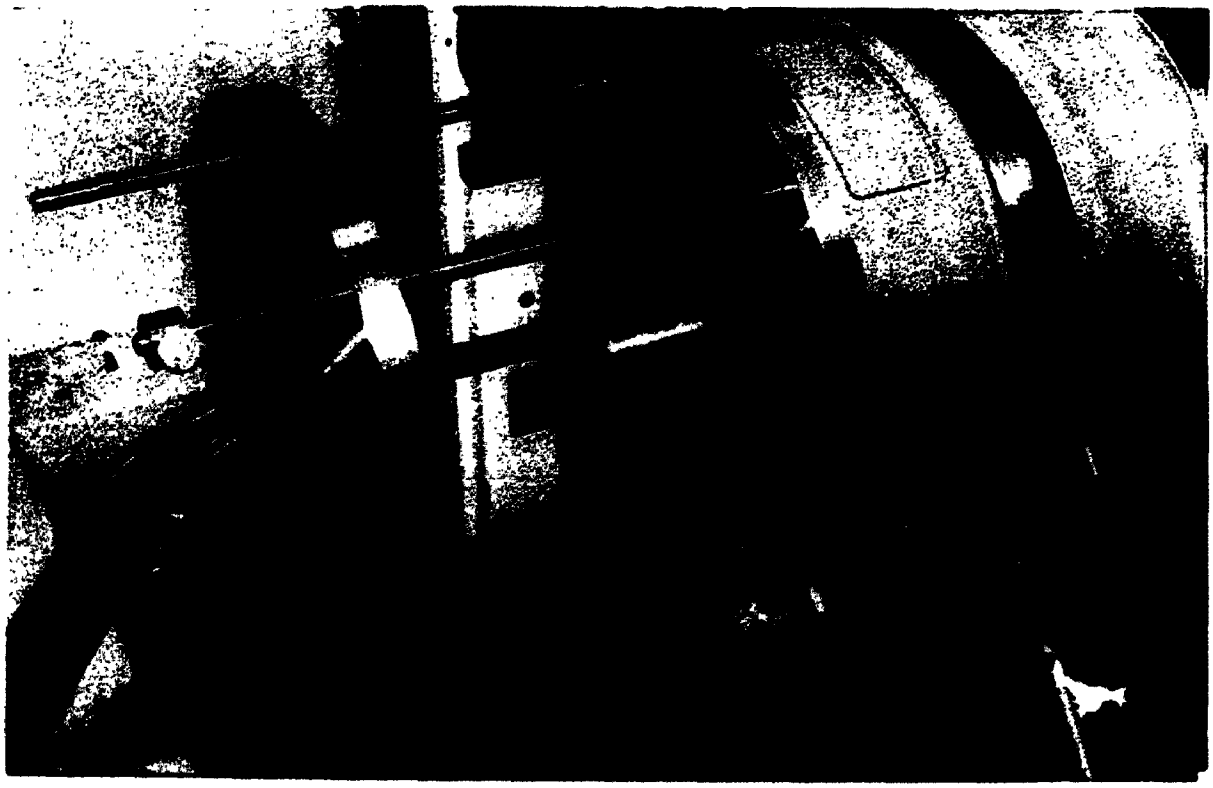

Figure 3.4 Photograph of the low temperature attachment for the Bühler chamber

in Table VIII. Diffraction data were collected in the "continuous scan" mode, in which counts are collected over a preset angular range, while the x-ray tube and detector (which together determine the Bragg angle 2θ) are advanced at a set rate, with the total counts assigned to the midpoint of this angular range for data acquisition purposes. This mode is subtly different from the "step scan" mode used for the Philips diffractometer, where the counts are accumulated for a preset time at a fixed angular step position, before advancing to the next position.

Table VIII

Instrumental Settings for the Scintag Theta : Theta Diffractometer

Setting	Structure Identification	Lattice Parameters
Goniometer radius	250 mm	250 mm
Limiting resolution	0.024 °2θ	0.024 °2θ
Soller slits	Both beams	Both beams
Divergent slit	1 ° (<90 °2θ)	1 ° (<90 °2θ)
Receiving slit	0.5 mm	0.3 mm
Preset angular range	0.05 °	0.03 °
Continuous scanning rate	5 ° (2θ)/min	1 ° (2θ)/min
Effective preset time	0.6 seconds	1.8 seconds

Samples for high temperature examination were prepared by depositing a small quantity of finely ground powder onto the centre of the platinum-rhodium heater strip. The temperature gradient over a length of ±2.5 mm from the centre of the hot zone has been shown to be less than ±2 °C [B.Cavin, 1st Scintag Workshop on High Temperature X-Ray Diffraction, Sunnyvale, CA, March 1991]. To improve the thermal contact between the powder sample and the heater strip, a drop of acetone was added to distribute the powder

evenly over the central (hot) zone of the strip and allowed to evaporate fully before initiating diffraction scans. Although this sample preparation method may enhance the preferred orientation of platy particles, this effect was of relatively little consequence for the high temperature work, which was directed at the measurement of peak positions rather than relative intensities. High temperature diffraction experiments are initially conducted with the sample in vacuum, but after preliminary tests revealed that the Bi_2O_3-SrO samples were prone to decomposition in reduced pressures, even at temperatures less than 600°C, all subsequent experiments were conducted in air at atmospheric pressure.

3.4 Low Temperature X-Ray Diffraction

Low temperature X-ray diffraction experiments were performed with the Scintag XDS2000 diffractometer, using a specially constructed attachment for the Bühler high temperature chamber. The attachment consisted of an adapter plate supporting a miniature Joule-Thomson refrigerator, which could be substituted for the Pt/Rh heater assembly and thereby make use of the vacuum facilities and sample alignment adjustments of the high temperature chamber, as shown in Figure 3.4. Using this device, the temperature of the cold stage could be controlled to ±1 K over the range from 400 K down to 65 K. A detailed description of the attachment, and its operating characteristics, are given in a paper published in *Advances in X-ray Analysis*, Vol. 39 (1994), which is reprinted as Appendix I of this thesis.

The instrumental settings and scanning conditions for low temperature measurements with the Scintag diffractometer were the same as those listed in Table VIII for the high temperature experiments, except that all low temperature scans were conducted at a reduced pressure of approximately 10^{-3} Torr, using the roughing pump attached to the Bühler chamber. This condition was necessary to prevent condensation and subsequent

POWD12 routine developed by Deane K. Smith for the modeling of d-spacings and relative peak intensities of X-ray, electron and neutron diffraction patterns, based on inputs of crystal structure data. This program is sophisticated enough to incorporate features such as peak shape considerations, partial occupancy of atom positions, and Lorentz and polarization effects, so that a detailed model diffraction pattern may be computed and compared with experimentally observed patterns. Options in the μ-POWD program were also used for calculating bond lengths and drawing model unit cells, but the latter feature was not found be particularly versatile.

A number of commercial computer programs are available for refining lattice parameters of indexed structures as well as correcting for systematic errors including axial divergence, sample surface displacement, specimen transparency, and zero 2θ missetting. Several of these routines also include options to utilize internal and/or external standard corrections in an effort to improve the precision of the refinement. A detailed experimental examination, published in *Advances in X-Ray Analysis* , Vol. 38 (1993) and reprinted as Appendix II of this thesis, has confirmed that the error in lattice parameters due to sample surface displacement, which is a function of $\cos\theta\cot\theta$, is the most significant systematic error in Bragg-Brentano powder diffractometry. Since precision lattice parameter determination is the essence of the present investigation, an experimental evaluation of the effectiveness of the available computer programs for dealing with surface displacement and other systematic errors was considered to be an essential preliminary to the experimental work of this thesis. As described in a publication printed in *Advances in X-Ray Analysis* , Vol. 39 (1994) and reprinted as Appendix III, internal standards were found to cause uncertainty in peak positions when a peak, or peaks, of the standard inadvertently overlap peaks of the sample under investigation. It was also shown that external standards can actually reduce the precision of a lattice parameter refinement, when using a well aligned instrument. Further, it was demonstrated that lattice parameters can be routinely

POWD12 routine developed by Deane K. Smith for the modeling of d-spacings and relative peak intensities of X-ray, electron and neutron diffraction patterns, based on inputs of crystal structure data. This program is sophisticated enough to incorporate features such as peak shape considerations, partial occupancy of atom positions, and Lorentz and polarization effects, so that a detailed model diffraction pattern may be computed and compared with experimentally observed patterns. Options in the μ-POWD program were also used for calculating bond lengths and drawing model unit cells, but the latter feature was not found be particularly versatile.

A number of commercial computer programs are available for refining lattice parameters of indexed structures as well as correcting for systematic errors including axial divergence, sample surface displacement, specimen transparency, and zero 2θ missetting. Several of these routines also include options to utilize internal and/or external standard corrections in an effort to improve the precision of the refinement. A detailed experimental examination, published in *Advances in X-Ray Analysis* , Vol. 38 (1993) and reprinted as Appendix II of this thesis, has confirmed that the error in lattice parameters due to sample surface displacement, which is a function of $\cos\theta\cot\theta$, is the most significant systematic error in Bragg-Brentano powder diffractometry. Since precision lattice parameter determination is the essence of the present investigation, an experimental evaluation of the effectiveness of the available computer programs for dealing with surface displacement and other systematic errors was considered to be an essential preliminary to the experimental work of this thesis. As described in a publication printed in *Advances in X-Ray Analysis* , Vol. 39 (1994) and reprinted as Appendix III, internal standards were found to cause uncertainty in peak positions when a peak, or peaks, of the standard inadvertently overlap peaks of the sample under investigation. It was also shown that external standards can actually reduce the precision of a lattice parameter refinement, when using a well aligned instrument. Further, it was demonstrated that lattice parameters can be routinely

determined to an accuracy to one part in ten thousand without the use of external or internal standards, by using computational extrapolation with respect to $\cos\theta\cot\theta$. On the basis of this finding, the Scintag version of the Vogel and Kempter computational extrapolation program, utilizing the $\cos\theta\cot\theta$ error function, is routinely used in this laboratory to determine the lattice parameters from diffraction data collected with the Scintag diffractometer, providing that the structure is either cubic, tetragonal, or orthorhombic. Although the Vogel and Kempter software includes a hexagonal extrapolation option, it was found that errors in the program source code caused significant deviations from the correct lattice parameter values for all hexagonal structures.

In Appendix III, the Scintag version of the Burnham routine, LCLSQ, was found to yield lattice parameters with considerably less precision when a range of errors were refined simultaneously. However, when only the sample surface displacement error was allowed to be refined, the results were equivalent in precision to the Vogel and Kempter method, and LCLSQ was therefore utilized for the analysis of the diffraction patterns recorded with the Scintag diffractometer . The software used for determining lattice parameters from data collected with the Philips diffractometer was the MDI version of the Argonne National Laboratory routine B106, which also allowed for the simultaneous mathematical refinement of lattice parameters and sample surface displacement errors by a least squares routine similar to the Burnham program. When using either the ANL B106 Program, or the LCLSQ Program, the errors in lattice parameter determination indicated in the presentation of the results were estimated from the standard deviations of measurements of the individual peaks.

CHAPTER 4 - Experimental Results

4.1 Preliminary Experiments

4.1.1 Conductivity Measurements (performed at the University of Notre Dame)

The electrical conductivity of the sintered discs was measured in air at temperatures from 400°C to 800°C with an AC impedance spectrometer by Dr. Y. Shen at the Center for Sensor Materials, University of Notre Dame. Sputtered Au-Pd films provided electrical contacts, and the ceramics were heated in a tube furnace, with temperature control to ±2 °C. The electrical conductivities, summarized in Table IX, were detemined from the real axis intercept of the complex impedence recorded over the range from 100 mHz to 70 MHz.

Table IX
High Temperature Electrical Conductivity of β-$(Bi_2O_3)_{1-x}(SrO)_x$ Ceramics

	Electrical Conductivity $[\Omega\text{-cm}]^{-1}$			
Temperature [°C]	x = 0.20	x = 0.28	x = 0.32	x = 0.40
400	0.000753	0.000265	0.0003624	0.000257
450	0.001785	0.000688	0.0009848	0.0008801
500	0.003905	0.001613	0.002552	0.002875
550	0.00841	0.003354	0.005986	0.008478
575	0.0123	-	-	0.01399
600	0.01855	0.006762	0.01161	0.02304
625	0.02893	0.009636	0.01689	0.04643
650	0.06384	0.01448	0.02609	0.07794
675	0.2482	0.02073	0.06575	0.09947
700	0.4533	0.08983	0.1776	0.1210
725	-	0.3105	0.2188	-
750	0.6102	0.3561	0.2415	0.1659
800	0.7843	0.4496	0.3276	0.2122

The conductivities measured for the x = 0.20, 0.28, and 0.40 compositions are plotted in Figure 4.1 as data points superimposed on solid lines, which refer to the conductivity results of Boivin *et al.* [11] for equivalent compositions. Given the sensitivity of the conductivity to the porosity of the sintered ceramics, as discussed by Takahashi *et al.* [16], these results are seen to be in good agreement. This finding confirms that samples used in this work are of comparable quality to those samples utilized by Conflant *et al.* [13], Boivin *et al.* [11], Guillermo *et al.* [10], and Takahashi *et al.* [16].

4.1.2 Preliminary High Temperature X-ray Diffraction Experiments

Initial high temperature X-ray diffraction studies on the β-$(Bi_2O_3)_{1-x}(SrO)_x$ samples prepared by Dr. Shen confirmed that the samples were susceptible to decomposition when annealed under vacuum at temperatures above 550°C, as mentioned previously by Takahashi *et al.* [16]. Consequently the remaining high temperature experiments were conducted in air. Out of concern for a possible reaction of platinum with bismuth, Guillermo *et al.* [10] took pains to use gold foils and crucibles for their high temperature experiments. As it was normal practice at UWO to use Kanthal heater strips instead of platinum alloys in the interest of economy, initial experiments were performed with this material. However, as it was found that the Kanthal heater strips reacted with the β-phases at high temperatures, forming a dark orange reaction product which adhered strongly to the Kanthal, this practice was discontinued. Subsequent experiments were performed with a platinum rhodium heater strip without any noticeable degradation of either sample or heater strip. Platinum heater strips were earlier used in the high temperature XRD experiments of Levin and Roth [18], who did not report any deleterious effects.

The intensities of the 00•l diffraction peaks are frequently enhanced when β-phase samples are held at temperatures above 600 °C in the diffractometer furnace for long times.

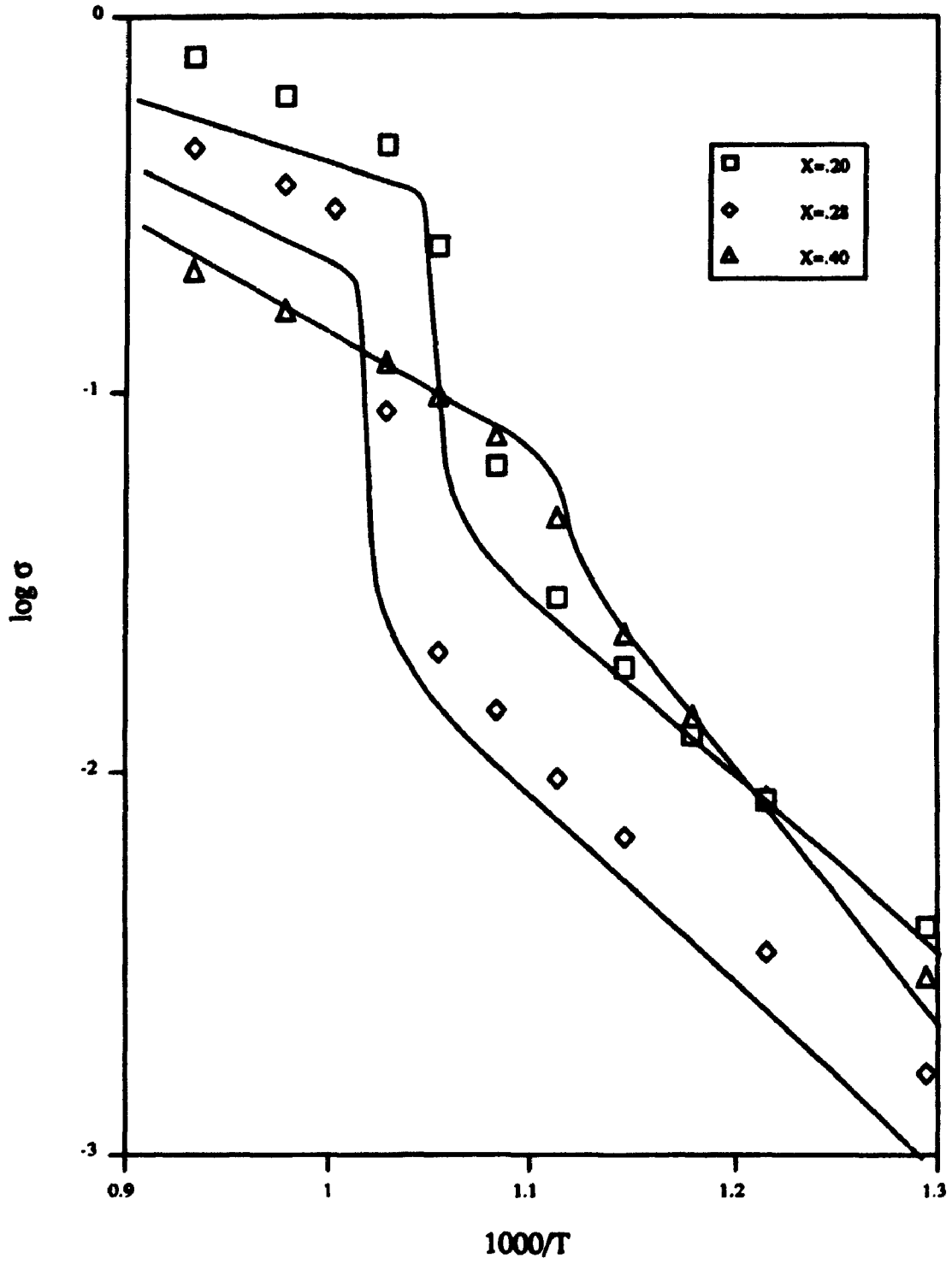

Figure 4.1 High temperature ac conductivity of β-$(Bi_2O_3)_{1-x}(SrO)_x$ ceramics (data points) compared with measurements of Boivin et al. (solid lines)

It is uncertain whether this effect is due to a preferred orientation for recrystallization and grain growth of the powder samples, or whether thermal agitation allows the platey particles to settle onto the heater strip. This effect is irreversible and thus not related to the reversible electrical conductivity transition, consequently it was not investigated further.

At room temperature the samples were all a bright yellow colour. Samples removed from a muffle furnace at temperatures above 700°C were a darker orange, but this colour changed to bright yellow during cooling to room temperature. This observation of a reversible colour change has not been noted in the literature and may relate to the $\beta_1 \leftrightarrow \beta_2$ transformation proposed by Guillermo *et al.* [10].

4.2 Structure Identification

Qualitative XRD scans on all of the β-$(Bi_2O_3)_{1-x}(SrO)_x$ samples yielded diffraction patterns which could be indexed as a single hexagonal phase with sharp diffraction peaks, as shown in Figure 4.2 for the composition $x = 0.32$. In contrast to the broad diffuse peaks reported by Tilley [6], the peaks of the β-phase samples are only slightly broader than those of the NIST SRM640b 2θ / d-spacing standard silicon powder over the same range of 2θ under the same instrumental conditions.

The midpoint composition of the β-$(Bi_2O_3)_{1-x}(SrO)_x$ phase ($x = 0.28$) was selected for more detailed structural analysis. Diffraction patterns over the ranges $5 \leq 2\theta \leq 40$ and $40 \leq 2\theta \leq 140$ were obtained using the instrumental settings for structure identification described in Table VII. All of the observed peaks could be indexed using the hexagonal (rhombohedral) space group $R\bar{3}m$, as shown in Figure 4.3(a-b) and Figure 4.4(a-b).

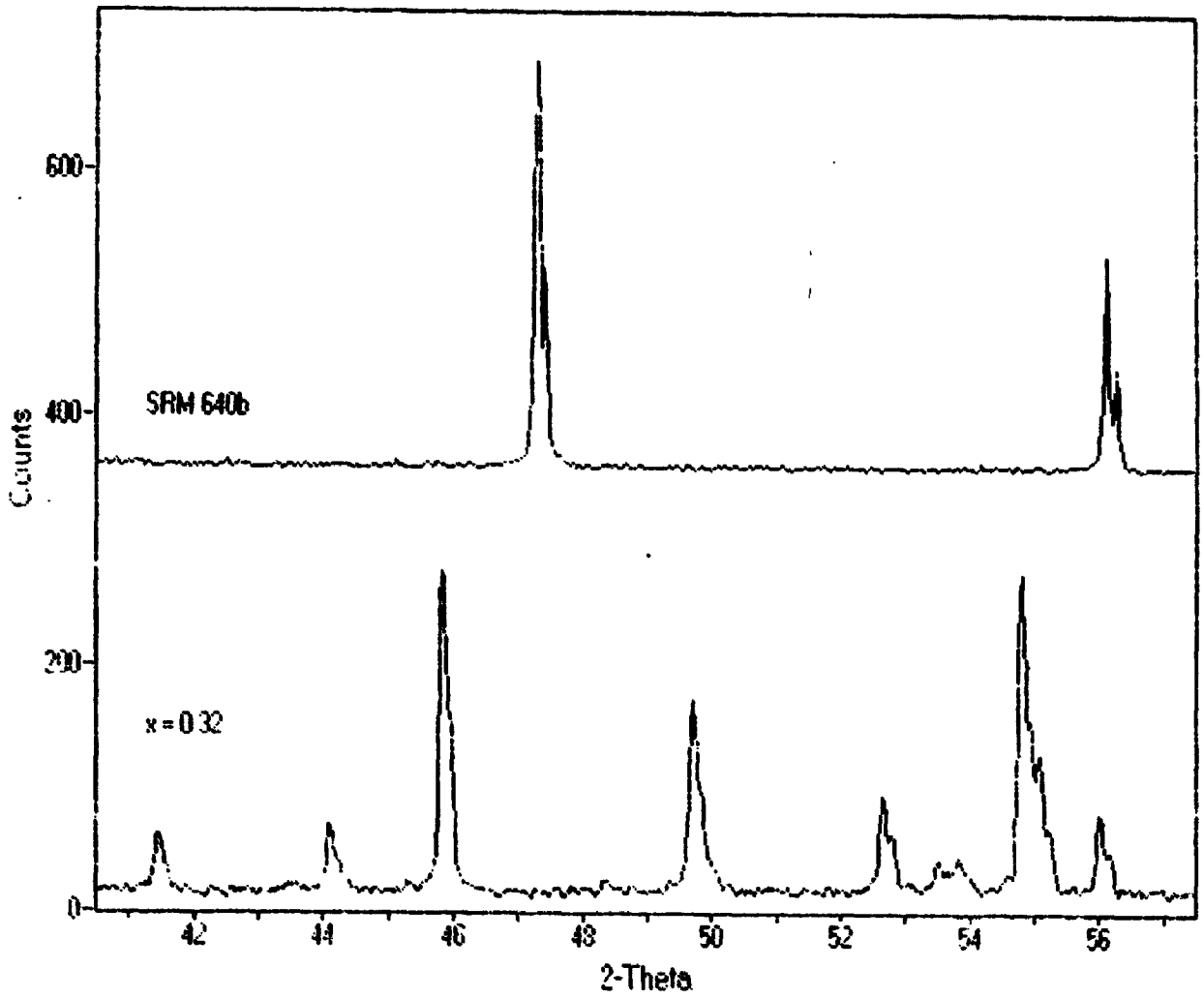

Figure 4.2 **Diffraction patterns of : (bottom) β-$(Bi_2O_3)_{0.68}(SrO)_{0.32}$ and (top) Si (NIST SRM640b) powder 2 θ / d-spacing standard**

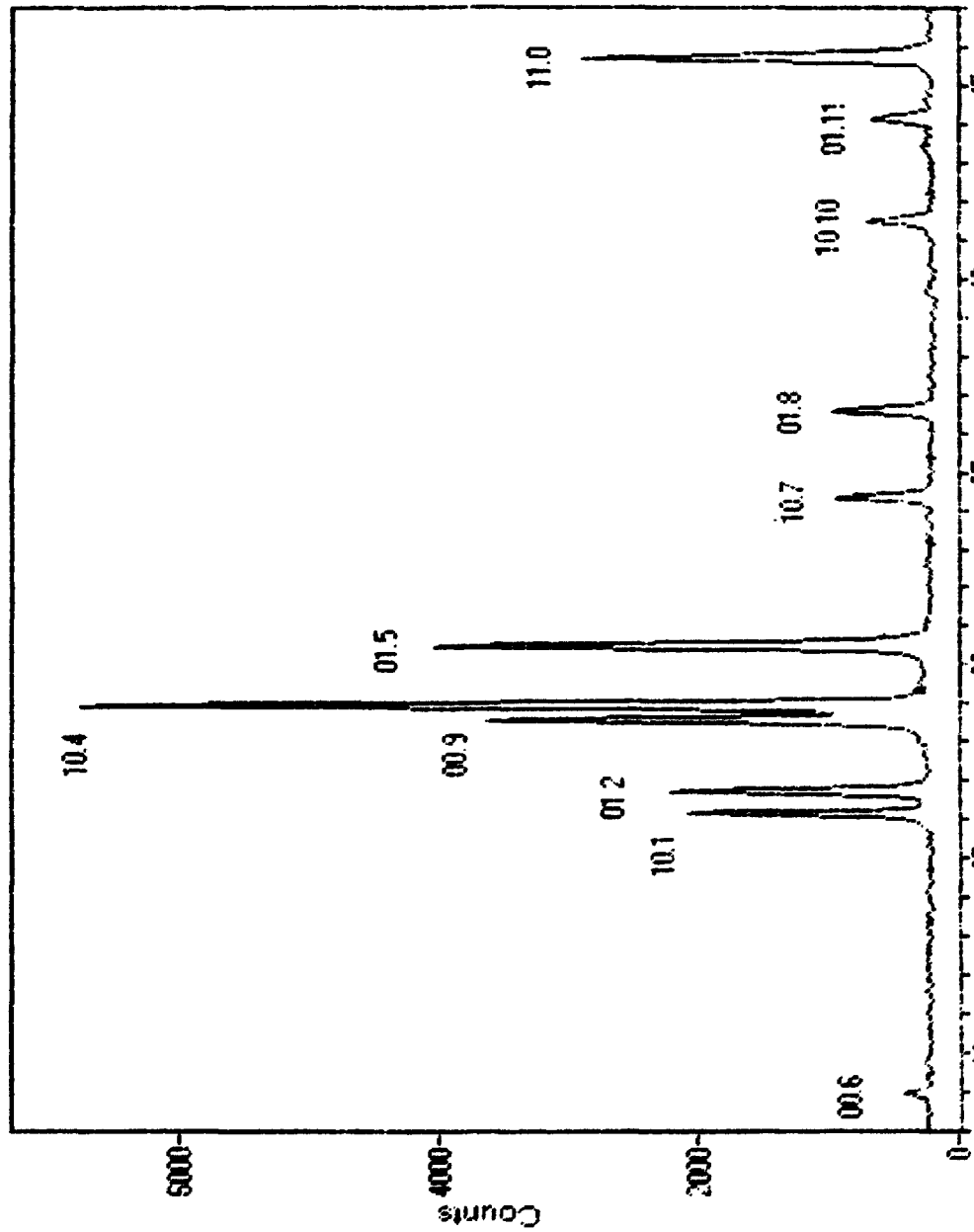

Figure 4.3a Indexed room temperature diffraction pattern of β-(Bi_2O_3)$_{0.72}$(SrO)$_{0.28}$ over the angular range 18°-47° (1° divergence slit)

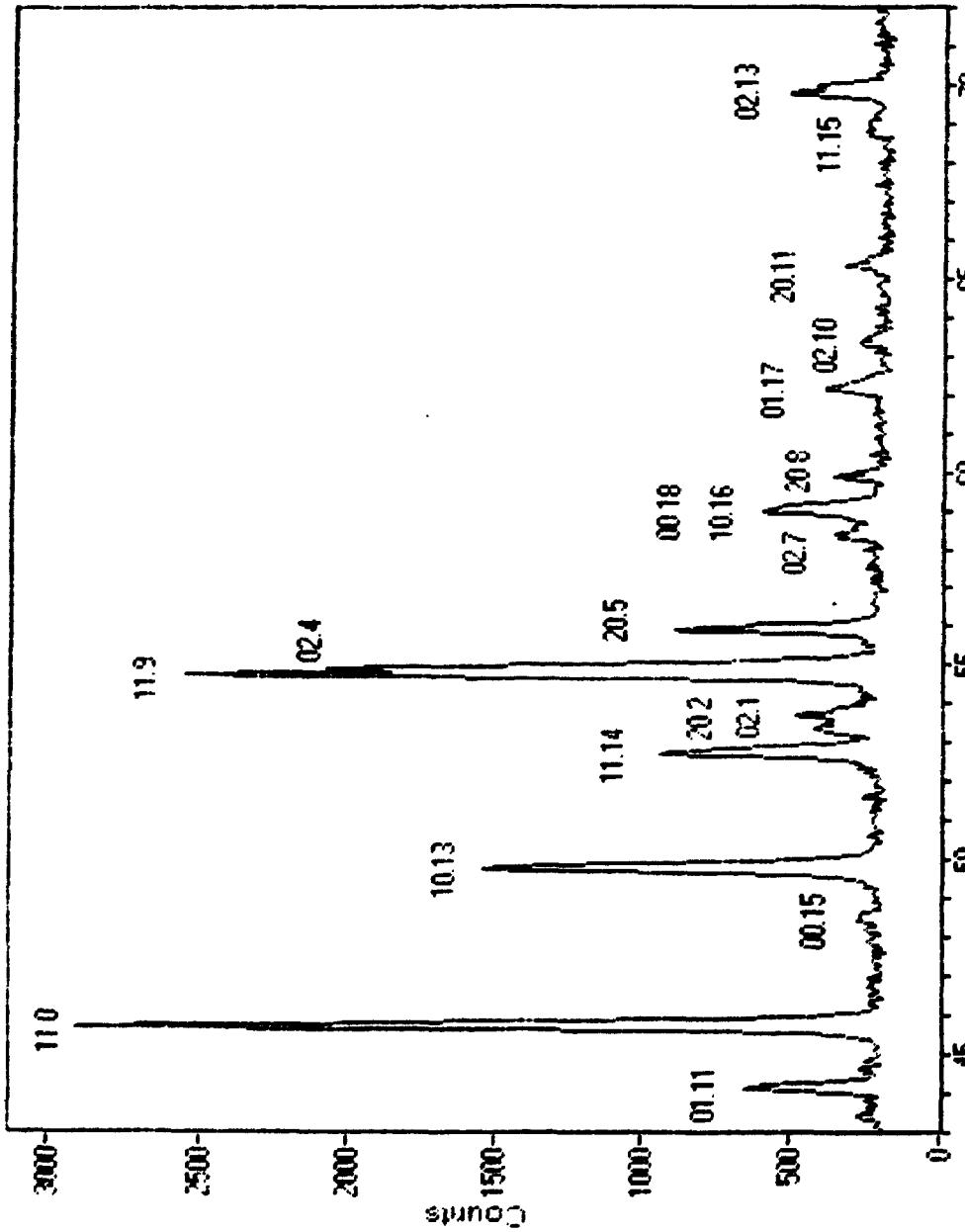

Figure 4.3b Indexed room temperature diffraction pattern of β-(Bi2O3)0.72(SrO)0.28 over the angular range 43°-72° (1° divergence slit)

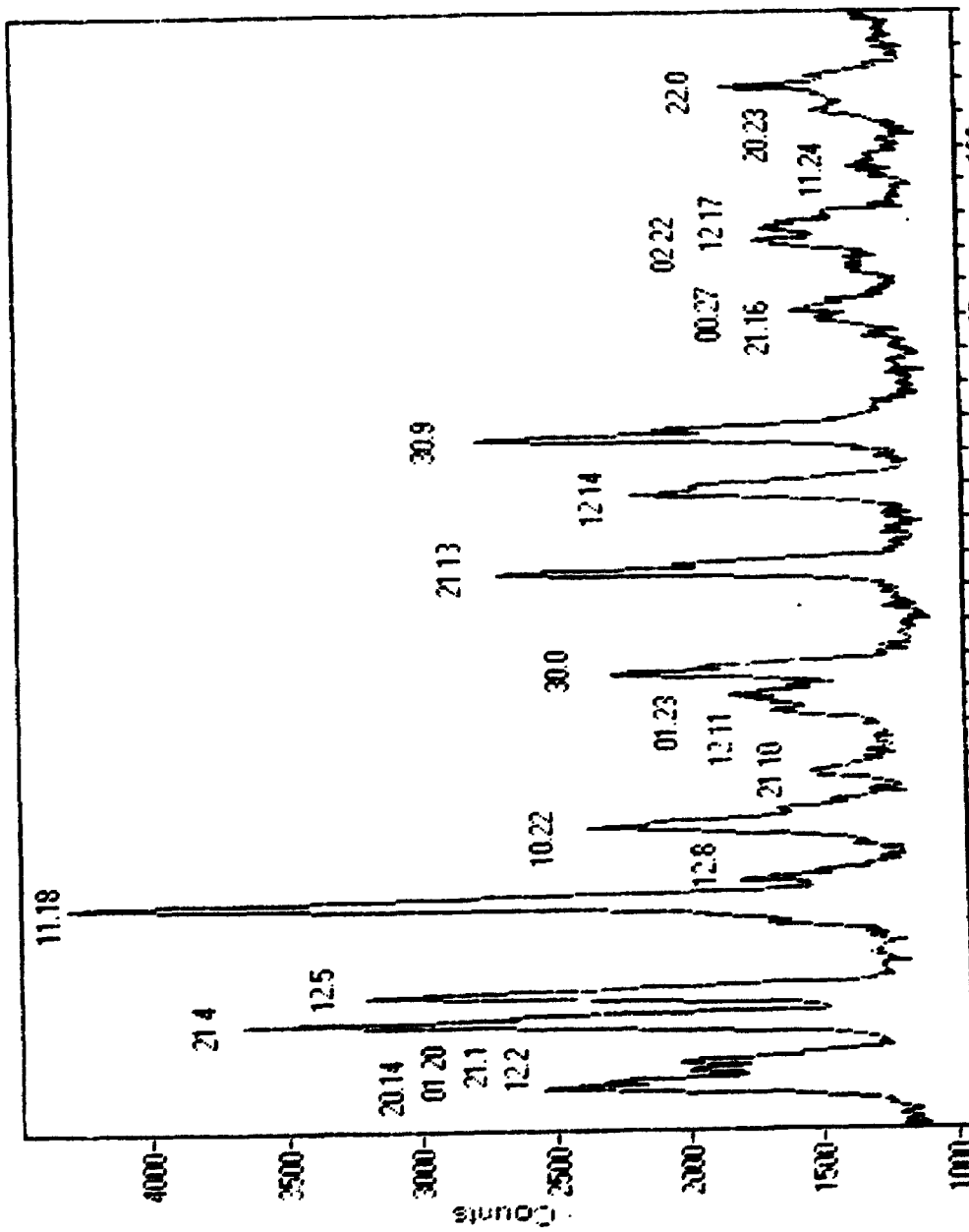

Figure 4.4a Indexed room temperature diffraction pattern of β-(Bi2O3)0.72(SrO)0.28 over the angular range 71°-104° (4° divergence slit)

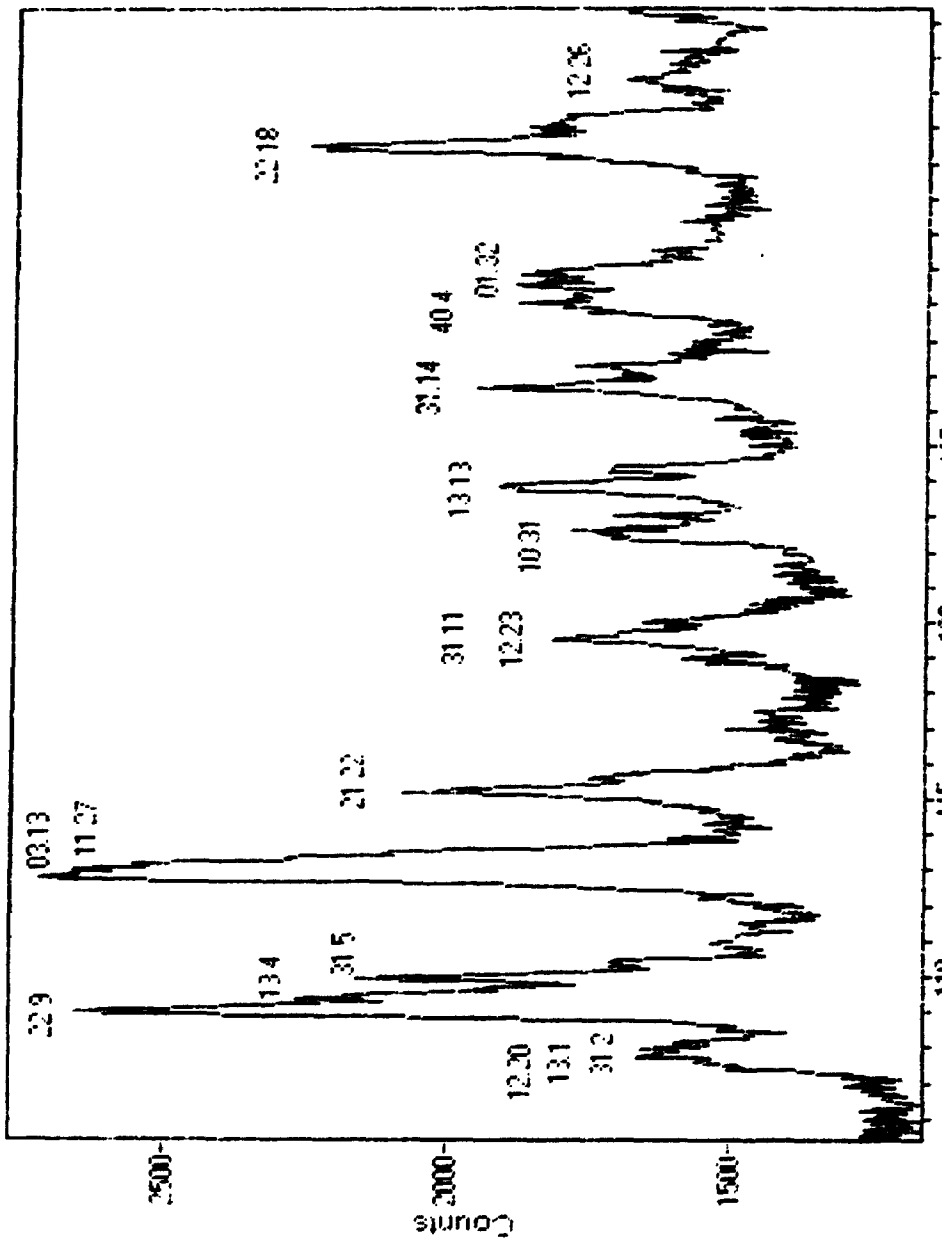

Figure 4.4b Indexed room temperature diffraction pattern of β-(Bi_2O_3)$_{0.72}$(SrO)$_{0.28}$ over the angular range 105°-138° (4° divergence slit)

4.3 Composition Dependence of Lattice Parameters

4.3.1 β-$(Bi_2O_3)_{1-x}(SrO)_x$

Powder samples of eight compositions across the β-$(Bi_2O_3)_{1-x}(SrO)_x$ phase were examined at room temperature with the Philips diffractometer using the instrumental settings for precision lattice parameter determinations described in Table VII over the range $24° \leq 2\theta \leq 51°$, where the eleven most intense and well resolved diffraction peaks of the hexagonal β-phase structure occur. After removal of background and $K_{\alpha 2}$ radiation, the centroid of the $K_{\alpha 1}$ peak positions were determined with the Jade program. The d-spacing

Table X

β-$(Bi_2O_3)_{1-x}(SrO)_x$ Powder Diffraction Data

	x = 0.18		x = 0.20		x = 0.24		x = 0.28	
hk•l	d [Å]	I	d [Å]	I	d [Å]	I	d [Å]	I
10•1	3.39201	27.3	3.39268	25.6	3.39135	25.6	3.39150	22.4
01•2	3.32029	25.0	3.31988	23.1	3.31912	25.6	3.31970	27.6
00•9	3.11005	52.3	3.11101	56.4	3.10615	41.9	3.11041	60.3
10•4	3.07329	100.0	3.07427	100.0	3.07111	100.0	3.07209	100.0
01•5	2.92018	75.0	2.91981	56.4	2.91909	67.4	2.91946	67.2
10•7	2.60023	11.4	2.60116	7.7	2.59945	11.6	2.60157	12.1
01•8	2.44899	15.9	2.44895	10.3	2.44702	14.0	2.44864	10.3
10•10	2.17050	9.1	2.16853	7.7	2.16984	7.0	2.16943	6.9
01•11	2.04510	4.5	2.04442	5.1	2.04622	4.7	2.04700	6.9
11•0	1.97841	54.5	1.97957	33.3	1.97904	51.2	1.97855	43.1
10•13	1.82659	36.4						

Table X (continued)

	x = 0.32		x = 0.36		x = 0.40		x = 0.42	
hk•l	d [Å]	I	d [Å]	I	d [Å]	I	d [Å]	I
10•1	3.39429	25.0	3.39136	20.8	3.39539	10.3	3.40380	16.7
01•2	3.32185	31.9	3.32107	41.7	3.33159	55.2	3.33249	44.4
00•9	3.12500	62.5	3.13662	62.5	3.15519	55.2	3.16286	51.9
10•4	3.07673	100.0	3.07752	100.0	3.08697	100.0	3.08878	100.0
01•5	2.92400	58.3	2.92576	70.8	2.93863	79.3	2.93785	59.3
10•7	2.60709	9.7	2.61035	14.6	2.61963	6.9	2.62169	13.0
01•8	2.45391	9.7	2.45806	10.4	2.46629	6.9	2.47033	7.4
10•10	2.17703	5.6	2.18173	4.2	2.18968	3.6	2.19391	3.7
01•11	2.05193	5.6	2.05639	10.4	2.06707	3.4	2.06819	9.3
11•0	1.97883	40.3	1.97805	45.8	1.98274	37.9	1.98314	35.2
10•13	1.83305	27.8	1.83755	29.2	1.84605	24.1	1.84824	18.5

of the diffraction peaks were calculated using the currently accepted wavelength NIST wavelength of Cu $K_{\alpha 1}$, *i.e.*, λ = 1.54060 Å. The indices, d-spacings and relative intensities of these peaks are summarized in Table X.

Lattice parameters were derived from the diffraction data of Table X using the B106 refinement program and the findings are summarized in Table XI. The estimated standard deviations (esd) listed in this table are based on the differences between the observed peak positions and the positions calculated from the lattice parameter and including a refined $\cos\theta\cot\theta$ error function, which takes account of sample surface displacements.

Table XI

Lattice Parameters of β-$(Bi_2O_3)_{1-x}(SrO)_x$ at 27°C

x	*a* [Å]	esd *a* [Å]	*c* [Å]	esd *c* [Å]
0.18	3.9681	0.0018	28.132	0.013
0.20	3.9687	0.0029	28.101	0.020
0.24	3.9738	0.0021	28.154	0.015
0.28	3.9705	0.0025	28.160	0.017
0.32	3.9689	0.0015	28.269	0.010
0.36	3.9676	0.0017	28.376	0.012
0.40	3.9749	0.0040	28.517	0.028
0.42	3.9746	0.0023	28.565	0.017

4.3.2 Bismuth Yttrium Strontium Oxides

The lattice parameters of the ternary oxides Bi-Y-Sr-O are presented in Table XII, together with results for the equivalent binary oxides Bi-Sr-O.

The ternary composition $[Bi_2O_3,Y_2O_3]_{1-x}(SrO)_x$, with a constant strontium oxide composition x = 0.36, was composed of a major phase with the hexagonal β-phase structure, with Y_2O_3 and the Bi_2SrO_4 as minor phases and traces of α-Bi_2O_3 and the fcc α_1-$(Bi_2O_3)_{1-x}(Y_2O_3)_x$ phase. The increase in the *a* and *c* parameters of the ternary β-phase compared to the binary composition without yttrium, suggests that in addition to the formation of the Bi_2SrO_4 phase and the presence of unreacted Y_2 $_3$ there is a relative reduction in the amount of bismuth in the hexagonal phase. This is consistent with the Y^{3+} ion being unable to substitute for Bi^{3+} on "c" sites, consequently competing with Sr^{2+} for

occupancy of "a" sites. This solute ion redistribution takes the nominal composition out of the range of stability of the β-phase, resulting in the formation of the observed minor phases. Further annealing at 700 °C produced sharper diffraction peaks for the β-phase, but caused no significant changes in the relative intensities.

In the ternary composition $[Bi_2O_3,Y_2O_3]_{1-x}(SrO)_x$ with a constant strontium oxide composition x = 0.20, the major constituent was a hexagonal β-phase, the minor constituent was the fcc α_1-$(Bi_2O_3)_{1-x}(Y_2O_3)_x$ phase, and trace constituents included Y_2O_3 and Bi_2SrO_4. The relatively small increase in the *c* parameter compared to the binary composition without yttrium suggests that the formation of α_1-$(Bi_2O_3)_{1-x}(Y_2O_3)_x$ and the presence of unreacted Y_2O_3 results in a relatively small reduction in the amount of bismuth in the hexagonal phase, in contrast to the above results for x = 0.36. Upon further annealing the relative amount of α-Bi_2O_3 was increased and the hexagonal β-phase peaks became sharper.

In the ternary composition with a constant solvent : solute ion ratio of 0.78 (Bi^{3+}) : 0.22 (Y^{3+},Sr^{2+}) the major phase was a hexagonal β-phase, the minor phase was fcc α_1-$(Bi_2O_3)_{1-x}(Y_2O_3)_x$, and the trace phase was β-Bi_2O_3. The *a* and *c* parameters of the ternary β-phase lie between the two binaries, Bi-Sr-O and Bi-Y-O, which suggests that the hexagonal "a" sites have been substituted by both Sr^{2+} and Y^{3+} ions. Some of the yttrium ions are lost by the formation of the binary Bi-Y-O phase, thereby reducing the relative amount of yttrium in the ternary, so that the lattice parameters are closer to the x = 0.36 strontium composition than the x = 0.22 yttrium composition.

These results indicate that the hexagonal "a" sites are the only locations available to the solutes Sr^{2+} and Y^{3+} in the β-phase. It can thus be concluded that the valence of the

cation is not a factor in the designation of the solute sites and, when two cations are present a competition is established for the occupancy of these sites.

Table XII

Lattice Parameters of Bi-Y-Sr-O Samples

Constant trivalent : divalent cation ratio at 0.64 (Bi^{3+},Y^{3+}) : 0.36 (Sr^{2+})		
$(Bi_2O_3)_{0.64}(SrO)_{0.36}$	a = 3.9676	c = 28.376
$[(Bi_2O_3)_{0.496}(Y_2O_3)_{0.144}](SrO)_{0.36}$	a = 3.9688	c = 28.523
Constant trivalent : divalent cation ratio at 0.80 (Bi^{3+},Y^{3+}) : 0.20 (Sr^{2+})		
$(Bi_2O_3)_{0.8}(SrO)_{0.2}$	a = 3.9687	c = 28.101
$[(Bi_2O_3)_{0.62}(Y_2O_3)_{0.18}](SrO)_{0.2}$	a = 3.9604	c = 28.250

Constant solvent : solute ratio at 0.78 (Bi^{3+}) : 0.22 (Y^{3+},Sr^{2+})		
$(Bi_2O_3)_{0.64}(SrO)_{0.36}$	a = 3.9676	c = 28.376
$(Bi_2O_3)_{0.703}[(Y_2O_3)_{0.099}(SrO)_{0.198}]$	a = 3.9622	c = 28.225
$(Bi_2O_3)_{0.78}(Y_2O_3)_{0.22}$	a = 3.9485	c = 27.275
$(Bi_2O_3)_{0.78}(Y_2O_3)_{0.22}$	a = 5.4337 Å (fcc above 720 °C)	

4.4 High Temperature Lattice Parameters

Powder samples of the eight β-$(Bi_2O_3)_{1-x}(SrO)_x$ samples were examined at temperatures up to 777 °C with the Scintag high temperature diffractometer using the instrumental settings for precision lattice parameter determinations described in Table VIII over the range $15° \leq 2\theta \leq 55°$, which included fifteen to sixteen well resolved diffraction peaks of the hexagonal β-phase structure. After removal of background and $K_{\alpha 2}$ radiation, the d-spacings of the $K_{\alpha 1}$ peak positions were determined by the Scintag profile fitting

routine based on a Pearson VII function and indices were assigned by reference to the previous room temperature results. Lattice parameters determined from these d-spacings by the B106 refinement program are summarized in Tables XIII - XX. In order to identify any irreversible effects during thermal cycling, the lattice parameters were determined at temperatures in the experimental sequence indicated in the final column of each table.

Table XIII

High Temperature Lattice Parameters for x = 0.18

Temperature [°C]	Temperature [K]	*a* [Å]	esd *a* [Å]	*c* [Å]	esd *c* [Å]	Sequence
27	300	3.9702	0.0015	28.140	0.015	1
127	400	3.9764	0.0013	28.160	0.013	2
227	500	3.9819	0.0015	28.193	0.011	3
327	600	3.9886	0.0018	28.225	0.012	4
427	700	3.9957	0.0031	28.258	0.022	5
527	800	4.0018	0.0020	28.309	0.014	6
602	875	4.0099	0.0029	28.371	0.021	11
627	900	4.0073	0.0014	28.372	0.010	7
652	925	4.0104	0.0021	28.401	0.015	10
677	950	4.0167	0.0033	28.612	0.023	8
702	975	4.0175	0.0025	28.630	0.018	9

Table XIV

High Temperature Lattice Parameters for x = 0.20

Temperature [°C]	Temperature [K]	*a* [Å]	esd *a* [Å]	*c* [Å]	esd *c* [Å]	Sequence
27	300	3.9637	0.0062	28.114	0.044	1
27	300	3.9661	0.0021	28.096	0.022	17
127	400	3.9669	0.0058	28.131	0.041	2
227	500	3.9729	0.0067	28.191	0.047	3
227	500	3.9771	0.0045	28.144	0.032	10
327	600	3.9780	0.0059	28.209	0.042	4
377	650	3.9888	0.0082	28.228	0.058	11
427	700	3.9842	0.0072	28.253	0.051	5
427	700	3.9887	0.0025	28.226	0.017	18
477	750	3.9955	0.0077	28.275	0.055	12
527	800	3.9915	0.0073	28.261	0.052	6
527	800	3.9951	0.0034	28.277	0.024	19
577	850	3.9974	0.0052	28.348	0.037	13
627	900	3.9996	0.0061	28.344	0.043	7
627	900	4.0043	0.0038	28.382	0.027	20
652	925	4.0046	0.0089	28.412	0.063	15
677	950	4.0068	0.0030	28.413	0.021	21
702	975	4.0182	0.0020	28.623	0.014	22
702	975	4.0149	0.0040	28.626	0.028	16
727	1000	4.0186	0.0037	28.634	0.027	8
752	1025	4.0152	0.0047	28.633	0.034	23
777	1050	4.0225	0.0082	28.708	0.059	9

Table XV

High Temperature Lattice Parameters for x = 0.24

Temperature [°C]	Temperature [K]	*a* [Å]	esd *a* [Å]	*c* [Å]	esd *c* [Å]	Sequence
27	300	3.9682	0.0018	28.092	0.013	1
127	400	3.9721	0.0023	28.130	0.016	2
227	500	3.9778	0.0030	28.179	0.021	3
327	600	3.9846	0.0030	28.230	0.021	4
427	700	3.9908	0.0030	28.271	0.021	5
477	750	3.9962	0.0028	28.321	0.020	15
527	800	3.9933	0.0025	28.319	0.018	6
577	850	4.0000	0.0048	28.373	0.034	14
602	875	4.0005	0.0027	28.394	0.019	13
627	900	3.9980	0.0028	28.415	0.020	7
652	925	4.0022	0.0024	28.425	0.017	12
677	950	4.0058	0.0032	28.441	0.023	11
702	975	4.0048	0.0055	28.421	0.039	10
727	1000	4.0152	0.0030	28.648	0.021	8
752	1025	4.0193	0.0028	28.673	0.020	9

Table XVI

High Temperature Lattice Parameters for x = 0.28

Temperature [°C]	Temperature [K]	*a* [Å]	esd *a* [Å]	*c* [Å]	esd *c* [Å]	Sequence
27	300	3.969	0.0041	28.150	0.029	1
127	400	3.975	0.0031	28.209	0.022	2
227	500	3.978	0.0058	28.231	0.041	3
327	600	3.983	0.0026	28.283	0.018	4
427	700	3.992	0.0022	28.354	0.016	5
527	800	3.996	0.0033	28.411	0.023	6
627	900	4.002	0.0030	28.476	0.021	7
652	925	4.001	0.0040	28.490	0.028	11
677	950	4.005	0.0030	28.528	0.022	8
702	975	4.004	0.0025	28.533	0.018	9
727	1000	4.018	0.0035	28.706	0.025	10
752	1025	4.019	0.0050	28.704	0.036	12

Table XVII

High Temperature Lattice Parameters for x = 0.32

Temperature [°C]	Temperature [K]	*a* [Å]	esd *a* [Å]	*c* [Å]	esd *c* [Å]	Sequence
27	300	3.9640	0.0013	28.254	0.009	1
177	450	3.9729	0.0044	28.311	0.031	16
277	550	3.9761	0.0026	28.341	0.018	14
377	650	3.9804	0.0028	28.392	0.020	13
477	750	3.9881	0.0038	28.470	0.027	12
527	800	3.9923	0.0026	28.525	0.018	2
577	850	3.9953	0.0035	28.529	0.025	11
602	875	3.9969	0.0023	28.545	0.016	10
627	900	3.9999	0.0027	28.596	0.020	3
652	925	4.0001	0.0032	28.592	0.023	9
677	950	4.0016	0.0045	28.617	0.032	4
690	963	4.0136	0.0040	28.775	0.029	15
702	975	4.0161	0.0038	28.767	0.027	8
727	1000	4.0157	0.0030	28.787	0.022	5
752	1025	4.0171	0.0027	28.800	0.019	6
777	1050	4.0200	0.0034	28.804	0.024	7

Table XVIII

High Temperature Lattice Parameters for x = 0.36

Temperature [°C]	Temperature [K]	*a* [Å]	esd *a* [Å]	*c* [Å]	esd *c* [Å]	Sequence
127	400	3.9731	0.0054	28.419	0.038	2
227	500	3.9745	0.0053	28.484	0.038	3
227	500	3.9770	0.0019	28.474	0.013	7
327	600	3.9816	0.0022	28.516	0.016	4
427	700	3.9865	0.0021	28.579	0.015	5
527	800	3.9923	0.0022	28.646	0.016	6
577	850	3.9982	0.0012	28.715	0.008	15
627	900	4.0013	0.0018	28.763	0.013	11
627	900	4.0025	0.0019	28.768	0.014	16
652	925	4.0081	0.0019	28.822	0.013	22
677	950	4.0082	0.0024	28.836	0.017	12
677	950	4.0110	0.0032	28.845	0.023	17
702	975	4.0144	0.0016	28.876	0.011	21
727	1000	4.0150	0.0023	28.890	0.016	13
727	1000	4.0159	0.0020	28.885	0.014	18
752	1025	4.0177	0.0022	28.923	0.016	20
777	1050	4.0214	0.0022	28.938	0.016	19

Table XIX

High Temperature Lattice Parameters for x = 0.40

Temperature [°C]	Temperature [K]	*a* [Å]	esd *a* [Å]	*c* [Å]	esd *c* [Å]	Sequence
27	300	3.9693	0.0035	28.538	0.025	1
127	400	3.9760	0.0043	28.573	0.031	2
227	500	3.9781	0.0029	28.619	0.021	3
327	600	3.9816	0.0035	28.669	0.003	4
427	700	3.9889	0.0046	28.709	0.033	5
527	800	3.9934	0.0038	28.766	0.027	6
552	825	3.9963	0.0035	28.779	0.025	15
602	875	4.0009	0.0028	28.843	0.020	14
627	900	4.0023	0.0043	28.880	0.031	7
652	925	4.0092	0.0049	28.915	0.036	13
677	950	4.0072	0.0032	28.932	0.023	12
702	975	4.0093	0.0022	28.957	0.016	11
727	1000	4.0089	0.0028	28.994	0.021	8
752	1025	4.0133	0.0018	28.998	0.013	10
777	1050	4.0180	0.0043	29.028	0.031	9

Table XX

High Temperature Lattice Parameters for x = 0.42

Temperature [°C]	Temperature [K]	*a* [Å]	esd *a* [Å]	*c* [Å]	esd *c* [Å]	Sequence
26	299	3.9746	0.0035	28.565	0.025	17
27	300	3.9788	0.0026	28.595	0.027	1
127	400	3.9756	0.0039	28.606	0.028	2
202	475	3.9808	0.0015	28.694	0.011	12
227	500	3.9774	0.0063	28.619	0.045	3
252	550	3.9795	0.0039	28.669	0.028	11
302	575	3.9850	0.0017	28.746	0.012	13
327	600	3.9824	0 0055	28.678	0.039	4
427	700	3.9931	0.0031	28.794	0.022	5
527	800	3.9985	0.0017	28.871	0.012	6
552	825	4.0010	0 0030	28.881	0.021	7
602	875	4.0038	0.0017	28.936	0.012	8
627	900	4.0079	0.0019	28.954	0.013	14
652	925	4.0084	0.0024	29.015	0.017	9
702	975	4.0133	0.0020	29.040	0.014	10
727	1000	4.0154	0.0024	29.052	0.018	15
752	1025	4.0221	0.0028	29.101	0.020	16

4.5 Low Temperature Lattice Parameters

Powder samples of the eight β-$(Bi_2O_3)_{1-x}(SrO)_x$ samples were examined at temperatures down to 77 K with the low temperature attachment on the Scintag diffractometer using the instrumental settings for precision lattice parameter determinations described in Table VIII over the range $23° \leq 2\theta \leq 61°$, which include fifteen to seventeen well resolved diffraction peaks of the hexagonal β-phase structure. After removal of background and $K_{\alpha 2}$ radiation, the d-spacings of the $K_{\alpha 1}$ peak positions were determined by the Scintag profile fitting routine based on a Pearson VII function and indices were assigned by reference to the previous room temperature results. Lattice parameters determined from these d-spacings by the B106 refinement program are summarized in Tables XXI - XXVIII.

Table XXI

Low Temperature Lattice Parameters for x = 0.18

Temperature [K]	*a* [Å]	esd *a* [Å]	*c* [Å]	esd *c* [Å]
100	3.9605	0.0017	28.065	0.0121
150	3.9658	0.0031	28.096	0.0221
200	3.9669	0.0028	28.114	0.0192
250	3.9674	0.0016	28.129	0.0110
299	3.9685	0.0026	28.145	0.0188
350	3.9752	0.0027	28.174	0.0193

Table XXII

Low Temperature Lattice Parameters for x = 0.20

Temperature [K]	*a* [Å]	esd *a* [Å]	*c* [Å]	esd *c* [Å]
100	3.9629	0.0026	28.061	0.0183
150	3.9636	0.0019	28.079	0.0131
200	3.9656	0.0020	28.101	0.0141
250	3.9704	0.0031	28.119	0.0221
300	3.9696	0.0021	28.125	0.015
350	3.9728	0.0019	28.123	0.0133

Table XXIII

Low Temperature Lattice Parameters for x = 0.24

Temperature [K]	*a* [Å]	esd *a* [Å]	*c* [Å]	esd *c* [Å]
100	3.9642	0.0028	28.058	0.020
150	3.9652	0.0012	28.074	0.009
200	3.9639	0.0034	28.072	0.024
250	3.9681	0.0020	28.087	0.014
298	3.9722	0.0016	28.116	0.012
350	3.9741	0.0030	28.136	0.021

Table XXIV

Low Temperature Lattice Parameters for x = 0.28

Temperature [K]	*a* [Å]	esd *a* [Å]	*c* [Å]	esd *c* [Å]
77	3.961	0.0025	28.077	0.0176
100	3.9605	0.0019	28.087	0.0134
200	3.9643	0.0021	28.109	0.0152
294	3.9679	0.0023	28.135	0.0165

Table XXV

Low Temperature Lattice Parameters for x = 0.32

Temperature [K]	*a* [Å]	esd *a* [Å]	*c* [Å]	esd *c* [Å]
77	3.9587	0.0013	28.193	0.009
100	3.9597	0.0019	28.201	0.013
200	3.9643	0.0019	28.234	0.014
300	3.9689	0.0026	28.274	0.018

Table XXVI

Low Temperature Lattice Parameters for x = 0.36

Temperature [K]	*a* [Å]	esd *a* [Å]	*c* [Å]	esd *c* [Å]
100	3.9563	0.0018	28.282	0.013
200	3.9607	0.0017	28.312	0.012
297	3.9655	0.0013	28.344	0.009
350	3.9658	0.0013	28.364	0.010

Table XXVII

Low Temperature Lattice Parameters for x = 0.40

Temperature [K]	*a* [Å]	esd *a* [Å]	*c* [Å]	esd *c* [Å]
100	3.9647	0.0033	28.429	0.024
200	3.9699	0.0025	28.498	0.018
250	3.9718	0.0041	28.468	0.029
294	3.9734	0.0048	28.497	0.034
300	3.9750	0.0010	28.523	0.007
350	3.9752	0.0040	28.528	0.029

Table XXVIII

Low Temperature Lattice Parameters for x = 0.42

Temperature [K]	*a* [Å]	esd *a* [Å]	*c* [Å]	esd *c* [Å]
100	3.9689	0.0023	28.495	0.016
150	3.9679	0.0030	28.499	0.022
200	3.9710	0.0019	28.558	0.013
250	3.9734	0.0024	28.560	0.017
300	3.9791	0.0019	28.600	0.014
350	3.9777	0.0026	28.600	0.019

CHAPTER 5 - Discussion

5.1 Crystal Structure Results

In Table XXIX, the experimentally determined X-ray diffraction patterns presented previously in Figures 4.2a and 4.2b are compared to simulated patterns calculated by the MDI program µ-POWD using the space group symmetry and atomic positions given by: 1) Sillén and Aurivillius (S&A) [3], 2) Conflant, Boivin and Thomas (CBT) [5], and 3) Blower and Greaves (B&G) [7]. In each of the computed models the lattice parameters have been set to the experimental result for the composition x = 0.28, *i.e.*, a_H = 3.9690 Å and c_H = 28.150 Å for the hexagonal unit cell, or equivalently, a_M = 13.749 Å, b_M = 7.938 Å, c_M = 9.659 Å, β = 103.72° for the monoclinic unit cell.

Table XXIX

Comparison of Simulated Diffraction Patterns With Observed Results for x = 0.28

d-spacing	hk•l	I (S&A)	I (CBT)	hkl	I (B&G)	I obs
9.383	00•3	1	1	0 0 1	1	0
6.678	-		-	2 0 0	0	-
4.692	00•6	5	5	0 0 2	5	2
3.412	10•1	24	32	2 2 0, -4 0 1	24	28
3.339	01•2	39	39	4 0 0, -2 2 1	33	29
3.128	00•9	54	50	0 0 3	50	57
3.089	10•4	100	100	2 2 1, -4 0 2	100	100
2.934	01•5	74	58	4 0 1, -2 2 2	55	65
2.613	10•7	8	12	2 2 2, -4 0 3,	10	12
2.605				2 0 3		

d-spacing	hk•l	I (S&A)	I (CBT)	hkl	I (B&G)	I obs
2.587	-	-	-	-4 2 1	1	-
2.459	01•8	21	14	4 0 2, -2 2 3	14	13
2.359	-	-	-	4 2 1	0	-
2.226	-	-	-	6 0 0	0	-
2.178	10•10	4	9	2 2 3, -4 0 4	5	9
2.090	-		-	4 2 2	0	0
2.053	01•11	16	8	4 0 3, -2 2 4	8	7
1.9845	11•0	52	49	0 4 0, -6 2 1	44	39
1.9416	11•3	0	0	-6 2 2	1	1
1.8767	00•15	1	1	0 0 5	1	1
1.8321	10•13	30	25	2 2 4, -4 0 5	27	26
1.7356	01•14	12	14	4 0 4, -2 2 5	11	13
1.7154	02•1	4	4	-8 0 1, -4 4 1	4	3
1.7060	20•2	6	6	4 4 0, -8 0 2	5	6
1.6757	11•9	47	45	6 2 2, 0 4 3,	42	45
1.6756				-6 2 4		
1.6696	02•4	19	18	8 0 0, -4 4 2	18	24
1.6437	20•5	12	10	4 4 1, -8 0 3	10	12
1.5804	02•7	2	3	8 0 1, -4 4 3	2	2
1.5747	-	-	-	-8 2 1	1	-
1.5661	10•16	5	6	2 2 5, -4 0 6,	5	9
1.5639	00•18			0 0 6		
1.5443	20•8	5	3	4 4 2, -8 0 4	3	2
1.4918	01•17	7		4 0 5, -2 2 6	5	4
1.4669	02•10	1		-4 4 4	1	2
1.4267	20•11	4		4 4 3, -8 0 5	2	2
1.3635	11•15	2		6 2 4, 0 4 5,	2	1
				-6 2 6		
1.3462	02•13	9		8 0 3, -4 4 5	7	7
1.3064	20•14	4		4 4 4, -8 0 6	3	4
1.3025	01•20	2		4 0 6, -2 2 7	3	3
1.2978	21•1	3		-8 4 1, 2 6 0,	3	3
				-10 2 2		

d-spacing	hk•l	I (S&A)	I (CBT)	hkl	I (B&G)	I obs
1.2937	12•2	4		-10 2 1, -2 6 1, -8 4 2	3	0
1.2776	21•4	12		8 4 0, 2 6 1, -10 2 3	9	1
1.2659	12•5	9		10 2 0, -2 6 2, -8 4 3	7	6
1.2362	21•7	2		8 4 1, 2 6 2, -10 2 4	2	0
1.2294	02•6			-4 4 6, 6 2 5,		
1.2283	11•18	11		0 4 6, -6 2 7	9	10
1.2187	12•8	4		10 2 1, -2 6 3, -8 4 4	3	1
1.1992	10•22	7		2 2 7, -4 0 8	5	5
1.1925	20•17	3		4 4 5, -8 0 7	2	1

According to the monoclinic structural model of Blower and Greaves [7], the strongest perlattice line (arising from anion diffraction) occurs at an angle of 13.5° 2θ (for Cu K_α radiation), with a relative X-ray diffraction intensity of only 0.05 %, as shown in Figure 5.1, which is below the limit of resolution of the X-ray diffraction technique, but has been clearly resolved by neutron diffraction [7] for which the relative intensity is much greater. The close similarity of the fundamental lines of the simulated hexagonal and monoclinic diffraction patterns and the observed diffraction pattern is shown in Figure 5.2 for the angular range for the high angle region from 71 - 117 °2θ. This agreement stems from the identical cation sublattices of the hexagonal and monoclinic unit cells, as illustrated in Figure 5.3. When using X-ray and electron diffraction data, the monoclinic structure can properly be represented as pseudo-hexagonal with respect to the cation sublattice.

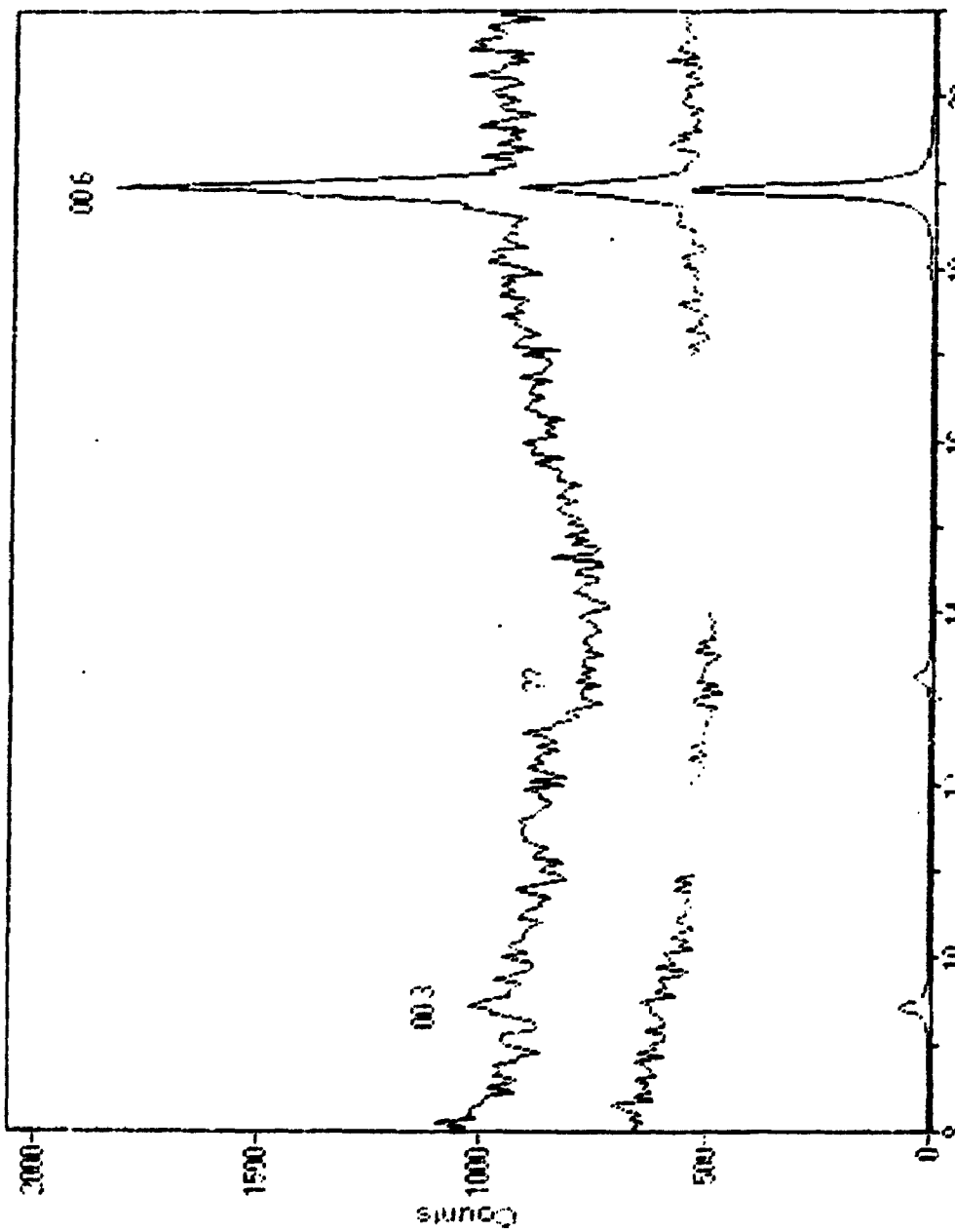

Figure 5.1 Observed diffraction patterns (top) of β-(Bi2O3)0.72(SrO)0.28 recorded over the range 8° - 21° and (bottom) a simulated pattern based on the crystal structure model of Blower and Greaves including the strongest superlattice peak labelled "??"

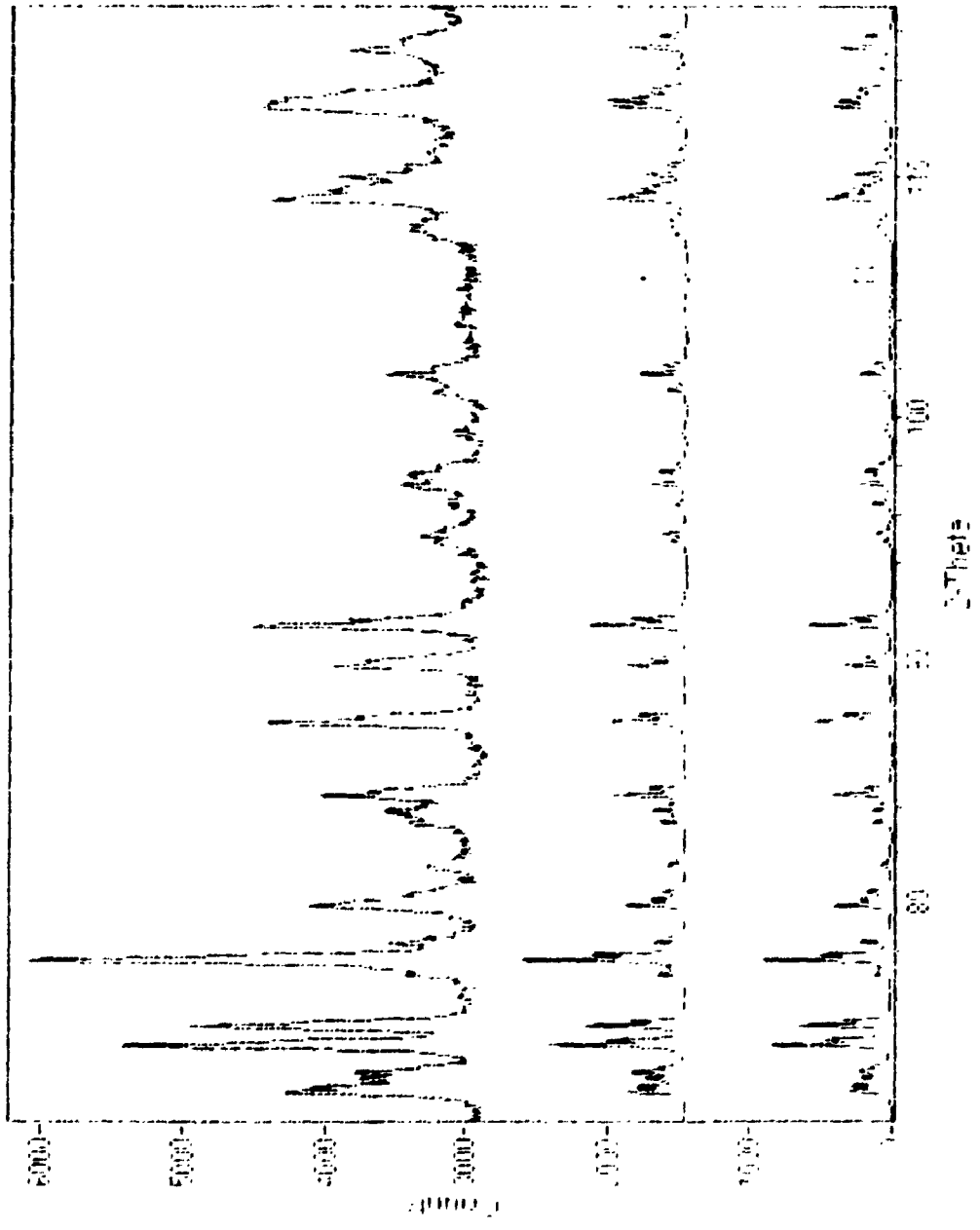

Figure 5.2 The observed diffraction pattern of β-(Bi2O3)0.72(SrO)0.28 over the range 71° - 117° and simulated patterns based on the crystal structure models of Conflant et al. and Blower and Greaves

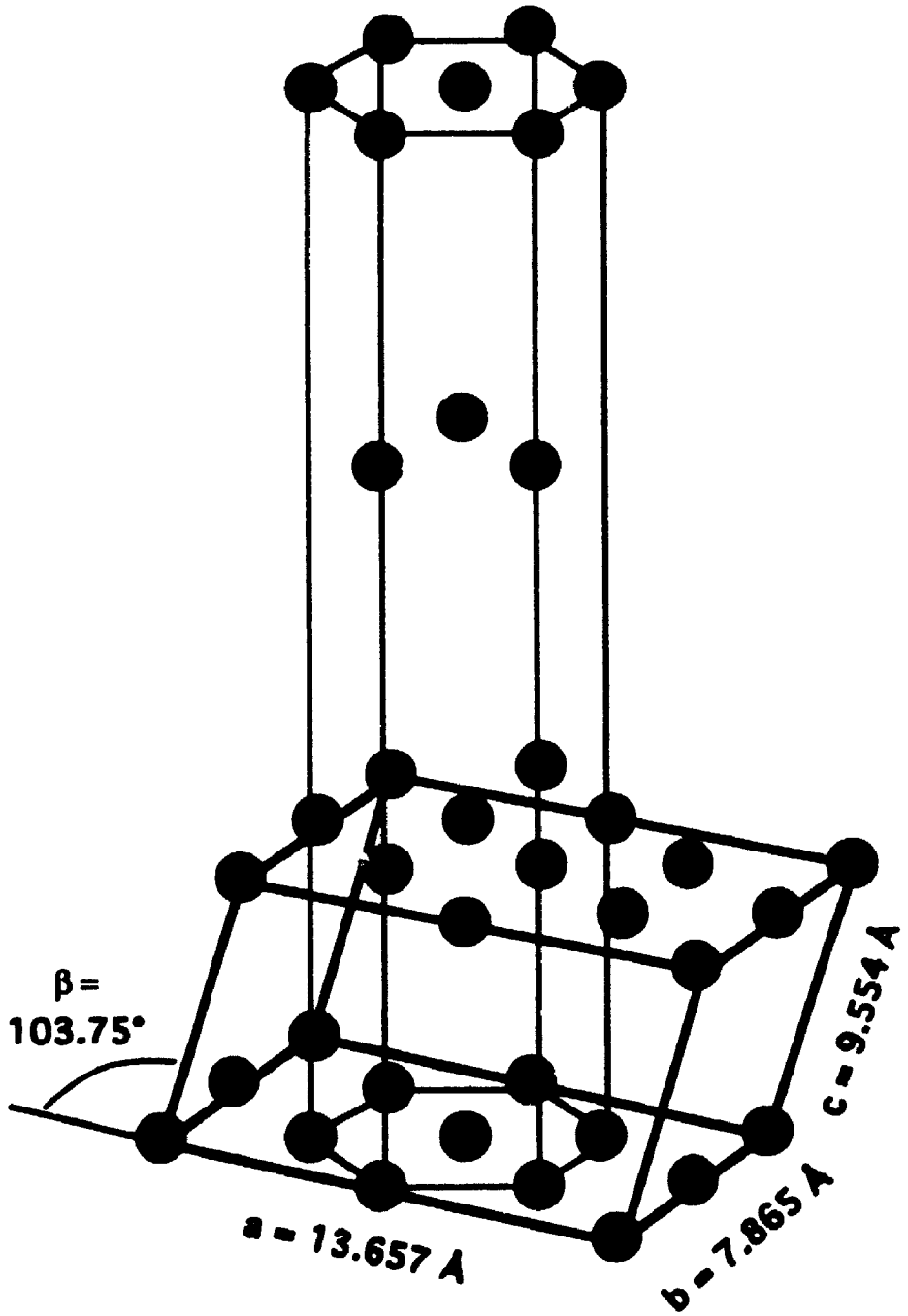

Figure 5.3 Relationship between monoclinic and hexagonal unit cells illustrating the equivalence of the substituted cation sublattice

5.2 Composition Dependence of Lattice Parameters

The refined room temperature lattice parameters derived from the data presented in Table XI are plotted in Figure 5.4. The error bars in the figure represent the estimated standard deviations of the lattice parameters. In Figure 5.5 these lattice parameters are superimposed on all the lattice parameter determinations from the literature review. The present data make sense of the apparent experimental scatter of previously published data. The *a* parameters conform to an approximately linear plot with a very shallow slope in agreement with the previously published results. This is consistent with the layered nature of the cation structure in which the strontium solute ions are only located in a single layer, so that the bismuth ions in the two unsubstituted layers have the dominant effect on the *a* parameter which remains effectively unchanged.

The original *c* parameters reported by Sillén and Aurivillius [3,4] lie on a nearly straight line, but only incorporate data from the strontium-rich side of the solid solution. Guillermo *et al.* [10] examined a wider range and noted that the parameters remained constant at first, and then increased slightly with increased strontium content, but this observation was based on only three data points. Guillermo interpreted this finding to indicate that the substitution of bismuth by a larger ion (Sr) had a greater effect on the *c* parameter than the concurrent increase in the number of oxygen vacancies. The strontium substitution results in an increase in the *c* parameter due to the separation of the cation layers, even though it does not increase the *a* parameter which is related to the interionic distances within the layers.

The greater number of samples examined in the present work also reveals that the composition dependence of the *c* parameter has a shallow slope at values $x \leq 0.28$ and a steeper slope for compositions $x \geq 0.28$. This observed change in the slope of the *c*

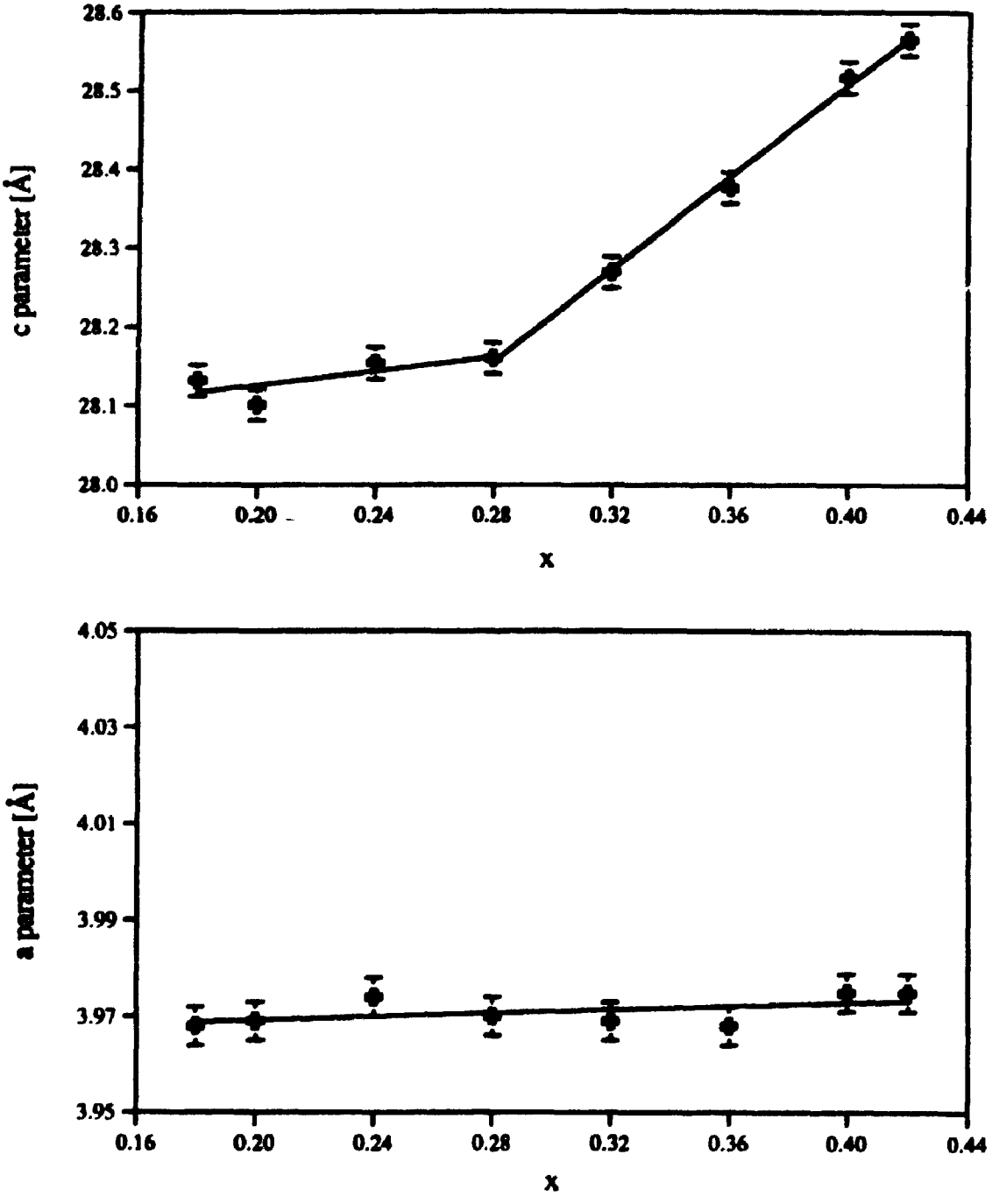

Figure 5.4 Graph of the composition dependence of lattice parameters of β-$(Bi_2O_3)_{1-x}(SrO)_x$ with separate lines fit to the ranges $0.18 \leq x \leq 0.28$ and $0.28 \leq x \leq 0.42$

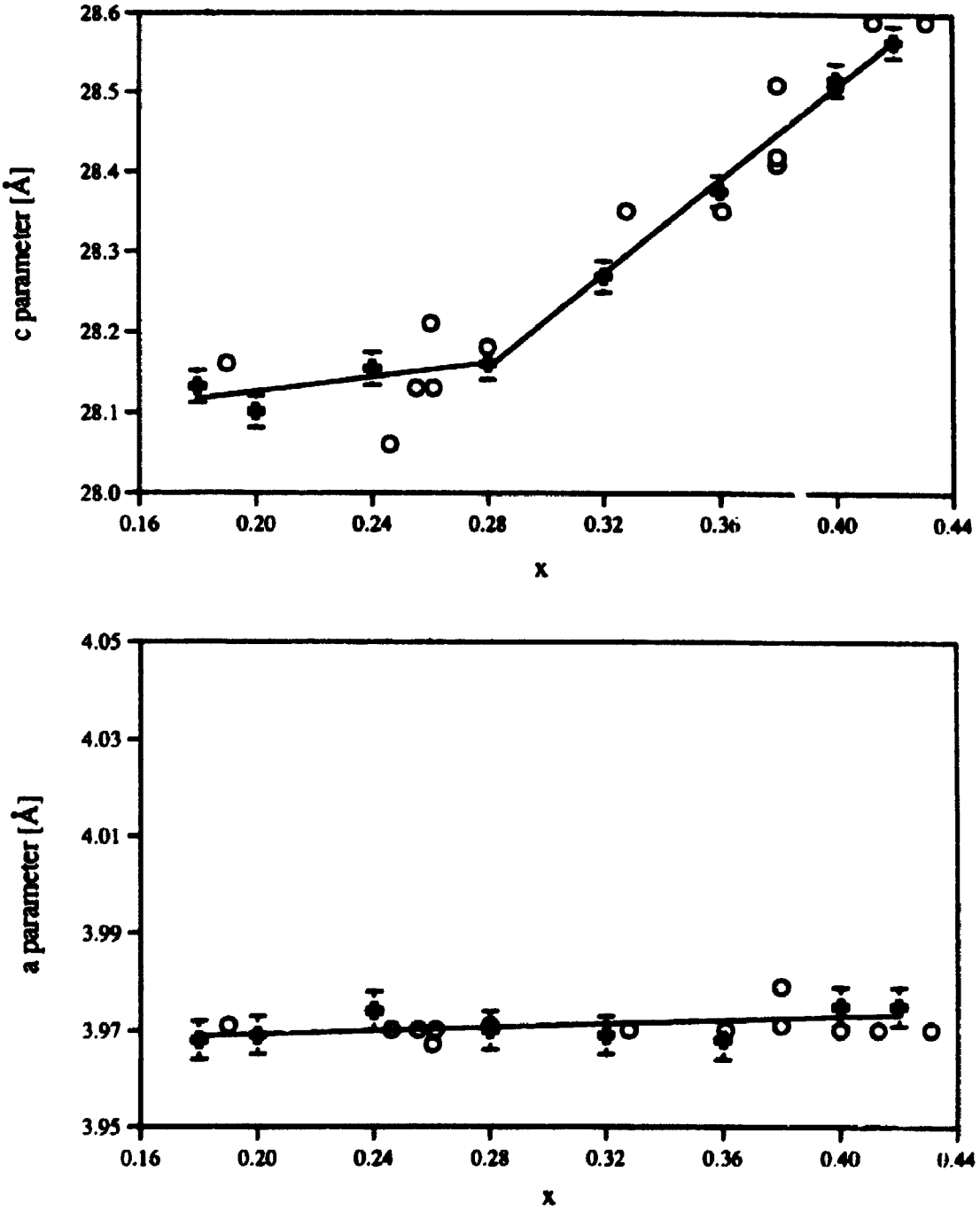

Figure 5.5 Superposition of the observed a and c lattice parameters at room temperature with values reported in the literature

parameter may be related to the fact that at $x \leq 0.28$ the number of bismuth cations is greater than the number of strontium cations at the hexagonal "a" sites, whereas at compositions $x \geq 0.28$ the number of strontium ions is greater than the number of bismuth ions. At $x \geq 0.28$, the *c* parameter may become even greater because the majority Sr^{2+} ions in the "a" sites are more weakly bound to the oxygen anions in the octahedron which surround them (see Figure 2.5). The expansion of the octahedron is constrained in the plane normal to the z-axis by the undisturbed bonding of Bi-O in the unsubstituted bismuth layers, so that the distortion will be directed along the z-axis, resulting in an expansion of the *c* parameter.

5.3 Temperature Dependence of Lattice Parameters

The low temperature lattice parameter results at 100, 200, and 300 K, for all β-phase compositions are shown in Figure 5.6. The *a* parameters conform to approximately linear plots with relatively shallow slopes, in agreement with the room temperature results presented previously in Figure 5.5. For the compositions $x \leq 0.28$ the *c* parameters are again characterized by a relatively shallow slope, whereas for $x \geq 0.28$ the *c* parameters have a steeper slope, in agreement with the room temperature results described previously. The extension of the trends observed at room temperature to temperatures down to 100 K confirms the low temperature stability of the β-phase and thus provides a benchmark for defining any anomalies which may occur at higher temperatures.

The *a* and *c* hexagonal lattice parameters determined over the entire experimental range of temperatures from 77 - 1050 K for each of the compositions are shown in Figures 5.7 - 5.14. These plots indicate two distinct composition-dependent trends. For all compositions $x \leq 0.36$, both the *a* and *c* parameters show a continuous expansion with

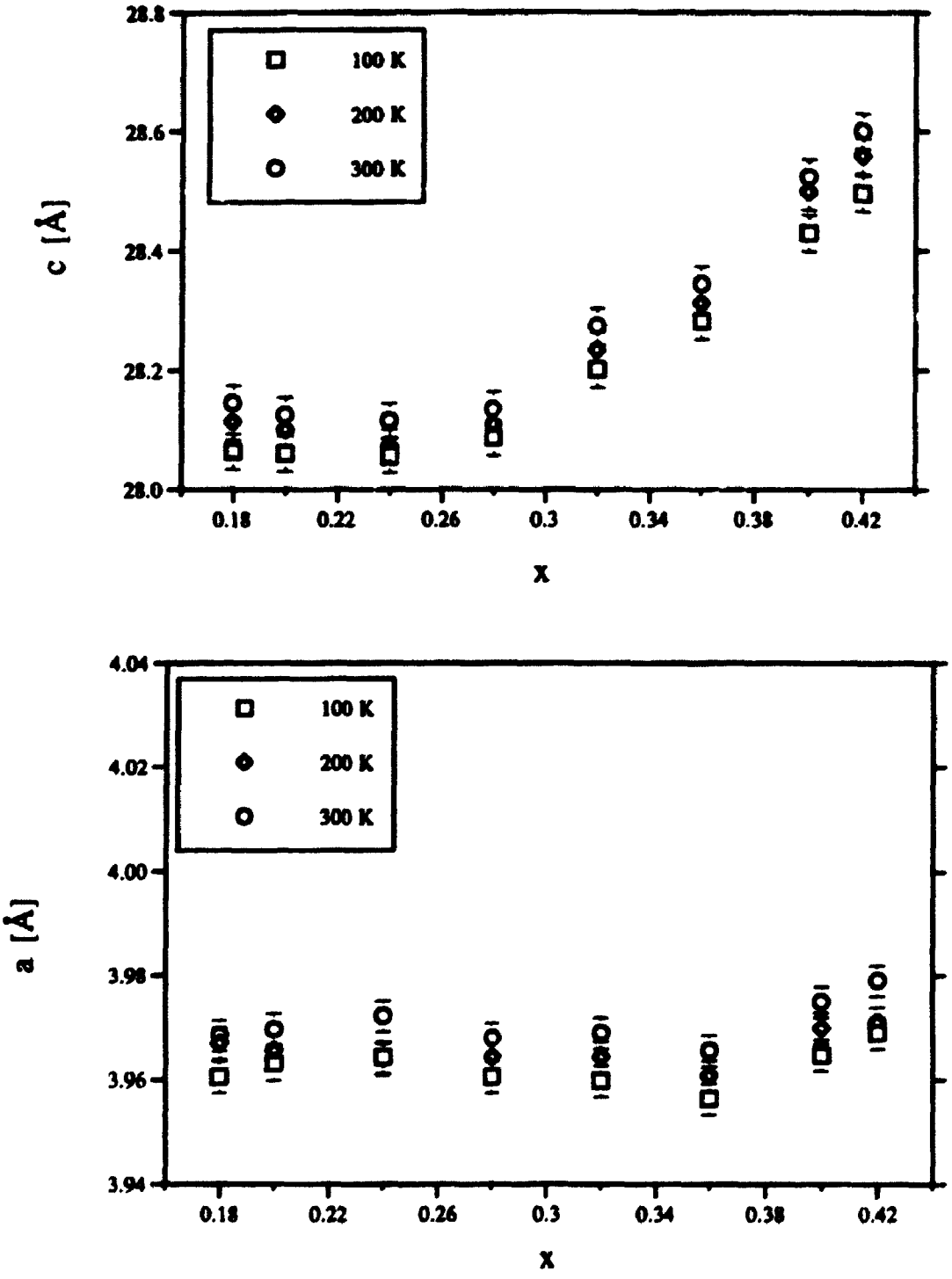

Figure 5.6 Composition dependence of the low temperature a and c lattice parameters of $(Bi_2O_3)_{1-x}(SrO)_x$

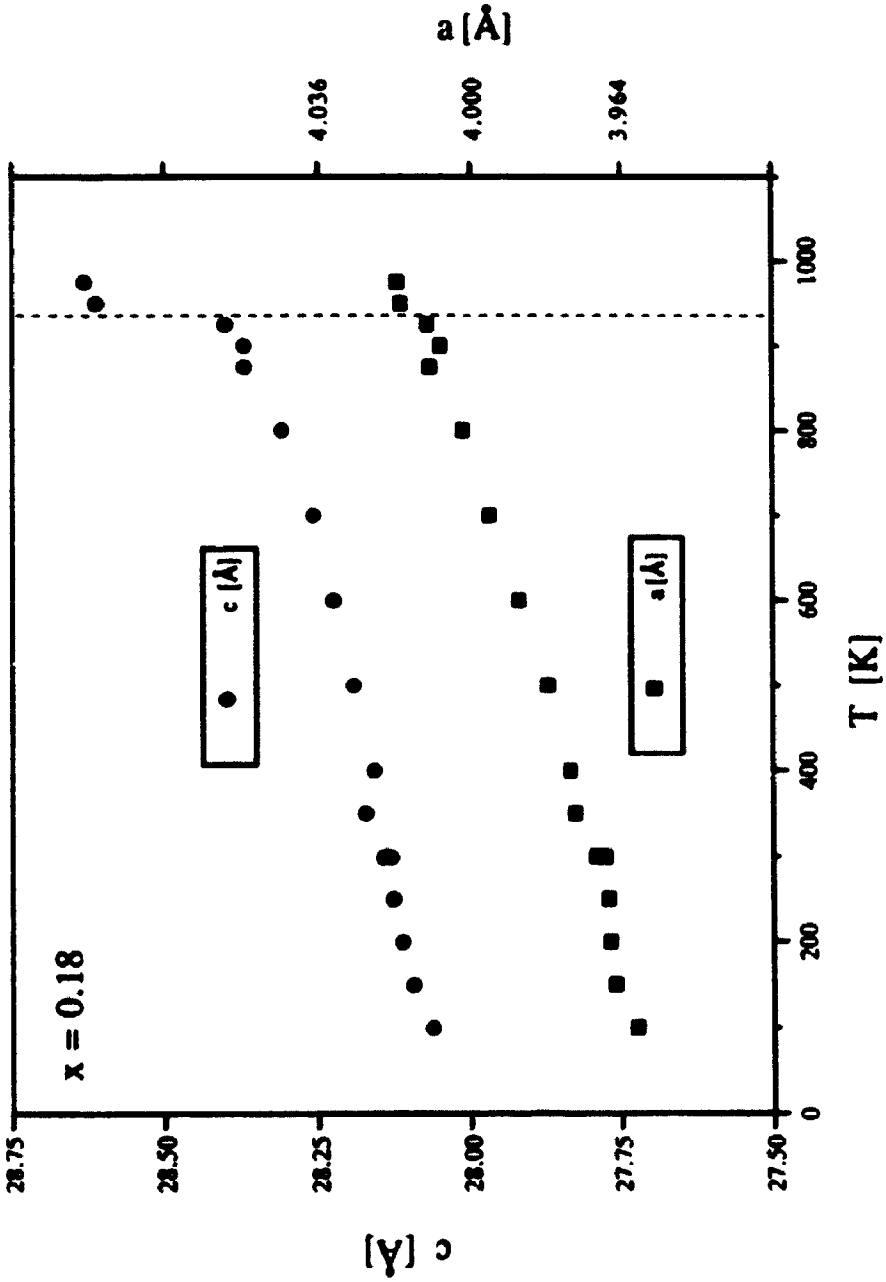

Figure 5.7 Temperature dependence of the a and c lattice parameters of β-$(Bi_2O_3)_{0.82}(SrO)_{0.18}$

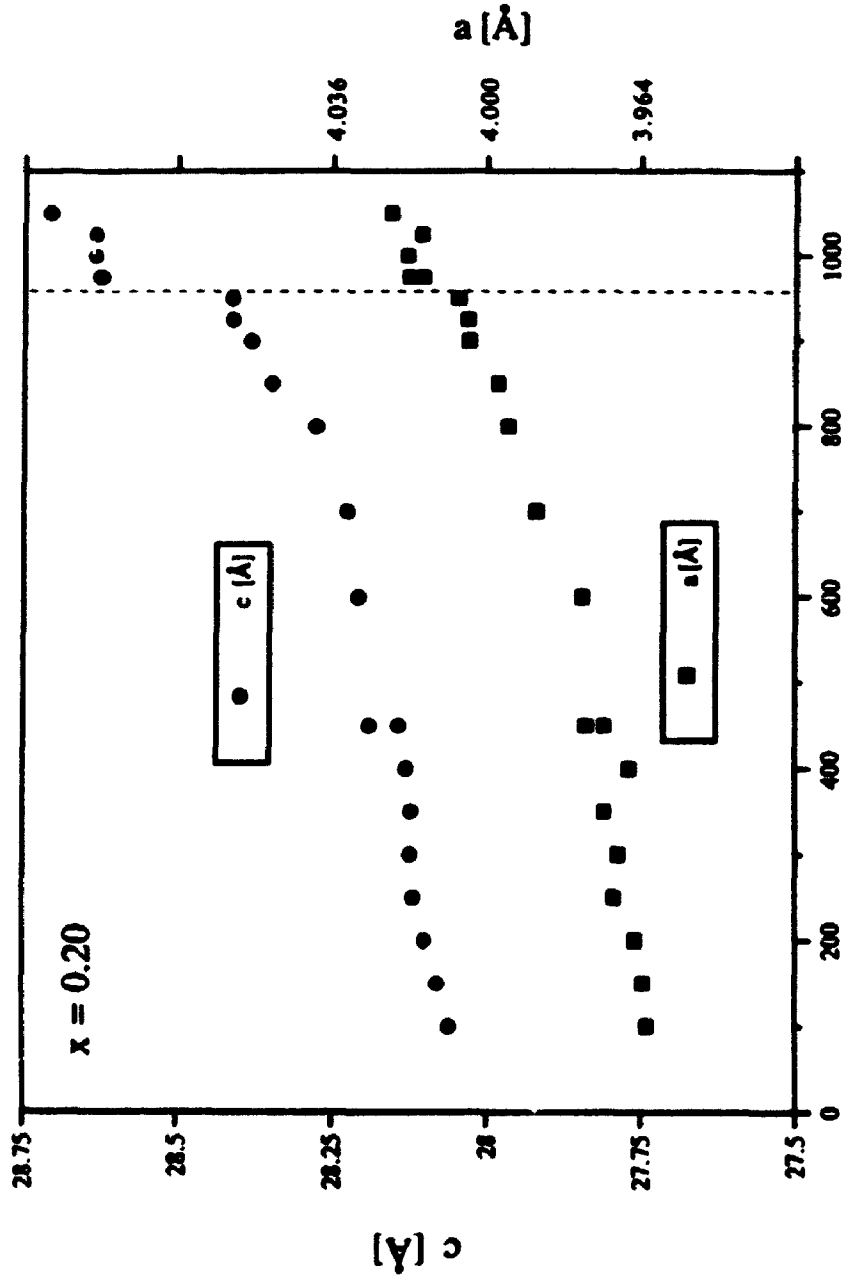

Figure 5.8 Temperature dependence of the a and c lattice parameters of β-$(Bi_2O_3)_{0.80}(SrO)_{0.20}$

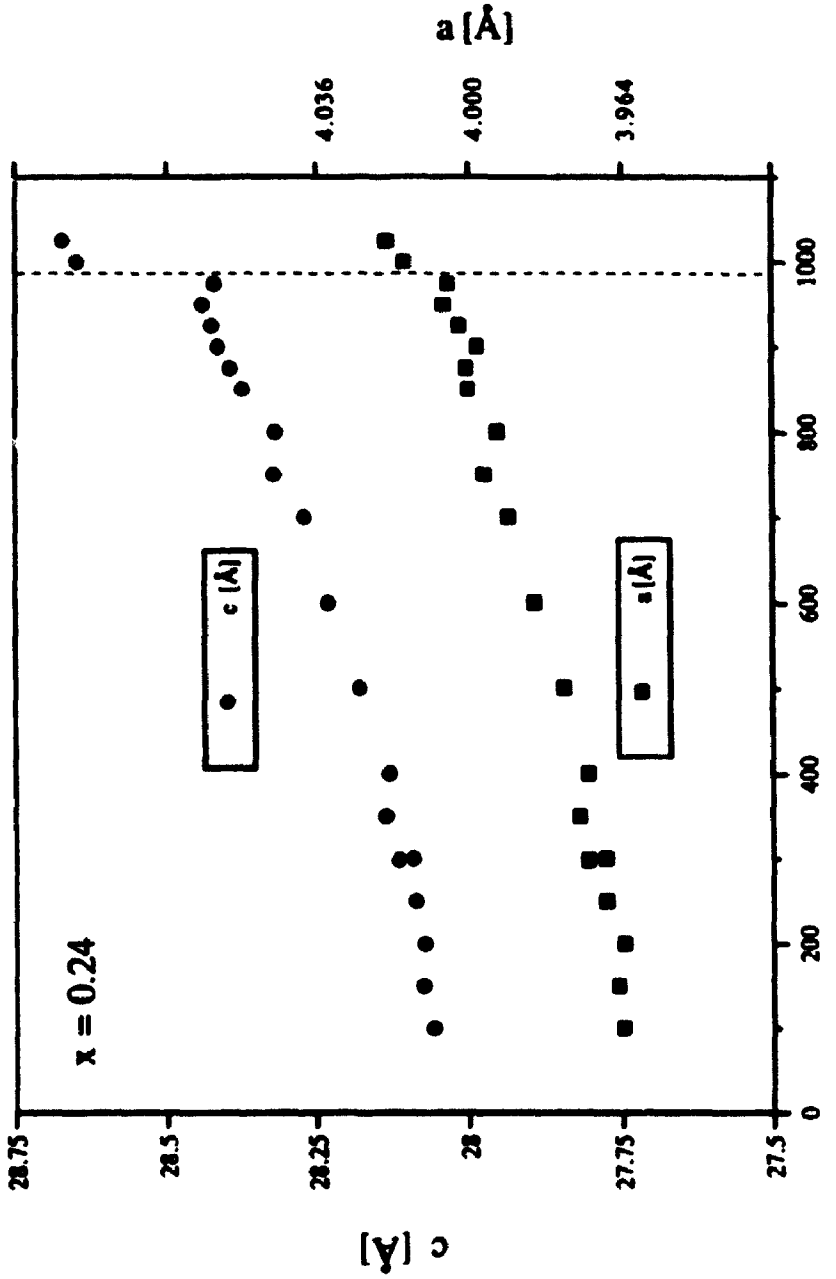

Figure 5.9 Temperature dependence of the a and c lattice parameters of β-$(Bi_2O_3)_{0.76}(SrO)_{0.24}$

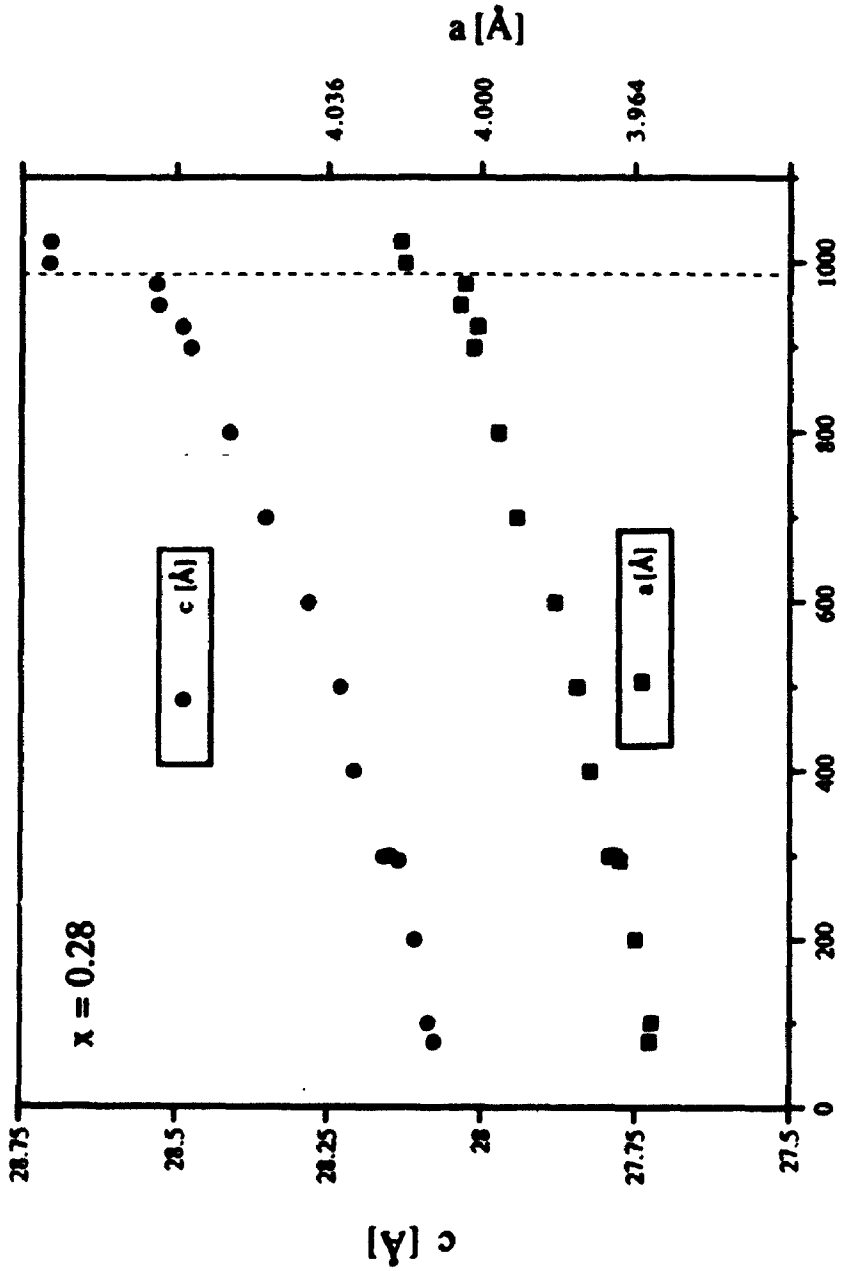

Figure 5.10 Temperature dependence of the a and c lattice parameters of β-$(Bi_2O_3)_{0.72}(SrO)_{0.28}$

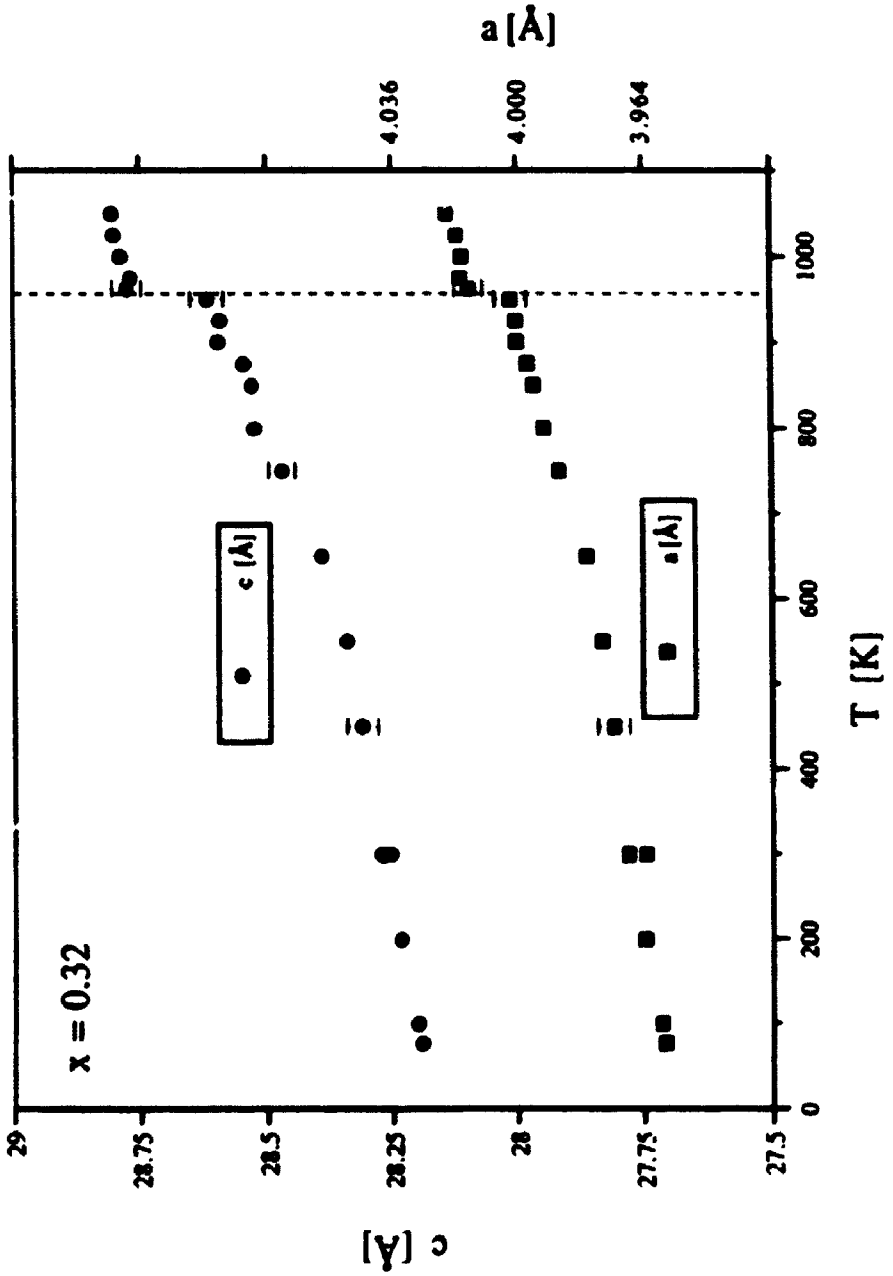

Figure 5.11 Temperature dependence of the a and c lattice parameters of β-$(Bi_2O_3)_{0.68}(SrO)_{0.32}$

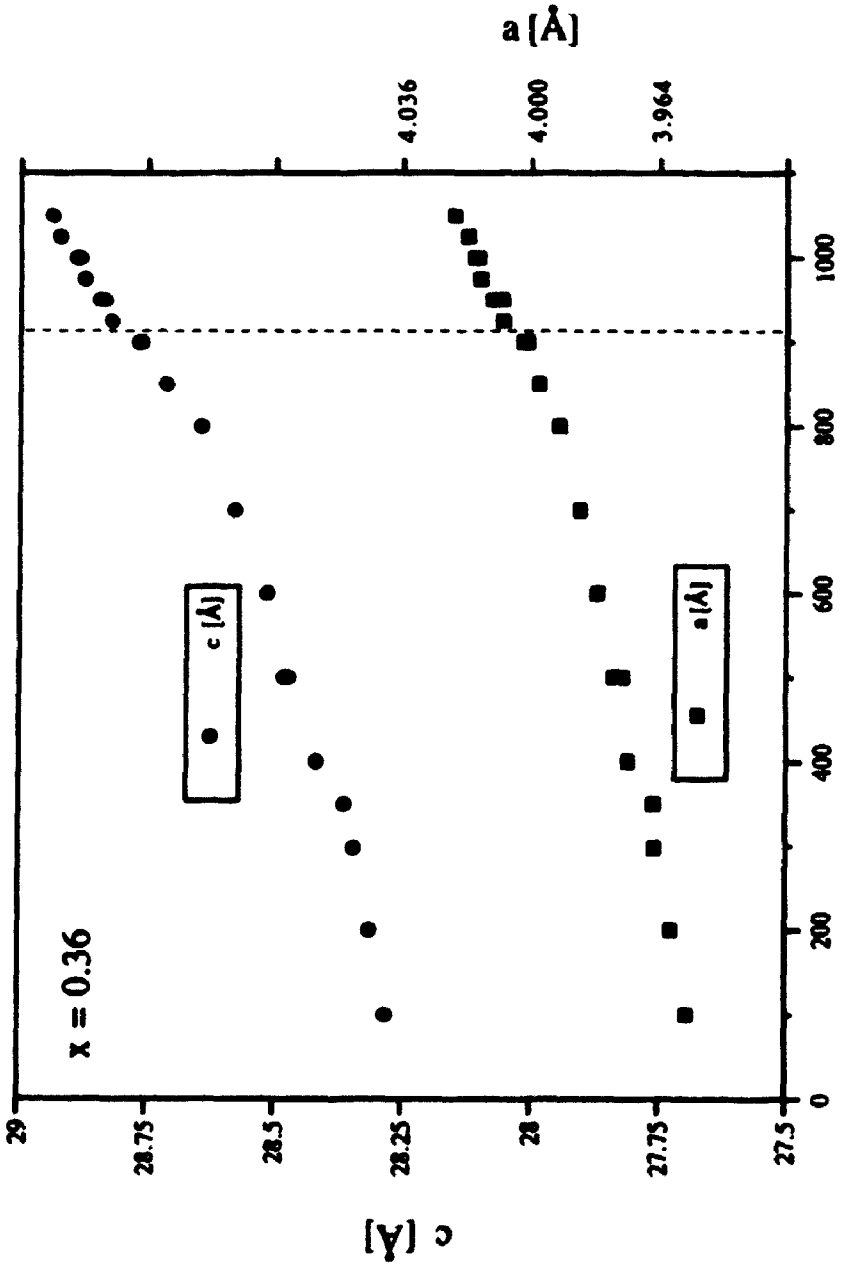

Figure 5.12 Temperature dependence of the *a* and *c* lattice parameters of β-$(Bi_2O_3)_{0.64}(SrO)_{0.36}$

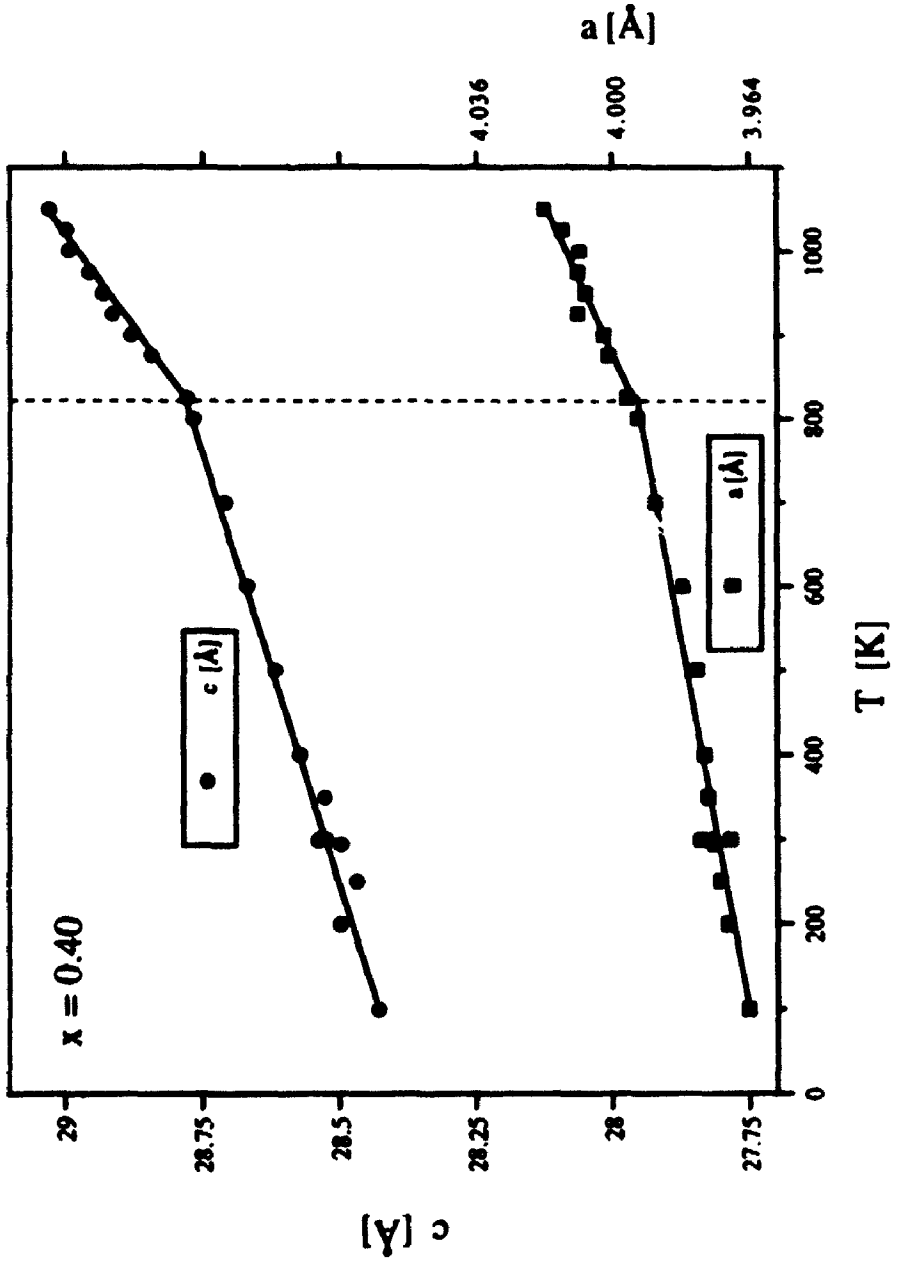

Figure 5.13 Temperature dependence of the a and c lattice parameters of β-$(Bi_2O_3)_{0.60}(SrO)_{0.40}$

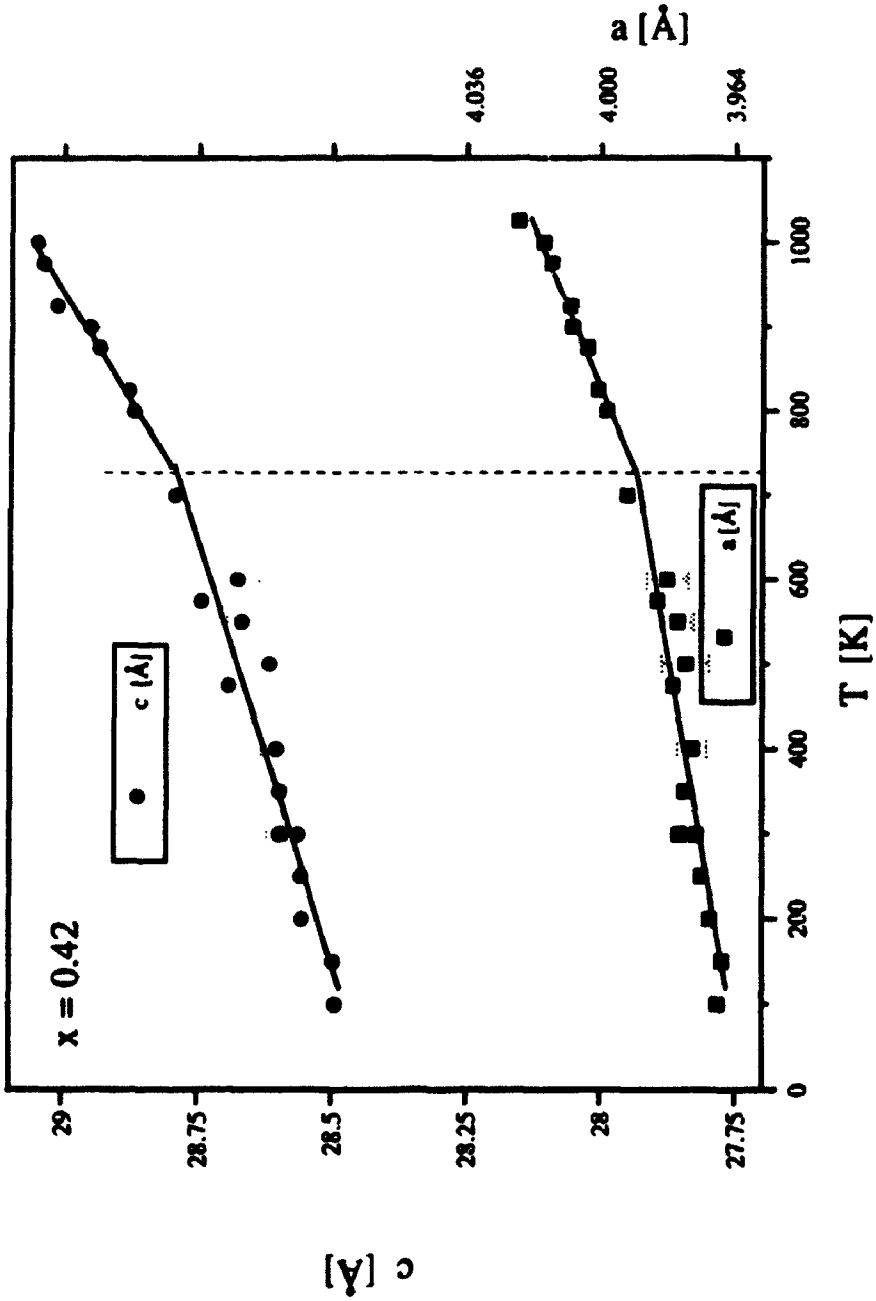

Figure 5.14 Temperature dependence of the *a* and *c* lattice parameters of β-$(Bi_2O_3)_{0.58}(SrO)_{0.42}$

temperature up to a temperature, T_{t1}, at which point there are distinct lattice parameter discontinuities, indicated by dashed vertical lines in the figures. For the two compositions $x > 0.36$, there is no discontinuity in the lattice parameters, to the limit of resolution of the method, but there is a sharp increase in the slopes of the lines at a temperature, T_{t2}, indicated by dashed vertical lines in the figures. These trends are also reflected in temperature dependence of the volume of the unit cell. For all compositions $x \leq 0.36$, the volume discontinuity ΔV occurs at the temperature T_{t1}, which may be considered to be a first-order effect. For compositions $x > 0.36$, an abrupt change in slope occurs at a temperature T_{t2}, which is indicative of a second-order effect, with a discontinuity in the first derivative, dV/dT.

The discontinuous increases in lattice parameters Δa and Δc, and in unit cell volume ΔV, observed at the transformation temperatures, T_{t1}, are plotted as a function of composition in Figure 5.15. The Δc results are in good agreement with those of Boivin *et al.* [11], but differ significantly from the higher order polynomial used to represent their data. The present results demonstrate that the magnitude of the Δc discontinuity falls off progressively with strontium concentration, and decreases to within the detection limit of the method at a composition between $x = 0.36$ and $x = 0.40$. In contrast, the ΔV and Δa discontinuities pass through a maximum around $x = 0.28$.

The presence of such discontinuous increases, Δa and Δc, in the respective lattice parameters are in direct agreement with the observations of Guillermo *et al.* [10] for a sample of the composition $x = 0.28$, which was shown previously in Figure 2.8, and provide strong confirmation of the proposed phase transformation $\beta_2 \leftrightarrow \beta_1$. The expansion of the *c* parameter is a consequence of an anisotropic weakening of the ionic bonds in directions parallel to the z axis of the hexagonal cell. In contrast, relatively small changes are observed in the *a* parameters due to the constraints imposed by the planes containing

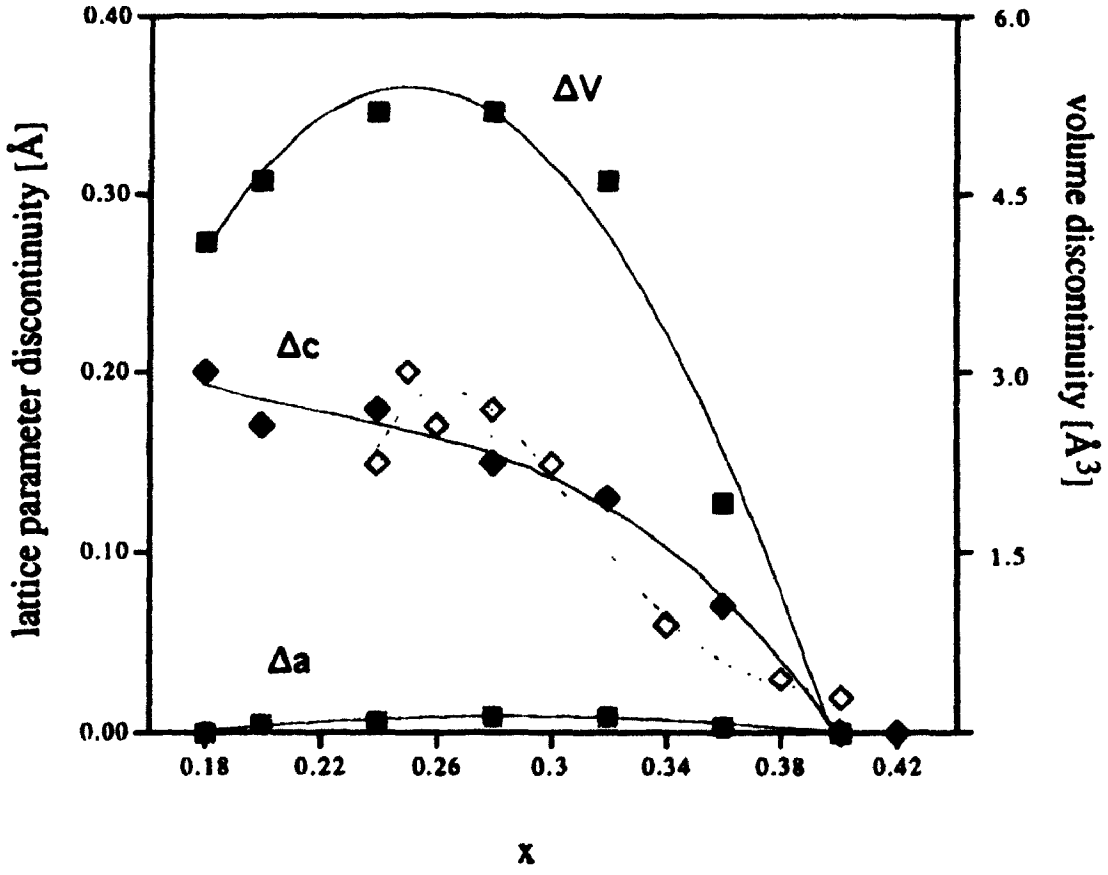

Figure 5.15 Composition dependence of the volume discontinuities, ΔV, and the lattice parameter discontinuities, Δa and Δc, as determined for β-$(Bi_2O_3)_{1-x}(SrO)_x$. The solid lines are 3rd order polynomials fit to the respective experimental data points. The open diamonds and dashed line are as reported by Boivin *et al.* for Δc

only bismuth cations, which are unaffected by the level of strontium concentration. As the relative intensities of the diffraction peaks do not show a significant change after cycling above and below the transformation temperatures, T_{t1}, this transformation cannot involve a modification of the cation sublattice at high temperatures. It may be postulated, however, that the occupied sites of the anion sublattice can be modified, since such a movement of the O^{2-} ions would not alter the relative intensities of the diffraction peaks due to the relatively low X-ray scattering factor of oxygen.

The form of the modification of the oxygen sublattice which generates the discontinuities Δa, Δc, and ΔV, must be such that it increases the mobility of anions in layers which lie normal to the z axis, to account for the observed increase in anionic conductivity. These discontinuities may thus be attributed to thermal excitation of oxygen anions into weakly-bound sites between the cation layers which provide high mobility, analogous to the excitation of carriers into the conduction band of semiconductors. As shown in Section 5.2.1 above, the c parameter is strongly dependent on compositions for $x \geq 0.28$, which is attributed to some weakening of the (Bi,Sr)-O bonds at increasing strontium concentrations, due to an increasing number of oxygen vacancies in the substituted layers. The reduction of the magnitude of the Δc discontinuity at higher strontium concentrations, shown in Figure 5.15, may be attributed to the increased number of oxygen vacancies in the substituted (Bi,Sr)-O layer which provide alternate sites to the highly mobile interlayer sites discussed above. This is consistent with the reduction in the Δc discontinuity and the concurrent observed reduction in ionic conductivity, with increasing strontium concentration.

5.4 Revisions to the Phase Diagram

The transition temperatures, T_{t1} and T_{t2}, are plotted as a function of composition, x, in Figure 5.16 with a 3rd order polynomial fit to the data. The other values in the plot consist of temperatures derived from Watanabe's DTA measurement at x = 0.38, Guillermo's sharp c-parameter increase at x = 0.28, and Boivin's T_t values for x = 0.26 and x = 0.38. The agreement between the present results and the literature values is very good. This graph shows once again that there is a change in characteristics on either side of a composition between x = 0.24 and x = 0.28, at which the ratio of bismuth to strontium ions at the "a" sites is inverted. Although it has not been established whether there are two distinct types of transformation, t_1 and t_2, the respective transformation temperatures do conform to the same composition-dependent curve, as shown in Figure 5.16.

The observed composition dependence of the transformation temperature T_t can be incorporated into the phase diagram of the Bi_2O_3-SrO system. For this purpose the recent phase diagram of Huang *et al.* [19] has been selected, because of its more detailed determinations of the intermediate compounds and phase boundaries. As shown in Figure 5.17, the amended diagram includes the compositional dependence of the $\beta_2 \leftrightarrow \beta_1$ phase boundary, with a maximum between x = 0.24 and x = 0.28. The $\beta_2 \leftrightarrow \beta_1$ phase boundary is uncertain beyond x > 0.36, since no distinct lattice parameter discontinuities (Δc, Δa, or ΔV) were observed at these higher strontium concentrations. This raises the possibility that, at compositions beyond x > 0.36, the β_1 phase may either transform by a second-order change to another low-temperature modification of the hexagonal structure, consistent with the observed change in slope of the lattice parameters and electrical conductivities, or even be stable down to ambient temperatures. In any event, the increased stability of the β_1 phase at high strontium concentrations is consistent with the proposal by Huang *et al.* [19] of a congruently melting composition at x = 0.415.

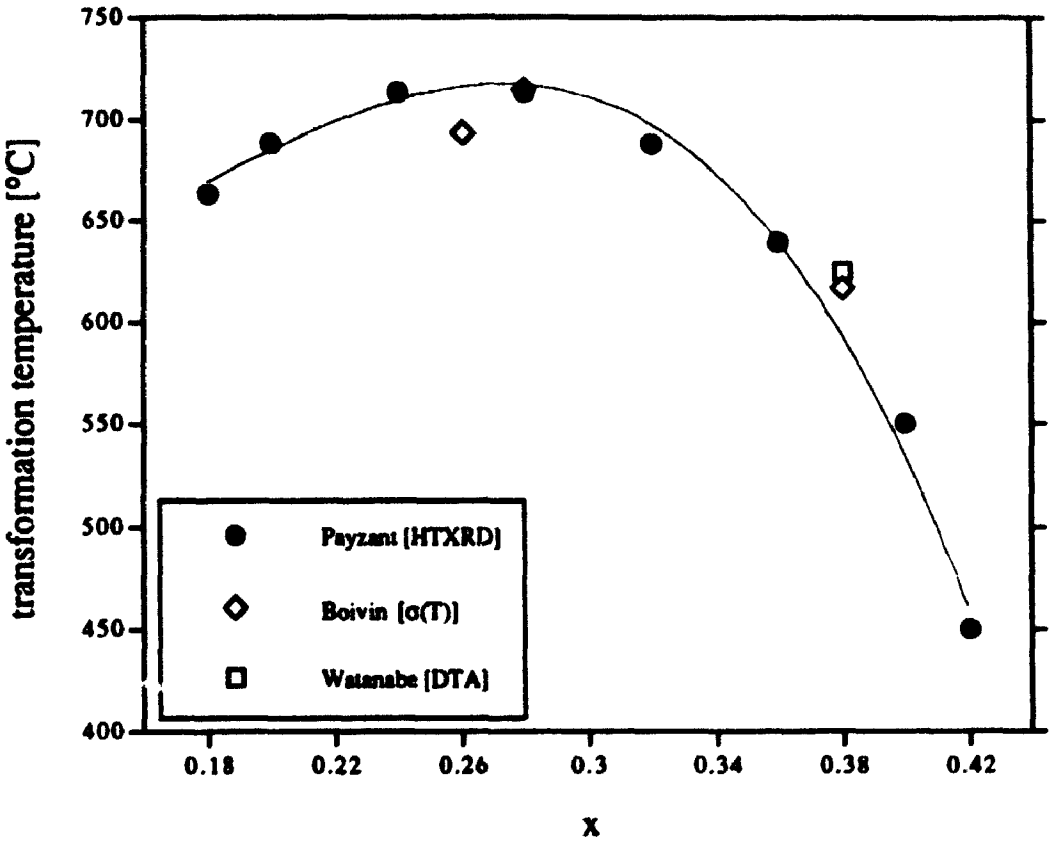

Figure 5.16 Composition dependence of transformation temperature T_t of β-$(Bi_2O_3)_{1-x}$ $(SrO)_x$. The solid curve is a 3rd order polynomial fit to the data, excluding the literature values

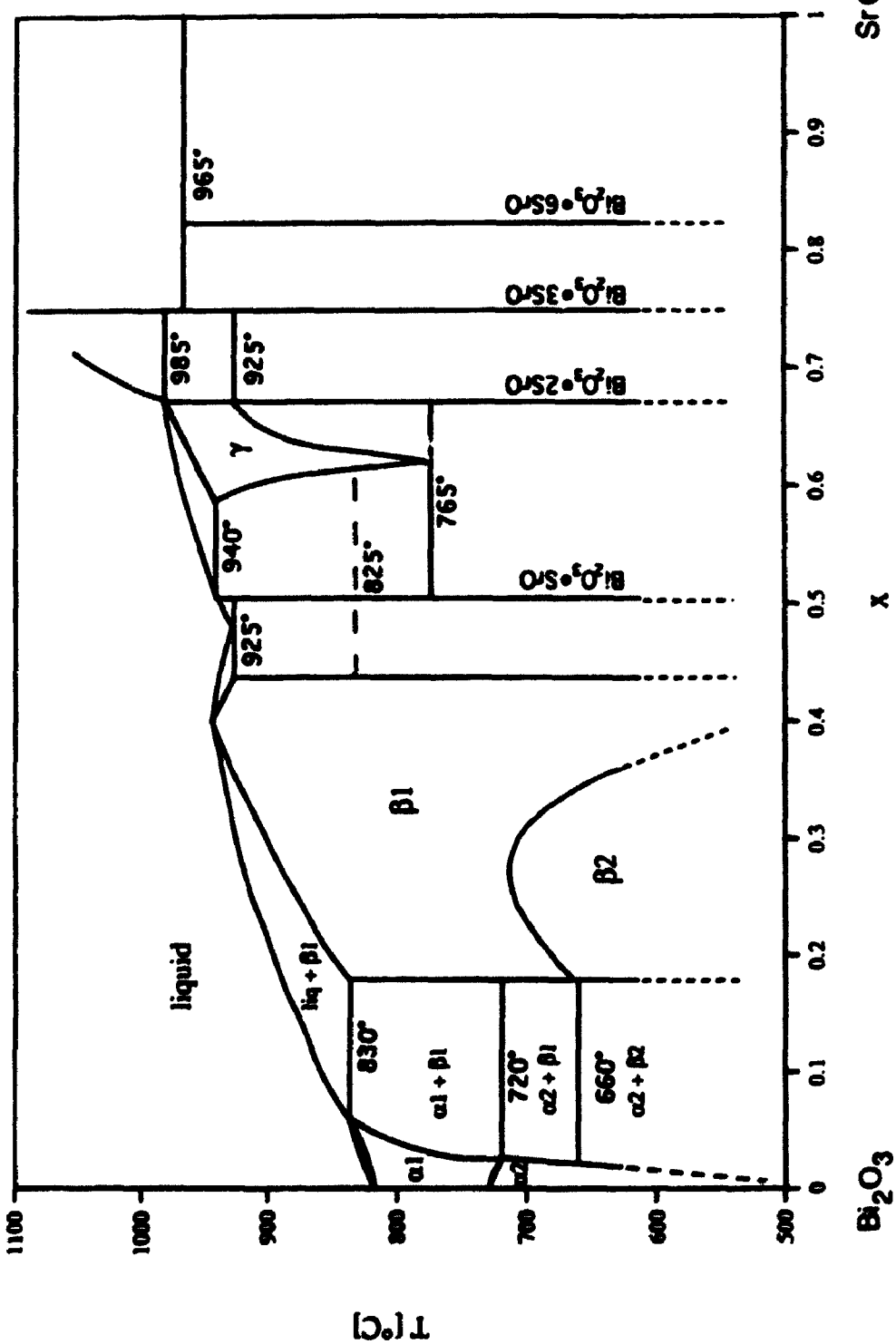

Figure 5.17 Amended Huang *et al.* Bi_2O_3-SrO phase diagram incorporating the new β_1-β_2 transformation temperature data

CHAPTER 6 - Conclusions

6.1 Conclusions:

The present work illustrates the advantage of combining information from a number of complimentary methods in order to determine accurate phase diagrams. This is of particular importance in systems such as Bi_2O_3-SrO where high temperature phases exist which cannot be stabilized at room temperature. Analysis by high temperature X-ray diffraction requires little sophistication when the phase transformation includes a significant structural change, but considerably more care was required to analyze the $\beta_1 \leftrightarrow \beta_2$ transformation, in which the structural changes were much more subtle. In this case, the extra information provided by differential thermal analysis and high temperature electrical conductivity justified a careful examination of the lattice parameters in the temperature ranges above and below the indicated transformation temperatures.

On the basis of the present study it has been concluded that :

1) the β-$(Bi_2O_3)_{1-x}(SrO)_x$ phase can properly be indexed as pseudo-hexagonal;
2) there is little or no compositional dependence of the *a* parameter of the β-phase;
3) the compositional dependence of the *c* parameter is increased at a composition near $x = 0.28$;
4) sharp discontinuities observed at high temperatures in the *a* and *c* parameters, and in the volume of the unit cell, are attributed to a phase transformation from the low temperature β_2 phase to the high temperature β_1 phase;
5) the temperature of the $\beta_1 \leftrightarrow \beta_2$ phase transformation has a maximum near a composition $x \approx 0.28$;

6) the $\beta_1 \leftrightarrow \beta_2$ phase transformation, t_1, unambiguously involves a significant discontinuous expansion in the *c* parameter with a much smaller expansion in the *a* parameter;

7) the magnitude of the discontinuous increase in the *a* parameter at T_{t1} passes through a maximum at the centre the β-phase;

8) the magnitude of the discontinuous increase in the *c* parameter at T_{t1} is greatest at low values of x and decreases with strontium concentration across the β-phase;

9) distinct lattice parameter discontinuities were not observed at high strontium concentrations, $x > 0.36$, but a change in the coefficient of thermal expansion is observed at a temperature T_{t2}, which decreases with strontium concentration, x;

10) the unit cell volume of the β-phase undergoes a discontinuous increase at low values of x and a continuous increase at high values of x;

11) as the hexagonal "a" sites of the β-phase structure are the only locations available to the solutes Sr^{2+} and Y^{3+}, the valence of the cation is not a factor in the designation of the solute sites and a competition is thus established for the occupancy of these sites when two or more cations are present;

12) the established temperature dependence of the $\beta_1 \leftrightarrow \beta_2$ phase transformation can be used to amend the phase diagram of the (Bi_2O_3)-(SrO) system;

13) at concentrations greater than $x = 0.36$ the high temperature β_1 phase may transform to another hexagonal structure by a second order phase transformation, or even be stable on cooling to ambient temperatures; and

14) the enhanced stability of the β_1 phase at high strontium concentrations is consistent with a reported congruently melting composition at $x = 0.416$.

6.2 Recommendations for Future Study

The solidus and liquidus of the β-phase of the Bi_2O_3-SrO system should be re-examined, to confirm the existence of the congruently melting composition reported by Huang *et al.*. It is also important to determine the precise composition of the congruently melting ceramic and to establish whether it has any relationship to the maximum in T_t observed in the present work. It would also be of interest to determine whether a spinodal decomposition occurs at a temperature above T_t, as observed in β-$(Bi_2O_3)_{1-x}(CaO)_x$.

Further neutron diffraction investigation of the structure of the β-phase should be performed to confirm the monoclinic superlattice structure and the precise location of the oxygen ions as a function of composition. High temperature neutron diffraction studies would also yield precise information on the changes in oxygen ion location associated with the $\beta_1 \leftrightarrow \beta_2$ phase transformation and thus provide a definitive explanation of the high ionic conductivity observed in these ceramics. Additionally, it may be possible to ascertain whether the high strontium β_1 phase decomposes by a second order phase transformation, or remains stable on cooling to room temperature.

APPENDICES

Appendix I

"Low Temperature Attachment for X-Ray Powder Diffractometry"
Advances in X-Ray Analysis, Vol. 37, pp. 457-463
Edited by J.V. Gilfrich *et al.*, Plenum Press, New York, 1994

Appendix II

"An Experimental Examination of Error Functions for
Bragg-Brentano Powder Diffractometry"
Advances in X-Ray Analysis, Vol. 36, pp. 663-670
Edited by J.V. Gilfrich *et al.*, Plenum Press, New York, 1993

Appendix III

"An Experimental Evaluation of Computational Methods for Determining Lattice
Parameters Using Bragg-Brentano Powder Diffractometry"
Advances in X-Ray Analysis, Vol. 37, pp. 87-93
Edited by J.V. Gilfrich *et al.*, Plenum Press, New York, 1994

LOW TEMPERATURE ATTACHMENT FOR X-RAY POWDER DIFFRACTOMETRY

H.W. King, M.A. Peters, E.A. Payzant and M.B. Stanley

Department of Materials Engineering
University of Western Ontario
London, ON, N6A 5B9
CANADA

Abstract

A low temperature attachment based on a miniature open-cycle Joule-Thomson refrigerator has been developed for x-ray diffractometry measurements over the temperature range from 65 - 400 K. By use of a special mounting plate, the device can be substituted for the heater assembly of a high temperature attachment and thereby utilize the available vacuum chamber and x-ray transparent beryllium window. The device is demonstrated by investigating the polymorphic phase transformations that occur in barium titanate.

Introduction

Continuous flow cryostats for cooling x-ray diffractometer samples have been applied successfully over the temperature range of 2-473 K using liquid helium, and 65-473 K using liquid nitrogen (1). However, these devices tend to be relatively expensive to operate and require considerable time for re-alignment and turn-around between samples. For optimum usage they are best mounted on diffractometers that can be assigned to specific projects for relatively long periods. Alternative cooling devices for intermittent use in a general diffraction laboratory, require short cool-down times, easy sample exchange and minimum instrumental re-alignment. Closed-cycle Joule-Thomson refrigerators, which are considerably smaller in bulk and have much lower operating costs than continuous flow cryostats, cannot be used effectively for low temperature x-ray diffraction, however, because of the excessive sample vibration caused by the reciprocating pistons in the compressor. Cryostats based on the Peltier effect have proved very effective for cooling electronic instrumentation, but at the present state of the art the lowest operating temperature of these devices is limited to ~200 K. Miniature open-cycle Joule-Thomson refrigerators offer considerable possibilities for low temperature x-ray diffraction, since these devices have proved successful for the cooling of sample stages for electron microscopy, where a very low level of sample vibration is mandatory. The operating temperature of an open-cyle Joule-Thomson refrigerator depends on the working gas, being 65-400 K for nitrogen, 30-85 K for neon and 2-30 K for helium. In principle, a multi-stage Joule-Thomson device could thus be fabricated to operate over the range from 2-400 K. The present paper is concerned with the development of a single stage device for rapid cycling of x-ray diffraction samples over a temperature range of 65-400 K, using a commercial [MMR Technologies Inc., Mountain View, CA] Joule-Thomson refrigerator cooled by nitrogen gas. The device can be substituted for the heater assembly of a high temperature x-ray diffractometer attachment, to utilize an existing vacuum chamber with an x-ray transparent beryllium

Advances in X-Ray Analysis, Vol. 37, Edited by
J.V. Gilfrich *et al.*, Plenum Press, New York, 1994

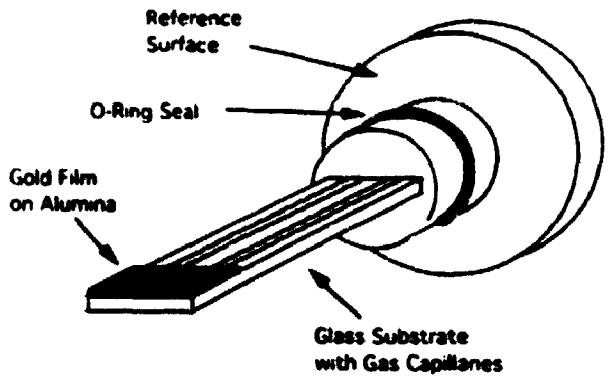

Figure 1. MMR Joule-Thomsor Refrigerator

window. The effectiveness of this cooling device is demonstrated by investigating the polymorphic phase transformations that occur in the compound barium titanate.

Experimental

The MMR Joule-Thomson miniature open-cycle refrigerator is cooled to 77 K by the expansion of high pressure (>1800 psi) nitrogen gas in a cavity, the upper surface of which is in direct thermal contact with a flat gold-coated alumina pad, as shown in Fig. 1. A sample to be cooled is placed on the gold surface and, if so required, increased thermal contact can be achieved by using silicone grease. The efficiency of the refrigerator is improved by pre-cooling the incoming gas by passing it through an integral counterflow heat exchanger cooled by the exhaust gas. Temperatures between 65-77 K are obtained by reducing the vapour pressure of the liquefied nitrogen, using a vacuum pump attached to the exhaust port of the refrigerator. Intermediate temperatures between 300 and 65 K are obtained by offsetting the cooling by activating a silicon resistance heater embedded in the alumina pad. This heater also enables the device to be used (without the cooling gas) at temperatures between 300 and 400 K. The temperature is monitored with a calibrated silicon diode sensor, which is also embedded in the alumina pad and linked to a programmable controller [MMR K-20].

Adapting the MMR miniature refrigerator for low temperature x-ray diffractometry (LTXRD) required a vacuum chamber with windows of very low x-ray attenuation. A high temperature x-ray diffractometer attachment [Buehler HDK2.3] with curved beryllium windows, available in the authors' laboratory, was adapted for this purpose by machining a special mounting plate to support the refrigerator in place of the heater assembly. Rapid sample mounting and replacement is achieved, since this plate can be removed and replaced without disturbing the alignment of the vacuum chamber, which remains firmly attached to the diffractometer goniometer, as shown by the schematic sketch in Fig. 2. The refrigerator is mounted in a sliding O-ring fitting machined in the adaptor plate, so that its external flange abuts against a reference surface which assures that the centre of the gold covered alumina pad is located along the central ray of the x-ray beam. The rotational alignment of the surface of the gold coated alumina pad is maintained by a pin which fits in a hole machined in the plate. As shown in this figure, gas inlet and outlet ports, and the electrical feedthroughs for the heater and thermometer pass through the body of the refrigerator, so that the vacuum of the chamber is not compromised.

To automate the control of the refrigerator, the MMR controller was linked to a 386 PC computer via an RS-232 interface at 5400 baud and software routines were written to enable the following functions:

- Monitor and control temperature
- Acquire and digitally store temperature and power data at specified time intervals
- Ramp to several different temperatures and hold for a set time
- Real-time graphical display

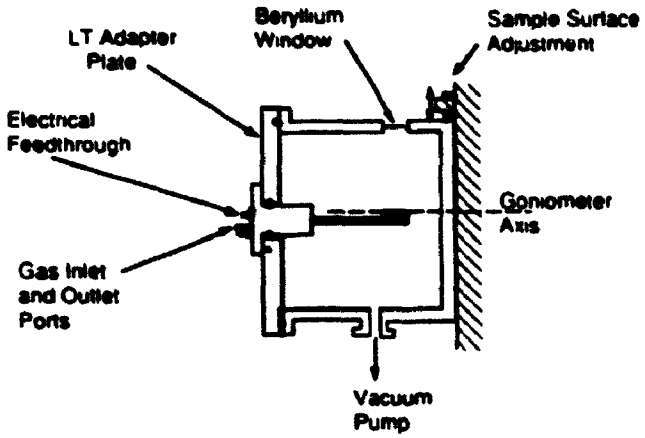

Figure 2. Schematic of Low Temperature Attachment

The low temperature attachment is aligned by the following procedure. To provide an approximate alignment, the position of the heater surface of the high temperature furnace attachment is first aligned in accordance with the procedures for this device. The heater is then replaced with the refrigerator, using the adaptor plate, and the position of the sample surface with respect to the axis of the goniometer is determined by measuring the positions of the diffraction peaks from the gold layer on the alumina pad. Using the LCLSQ (version 8.4) software program (2), the displacement of the surface of the gold coated pad can be refined, together with the lattice parameter of the gold layer. In practice, the surface of the gold layer is deliberately set slightly lower than the plane of the x-ray beam, when the goniometer is set at the zero degree position, so that a powder sample placed on top of the gold layer will lie close to the true zero plane passing through the axis of the goniometer. To enable the gold surface layer to be used as an internal standard, its lattice parameter was measured at 50 degree intervals, over the operational temperature range of the refrigerator. An advantage of gold for this purpose, is that only small number of diffraction peaks are generated with Cu K_α radiation (a total of eight up to 153 °2θ), resulting in relatively little interference with the diffraction pattern of a sample under investigation.

To evaluate the low temperature cooling device, a powdered sample of barium titanate [National Lead Co.] was placed on the surface of the gold coated alumina pad of the refrigerator, using a drop of acetone to aid in spreading. After the acetone was evaporated, the adaptor plate was attached to the vacuum chamber, which was evacuated with a roughing pump. X-ray diffractograms from the gold coating and from the barium titanate sample were obtained with a Scintag XDS 2000 diffractometer in the θ:θ mode, using a copper x-ray tube operated at 45 kV and 40 mA, and a solid state HPGe detector. For structural identification, diffraction profiles were scanned from 42.0 - 54.0°2θ at an equivalent scanning speed of 0.75 °/min., with a step interval of 0.03° and a 0.3 mm receiving slit. For determining precision lattice parameters for the gold layer at different temperatures, the angular region surrounding each diffraction peak was scanned at an equivalent scanning speed of 1 °/min., with a step interval of 0.03° and a 0.3 mm receiving slit. The peak positions were determined by profile fitting a Pearson VII profile to the raw data file, and lattice parameters were determined using a software extrapolation method based on Vogel and Kempter (3). During heating and cooling cycles over the range from 71 K to 400 K, the temperature was set and controlled to within ±0.2 K at intervals of 25 K for barium titanate structure determination, and at intervals of 50 K for determining the lattice parameters of the gold film.

Results and Discussion

A typical cooling and heating display, generated from temperature-time data stored in the computer, is shown in Fig. 3. This display confirms that, when using a gas inlet

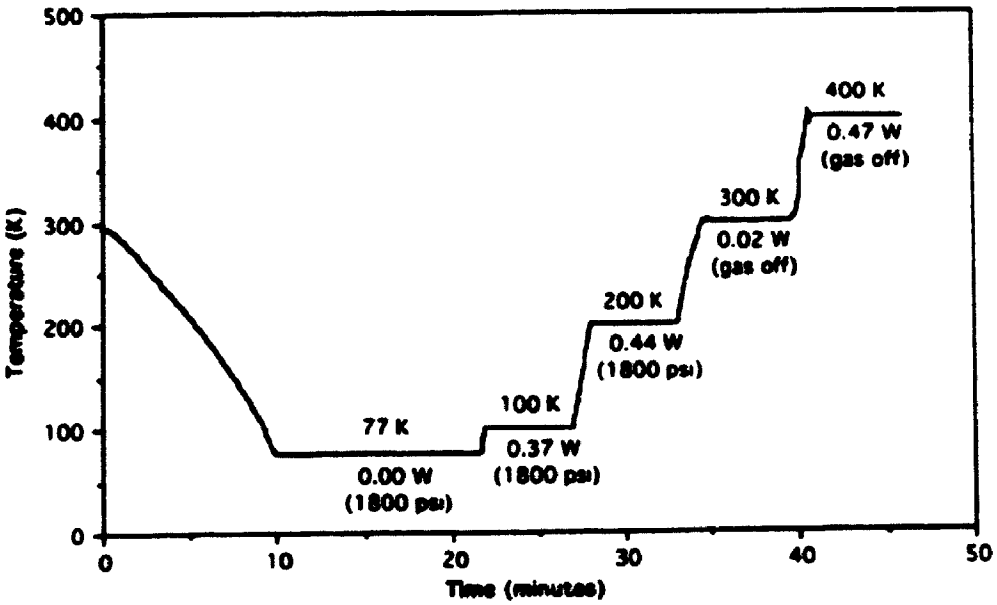

Figure 3. Plot of temperature-time data for heating and cooling cycles

pressure of 1800 psi, an x-ray powder sample can be cooled from room temperature to 77 K in less than 10 min., and maintained at this temperature to within ±0.2 K for a period of time specified in the computer input. The display also demonstrates that, by supplying increasing amounts of power, the heater is effective for adjusting and maintaining the temperature of the sample to within ±0.2 K of operator-selected intermediate temperatures between 77 and 300 K, for prescribed periods of time. Time-temperature plots with the same degree of temperature selection and control are obtained during step-cooling from 300 to 77 K, when the cooling is arrested by supplying decreasing amounts of power to the heater. For operation above 300 K, the nitrogen gas flow is turned off, and the temperature is controlled by the heater alone. As indicated by the initial section of the heating plot at 400 K in Fig. 3, the lack of a thermal sink provided by the cold nitrogen gas causes a small degree of overshoot to occur as the prescribed temperature is reached. An examination of the actual time-temperature data stored in the computer shows that at the maximum temperature of 400 K, the degree of overshoot is ≤ 2 K, and that within 15 seconds the temperature is subsequently controlled to within ±0.2 K. Temperatures below 77 K can be obtained by connecting a vacuum pump to the gas outlet port of the refrigerator.

The diffraction patterns obtained for the barium titanate sample after cooling to 150 K and subsequently step-heating to 400 K are given in Fig. 4. As shown in the figure, the structure of barium titanate at 150 K is rhombohedral. When the sample is heated to 225 K the rhombohedral structure transforms to monoclinic, as evidenced by splitting of the rhombohedral *202* peak, which occurs at 45.5 °2θ. This structural transformation may be described as rhombohedral-orthorhombic, in which case the peak splitting observed at 200 K can be attributed to the formation of a doublet composed of overlapping *220* and *002* diffraction peaks. On further heating to 300 K, the order of the intensities of the diffraction peak at 45.5 °2θ reverses, which is indicative of the transformation to the tetragonal form of barium titanate. These peaks may now be indexed as *002* and *200*. The tetragonal structure is maintained up to the highest obtainable temperature of 400K, but as this temperature is approached the tetragonal doublet at 45.5 °2θ shows a lack of resolution into two peaks, and takes on the appearance of a broadened cubic profile. This is consistent with the proximity of this temperature to the values of 393-403 K (120-130°C) quoted in the literature for the tetragonal-cubic transformation in barium titanate (4-10).

Equivalent diffraction patterns were obtained during the reverse temperature sequence, *i.e.* after heating to 400 K and subsequently step-cooling to 150 K. During this cooling

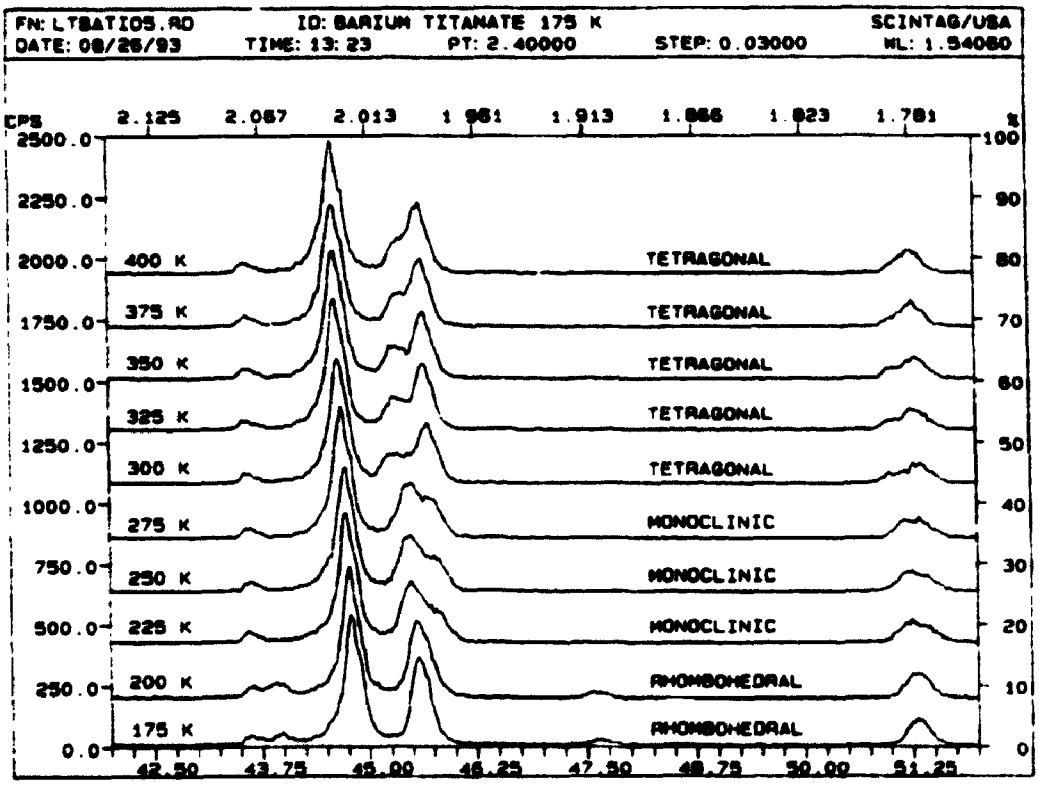

Figure 4 X-ray diffractograms for barium titanate during step heating from 175-400 K

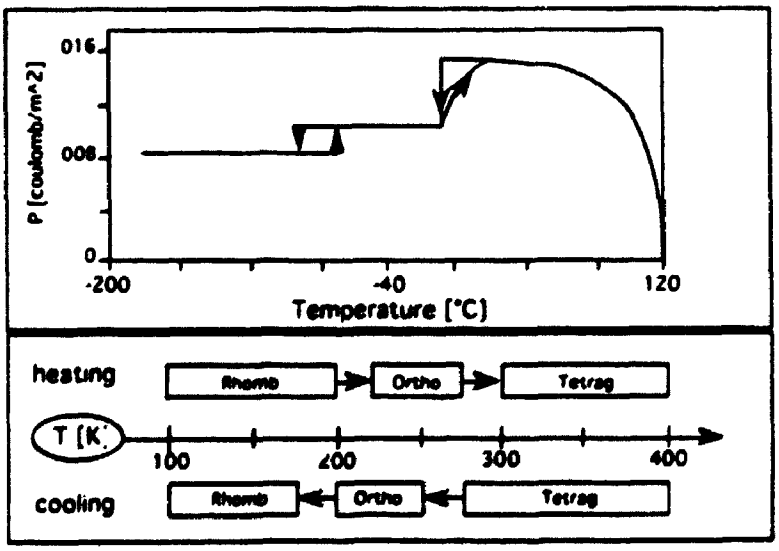

Figure 5 Comparison of the polarization data of Merz (8) to the present structure results

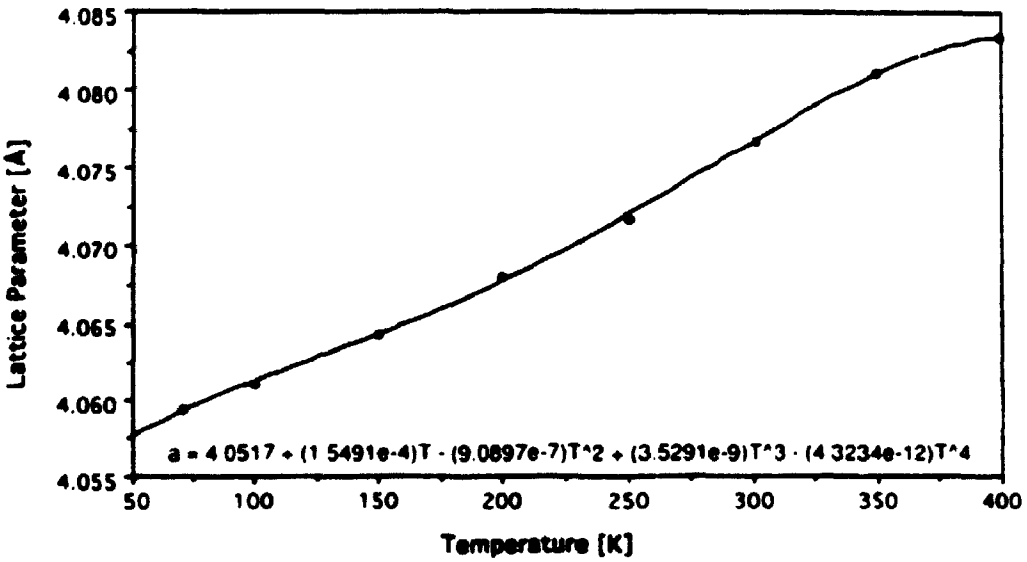

Figure 6. Lattice Parameter of Gold from 71 - 400 K

sequence, the tetragonal-monoclinic transformation occurred between 275 K and 250 K, while the monoclinic-rhombohedral transformation occurred between 200 K and 175 K, as shown in the schematic diagram in Fig. 5. The precise transformation temperature cannot be determined with a temperature step of 25 °C. Nevertheless, the agreement between the observed structural transformation temperatures and those reported in the literature, on the basis of polarization measurements (8-10) and x-ray diffraction studies (4-7), confirms the effectiveness of the low temperature cooling and heating stage for investigating phase transformations over the temperature range 65-400 K.

To provide an internal standard for checking the alignment of the diffractometer at low temperatures, the lattice parameter of the gold layer was determined over the operational temperature range from 71-400 K. As shown in Fig. 6, the results conform to a nonlinear plot which can be accurately represented by the 4th order polynomial equation given in the figure. It is necessary, of course, to make an additional correction for the position of the gold layer surface with respect to the centre of mass of the powder sample, when using this relationship as an internal standard for determining the precision lattice parameter(s) of a test sample. In any event, the gold peaks may be used to quickly and accurately establish the sample surface position on an otherwise well-aligned goniometer.

Acknowledgement

This work was supported in part by a grant from the Natural Sciences and Engineering Research Council.

References

1. W.A. Little, "Microminiature Refrigeration", *Rev. Sci. Instrum.*, **55** 661-680 (1984).
2. C.W. Burnham, "Refinement of Lattice Parameters Using Systematic Correction Terms", *Carnegie Inst. of Washington Yearbook*, **64** 200-202 (1965).
3. R.E. Vogel and C.P Kempter, "A Mathematical Technique for the Precision Determination of Lattice Parameters", *Acta Cryst.*, **14** 1130-1134 (1961).

4. H.L. Megaw, "Crystal Structure of Double Oxides of the Perovskite Type", *Proc. Phys. Soc.*, **58** 133-152 (1946).

5. R.G. Rhodes, "Structure of $BaTiO_3$ at Low Temperatures", *Acta Cryst.*, **2** 417-419 (1949).

6. L. Carlsson, "Crystal Structure Changes in $BaTiO_3$", *Acta Cryst.*, **20** 459 (1966).

7. H.F. Kay and P. Vousden, "Symmetry Changes in Barium Titanate at Low Temperatures and their Relation to its Ferroelectric Properties", *Proc. Roy. Soc.*, **40** 1019-1039 (1949).

8. W.J. Merz, "The Electric and Optical Behavior of $BaTiO_3$ Single-Domain Crystals", *Phys. Rev.*, **76** 1221-1225 (1949).

9. F. Jona and G. Shirane, *Ferroelectric Crystals*, Pergammon Press, London (1962).

10. T. Ikeda, *Fundamentals of Piezoelectricity*, Oxford University Press, Oxford (1990).

AN EXPERIMENTAL EXAMINATION OF ERROR FUNCTIONS FOR BRAGG-BRENTANO POWDER DIFFRACTOMETRY

H.W. King and E.A. Payzant

Department of Materials Engineering
University of Western Ontario
London, ON, N6A 5B9
CANADA

Abstract

A single function for the elimination of errors in precision lattice parameter determination has not been developed for the Bragg-Brentano x-ray diffractometer method, because of the different angular dependencies of the systematic errors. A review of the error functions shows that all but one can be calculated from the instrumental settings and known properties of a sample under investigation. The residual sample displacement error can be then be eliminated by using extrapolation plots or computer methods to correct the data to $\cos\theta\cot\theta$ plots. The slopes of $\cos\theta\cot\theta$ plots can also be used to align high temperature furnaces and low temperature cryostats mounted on x-ray diffractometers.

Introduction

The systematic errors affecting the position of Bragg reflections detected by the Bragg-Brentano x-ray diffractometer were reviewed at the Denver X-ray Conference some thirty years ago by Vassamillet and King (1). At that time, it was accepted that a single extrapolation function, equivalent to the Nelson-Riley function for the Debye-Scherrer film method, could not be developed for the x-ray diffractometer, because of the different angular dependencies of the error functions. As a compromise, it was proposed that $\cos^2\theta$ be adopted as an extrapolation function, provided its application be limited to Bragg reflections recorded at 2θ angles greater than 120 degrees. While this did not present a severe restriction when diffraction patterns were routinely scanned up to 165 °2θ using physically small proportional or scintillation counters, many modern diffractometers are equipped with bulky solid state detectors which restrict scanning to angles below 150 °2θ, particularly when using attachments which require the theta:theta mode. It thus seems timely to re-examine the known errors associated with the Bragg-Brentano diffractometer, with the aim of identifying the significant errors and correcting them by using extrapolation plots or computer analysis with respect to specific systematic error functions.

Advances in X-Ray Analysis, Vol 36, Edited by
J V Gilfrich *et al* Plenum Press, New York, 1993

Systematic Errors in Bragg-Brentano Diffractometry

The angular dependence of factors which cause a displacement ($\Delta\theta$) in the position of diffracted beams in Bragg-Brentano diffractometry are summarized in Table I. Since computer techniques are widely used to establish the $K_{\alpha 1}$ peak position, by stripping away the $K_{\alpha 2}$ peak using the Rachinger correction (2) and applying background removal, peak finder and/or profile fitting programs, it is important to note that although most of the analytical functions in Table I were originally analyzed in terms of shifts in the centroid of the diffraction profile, these error functions also apply to shifts in peak position (3). An exception occurs in the case of the combined effects of dispersion, Lorentz and polarization, where the centroid displacement varies as $\tan^3\theta$ (4,5), while the shift in peak position varies as $\tan\theta$ (as indicated in Table I), because errors in peak position due to Lorentz and polarization are of the same form, but opposite sign, and thus cancel out (6). When this $\tan\theta$ function for $\Delta\theta$ (expressed in radians) is substituted in the differential form of the Bragg equation

$$\Delta d/d = -\cot\theta\,\Delta\theta \qquad \text{equation 1}$$

the fractional error in interplanar spacings ($\Delta d/d$) is found to be independent of the Bragg angle and can thus be corrected by simply multiplying the derived lattice parameter(s) by a numerical factor. Other physical errors such as refraction (7), shifts in wavelength caused by filters and monochromators (8,9) and errors in the definition of wavelengths (10), can be corrected by applying correction factors to derived lattice parameters. The $\tan\theta$ dependent $\Delta\theta$ error arising from a misalignment δ of the x-ray beam with respect to the diffraction plane (11), also results in a constant error in $\Delta d/d$, which can be corrected by applying a numerical constant to the derived lattice parameter(s), as in the case of the physical errors. However, the magnitude of this error when using two sets of Soller slits is generally below the level of significance for the determination of lattice parameters to 1:50,000 (1). The non-vanishing component of the axial divergence error is also corrected by applying a similar multiplication factor (12).

It also follows from equation 1 that the magnitude of the fractional error in d-spacings ($\Delta d/d$) due to random errors in the measurement of Bragg angle has $\cot\theta$ dependence. If all

Table I. Factors Affecting the Displacement of Diffraction Beams ($\Delta\theta$) and Fractional Errors in Interplanar Spacings ($\Delta d/d$) for Bragg-Brentano Diffractometry

Factor	$\Delta\theta$	$\Delta d/d$	Ref
Dispersion, Lorentz and polarization	$+3\beta\tan\theta/2\lambda$	constant	4
Beam not in diffraction plane	$\tan\theta(1-\cos\delta)$	constant	11
Axial divergence (non-vanishing term)	$+Q_2\cos 2\theta\, h^2/6R^2$	constant	12
Random error in 2θ measurement	$\pm\Delta\theta$	$\pm\cot\theta\,\Delta\theta$	1, 13
Ellipticity of diffractometer gears	$\pm\Delta\theta$	$\pm\cot\theta\,\Delta\theta$	1
Electronic time constant	$+\Delta\theta$	$\cot\theta\,\Delta\theta$	14
Poor counting statistics	$\pm\Delta\theta$	$\pm\cot\theta\,\Delta\theta$	15
Backlash in driving gears	$\pm\Delta\theta$	$\pm\cot\theta\,\Delta\theta$	1
Primary beam not at zero 2θ	$\pm\Delta\theta$	$\pm\cot\theta\,\Delta\theta$	1
Specimen surface displacement	$\pm\cos\theta\, S/R$	$\pm\cos\theta\cot\theta\, S/R$	17
Flat specimen (horizontal divergence)	$-\cot\theta\,\gamma^2/12$	$+\cot^2\theta\,\gamma^2/12$	17
Transparency (absorption)	$-\sin\theta\cos\theta/2\mu R$	$+\cos^2\theta/2\mu R$	17
Axial (vertical) divergence	$-Q_1\cot 2\theta\, h^2/6R^2$	$+\cos^2\theta\,(Q_1+Q_2)\,h^2/12R^2$	12

S = specimen surface displacement
R = goniometer radius
$2h$ = height (width) of irradiated surface of specimen (same as beam height)
$q = sR/lh$, where s and l refer to the spacing and length of the Soller slit foils
Q_1 and Q_2 are complex functions of q as defined in reference (12)
μ = absorption coefficient
γ = angular width of divergence slit

Bragg angles are measured to the same degree of accuracy, the magnitude of the fractional error in d-spacing calculated from the position of a particular Bragg peak will decrease with increasing Bragg angle. When d-spacings or lattice parameter data are plotted against a function of θ, error bars for $\pm\Delta d$, or $\pm\Delta a$, will thus lie within a cone which tapers to zero at 90°θ. Sinusoidal $\Delta\theta$ errors arising from ellipticity in the gears of the diffractometer can be corrected by direct calibration (1) or by the use of an external standard (13). Errors due to electronic time constants (14), counting statistics (15), and backlash in the gears (1), can be reduced below the level of significance by proper experimental procedures, or eliminated at source by the use of computer-controlled stepping motors, as in most modern goniometers. A misalignment of the centre of the primary beam from zero °2θ causes a $\Delta\theta$ error which is the same for all measured Bragg angles (1), and is thus additive with respect to the random errors in peak position. Diffractometers with a facility for translating the 180 °2θ point of the goniometer scale with respect to the focal spot of the x-ray tube may also have a $\Delta\theta$ error which is a combination of a shift in angular scale and a displacement of specimen position (1).

Bragg-Brentano de-focusing errors arising from a mis-setting of the 2θ:θ following (16) or the width of the source and detector slits (16) cause the diffraction profile to be broadened symmetrically, but not shifted in position. Other geometrical errors result in an asymmetrical broadening of the diffraction profile, with a systematic shift in the position of the measured Bragg peak. Displacement of the specimen surface with respect to the focusing circle ($\pm S$), causes a peak shift which has cosθ dependence (17). The error due to the use of a flat specimen, which is governed by the width of the horizontal divergence slit, γ, varies as cotθ (17); while the error due to specimen transparency, which is governed by the absorption coefficient, μ, has sinθcosθ dependence; and the systematic component of the axial (vertical) divergence error, which is controlled by the dimensions of the Soller slits, varies as cot2θ (12).

When the various error functions for the systematic Bragg angle shifts, $\Delta\theta$, are substituted (in radians) in equation 1, three further analytical functions are obtained for the θ-dependence of the fractional error in d-spacings, $\Delta d/d$, *i.e.*, cosθcotθ, $\cot^2\theta$ and $\cos^2\theta$, as indicated in Table 1. The $\Delta d/d$ errors due to flat specimen, transparency and the θ-dependent component of vertical divergence are always positive, but the sign of the error due to specimen surface displacement will be either plus or minus for all of the data points (depending on whether the specimen surface lies inside or outside the focusing circle).

As all three of the systematic error functions for $\Delta d/d$ in Table 1 converge to zero as θ approaches 90 °, their relative significance to a particular set of diffraction data can, in principle, be assessed by plotting $\Delta d/d$ values for the different Bragg reflections against each function in turn, and determining which gives the best fit to a linear plot. This cannot be performed in practice, however, unless the correct d-spacings are known *a priori*, e.g. by using a material with authoritatively accepted lattice parameters, such as the standards produced by NIST (18). For cubic materials with a single lattice parameter a, the relative importance of the systematic errors can be established from plots of a parameters derived from various Bragg reflections against the different error functions, since for cubic crystals $\Delta d/d = \Delta a/a$. In this context, the magnitude of the errors in a parameters determined from different Bragg reflections could be calculated directly by using the error functions in Table 1 combined with relevant information on instrumental specifications, experimental settings and material properties. The errors caused by flat specimen, effective transparency and axial divergence can be treated in this manner, but similar calculations and corrections cannot be performed for a misalignment of the specimen surface, because the sign and magnitude of the displacement S are both unknown.

The residual systematic error due to a specimen surface displacement S can be investigated from plots of a parameter of a cubic material against cosθcotθ, after correcting the data for flat specimen, transparency and axial divergence errors. The slope of such a plot will be either positive or negative, depending on the sign of the displacement, and the scatter of the data from a linear plot will be indicative of the magnitude of the random errors in the measurement of θ. Using powdered samples of silicon and tungsten - which were selected

because of their wide difference in x-ray absorption - plots of *a* parameter against various error functions were examined visually to determine the angular range over which the different functions are effective and to distinguish between systematic and random errors. A successive paper will be concerned with a computer least squares analysis of these results, and of similar diffraction data obtained using NIST standards (18), with an emphasis on distinguishing between the treatment of systematic and random errors, so that the findings can be available for incorporation into least-squares refinement programs for correcting errors over the whole range of measured Bragg angles.

Experimental

Specimens for x-ray examination were prepared from ~6 μm powder of 99.98 % silicon (Koch Light) and 99.7 % tungsten (Fisher) by: a) front-loading into a cavity mount; b) back-loading into an open mount covered with a 0.060 mm thick layer of adhesive tape; and c) dusting a thin layer of powder on to a glass slide.

X-ray diffraction examination was performed with a Scintag XDS 2000 X-ray diffractometer equipped with a high purity Ge solid state detector and set in the theta:theta mode. Copper radiation ($\lambda_{Cu_{k\alpha 1}}$ = 1.54060 Å) was used for all experiments, with the tube voltage set at 45 kV and the current at 40 mA. After establishing the approximate positions of the diffraction profiles by step-scanning at an effective scan rate of 10 °/min, each identified profile was step-scanned at an effective rate of 0.5 °/min, using a divergence slit γ of 0.72 °, a receiving slit of 0.05 mm (0.01 °), a chopper increment of 0.01 ° and an increment time of 1.2 sec. Background and $K_{\alpha 2}$ stripping programs were applied to the data, and the positions of the resultant $K_{\alpha 1}$ peaks were determined using a profile fitting program. These peak positions were used to determine the *d*-spacings and of the relevant diffracting planes of the silicon and tungsten powders.

The *a* parameters obtained from the *d*-spacings determined from the Bragg diffraction peaks were corrected for the flat specimen error using the function $+\cot^2\theta\,\gamma^2/12$; for transparency errors using $+\cos^2\theta/2\mu R$; and for systematic axial divergence errors using $+\cos^2\theta\,(Q_1+Q_2)\,h^2/12R^2$. The instrumental parameters used for these corrections were R = 250 mm, h = 5.5

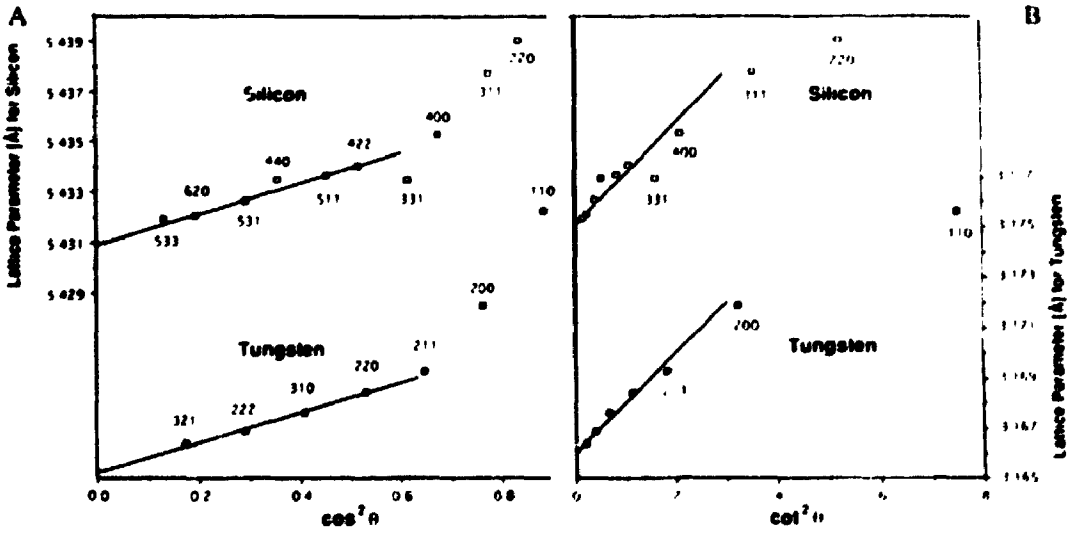

Fig. 1. Plots of *a* parameters of Si and W. A: versus $\cos^2\theta$. B: versus $\cot^2\theta$

mm, s = 0.5 mm and l = 25 mm. A value of q = 0.91 obtained from the dimensions of the Soller slits was used to obtain values of Q_1 = 0.36 and Q_2 = 0.03 from graphs given in reference 12. Assuming the powder samples to be ~60 % of theoretical density, the effective absorption coefficients for the Si and W specimens were taken as 85.8 cm^{-1} and 1950.8 cm^{-1}, respectively.

Results and Discussion

Lattice parameters calculated from the positions of the various Bragg reflections for the front loaded powder samples of Si and W were plotted against the functions $\cos^2\theta$, $\cot^2\theta$ and $\cos\theta\cot\theta$. As shown in Fig. 1A, the a parameter plots for both the Si and W samples are linear for values of $\cos^2\theta$ below 0.6, i.e. for Bragg angles greater than ~40 °θ. It was also observed that the direction of the deviation of the data points from a linear plot at lower Bragg angles is towards *higher a* parameter values. The available data points at Bragg angles greater than 40 °θ are spread fairly uniformly along the linear plot, but the lack of lesser error data points at $\cos^2\theta$ values below 0.16, *i.e.*, for Bragg angles above 66 °θ, will significantly reduce the accuracy of a lattice parameter derived by extrapolating the data to 90 °θ.

Plots of a parameters of the Si and W samples against $\cot^2\theta$, which are given in Fig. 1B, also show linear trends for Bragg angles greater than ~40 °θ. The lack of results for Bragg angles above 71 °θ is not so apparent in this plot, since $\cot^2\theta$ causes the data points to be bunched up in the high angle region, which makes this function less suitable for extrapolation purposes. In contrast to the $\cos^2\theta$ plot of the Si and W a parameter values, the direction of the deviation from a linear plot against $\cot^2\theta$ is towards *lower* values. This means that the magnitude of the angular function which governs the present experimental error in a parameters at low Bragg angles must be intermediate between the numerical values of $\cos^2\theta$ and $\cot^2\theta$.

The open symbol data points plotted against $\cos\theta\cot\theta$ in Fig. 2 refer to uncorrected a parameters of the samples of Si and W. The plots of these data are linear for values of $\cos\theta\cot\theta \leq 2.5$, i.e. for all Bragg angles greater than ~20 °θ, which covers almost the entire angular range of the present investigation (16-71 °θ). The extensive linearity of these $\cos\theta\cot\theta$ plots suggests that the prime source of systematic error in the present results is attributable to sample surface displacement. It also follows from the properties of trigonometric functions, that low angle data which conform to a linear $\cos\theta\cot\theta$ plot will show a deviation towards *higher* values when plotted against $\cos^2\theta$, and a deviation towards *lower* values when plotted against $\cot^2\theta$, as was observed for the data plotted in Figs. 1A and 1B.

The solid symbol data points in Fig. 2 refer to a parameters for Si and W samples which are corrected for flat specimen, effective transparency and axial divergence errors using the respective analytical functions, and instrumental and materials parameters, given in the experimental section. These corrections do not affect the linearity of the plots against $\cos\theta\cot\theta$, but cause a significant change in the slope of the Si plot, due to the magnitude of the transparency error correction for this low absorbent material. The change in slope results in a significantly difference in lattice parameter derived by extrapolation of the best least squares fit of the data to a linear plot, which gives 5.4317 Å and 5.4309 Å for the uncorrected and corrected data, respectively. The close similarity of the corrected data lattice parameter to the NIST accepted value of 5.43094(0) Å for Si SRM 640b (18), confirms the validity of the transparency correction based on 60 % of theoretical density. However, the extreme sensitivity observed for the transparency error with respect to the effective density of a powder sample means that the influence of this effect should be re-evaluated in the context of the use of small amounts of low absorbent materials as internal calibration standards for powder diffractometry.

In contrast to the results obtained for Si, the no significant change in slope was observed between the plots for uncorrected and corrected data points for W in Fig. 2 and there was no measurable difference in the extrapolated lattice parameters for the two sets of data. The

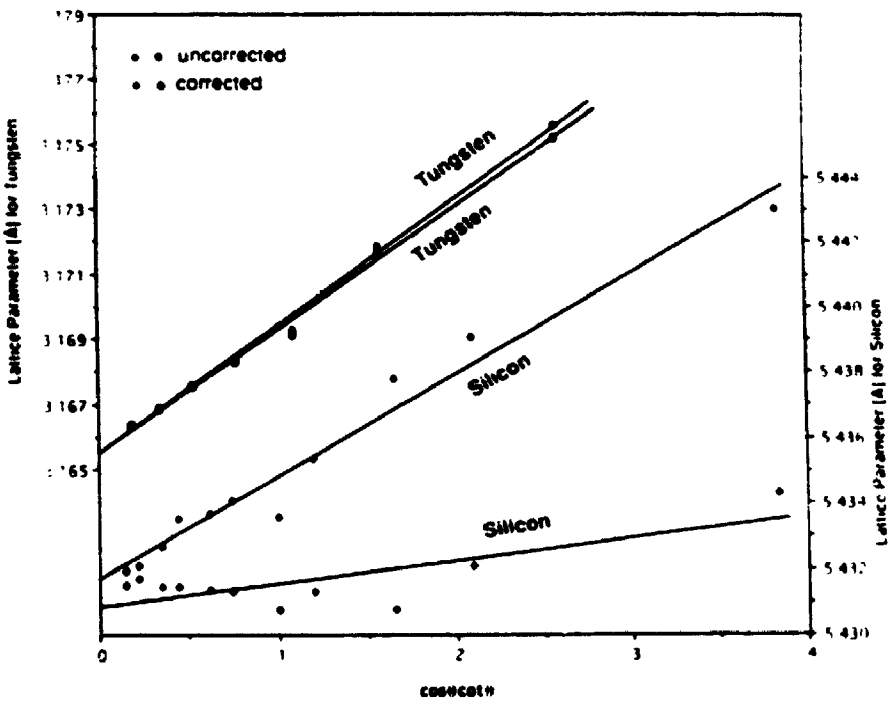

Fig. 2. Plots of uncorrected and corrected a-parameters of Si and W versus cosθcotθ.

extrapolated lattice parameter of $a = 3.1655$ Å is relatively close to the value of 3.1652(4) Å obtained by King and Russell (19), who eliminated scanning and sample displacement errors by measuring the total diffracted angle 4θ by scanning both sides of the beam. Exact agreement with other measurements is not to be expected as the purity of the W sample was not assessed, since the objective of the present experiment was to evaluate the influence of error functions rather than obtain precise lattice parameters by an extrapolation process. However, the almost

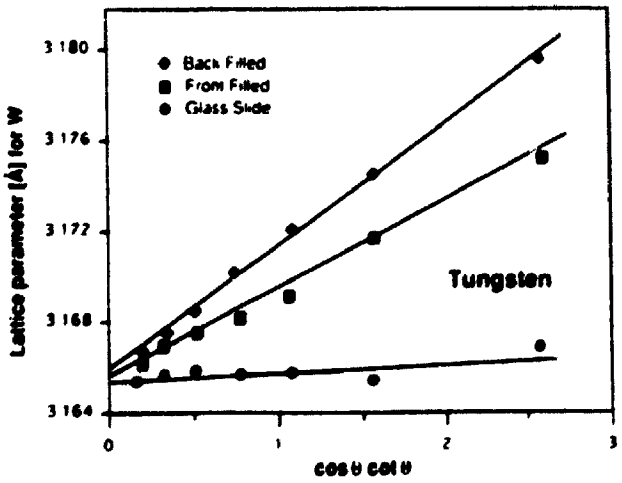

Fig. 3. Plots of corrected a parameters of W versus cosθcotθ for different sample mounts.

total absence of transparency errors in the results for the W sample in Fig. 2 means that small amounts of highly absorbent powders may prove to be more effective than low absorbent materials for use as internal standards for powder diffractometry, or perhaps the optimum solution is to use an internal standard with an absorption coefficient which is close to that of the sample under investigation.

Due to its relative insensitivity to the flat specimen, axial divergence and transparency errors, the tungsten powder was selected for further experiments on the effects of the sample displacement error. As shown in Fig. 3, plots of a parameter versus $\cos\theta\cot\theta$, using data corrected for flat specimen, effective transparency and axial divergence errors, have significantly different slopes for samples prepared by different mounting techniques. The positive slopes of these plots indicate that in all cases the surface of the sample is displaced outside the focusing circle. The minimum slope was observed for the powder sample prepared on a glass slide, while an intermediate slope was observed for the front filled cavity sample, and the greatest slope occurred for the sample prepared in the back filled sample mount covered with adhesive tape. In the context of the theta:theta geometry of the x-ray diffractometer, the sample prepared on the glass slide would be expected to lie above the reference plane of the specimen holder, but the small positive slope of the relevant plot in Fig. 3 indicates that the surface of the glass slide (and hence the reference surface of the goniometer) is in fact located just below the centre line of the x-ray beam when the tube and detector are set at zero $^\circ 2\theta$. In this event, the front-filled cavity sample would be displaced by the same amount below the centre line of the primary beam, to give a $\cos\theta\cot\theta$ plot with a positive slope. It also follows that under these conditions the $\cos\theta\cot\theta$ plot for the back-filled sample would have an even greater slope, because of the additional surface displacement introduced by the adhesive tape covering the surface of the sample.

The linearity of the plots of a parameter against $\cos\theta\cot\theta$ for W in Fig. 3 can be used to make corrections for specimen surface displacement errors under conditions where the position of the surface cannot be precisely aligned with respect to a defined reference, e.g. in a high temperature furnace or a low temperature cryostat. With prior calibration using known displacements of a cubic material, surface displacements that occur during an experiment can be detected by changes in the slope of a $\cos\theta\cot\theta$ plot using a parameters corrected for flat specimen, axial divergence and effective transparency. This information could also be used to adjust the position of the furnace or cryostat at a non-ambient temperature, so that the sample surface is positioned precisely on the focusing circle of the diffractometer, which will be evident when the $\cos\theta\cot\theta$ plot using corrected lattice parameters has a zero slope. After applying the corrections for transparency, flat specimen and axial divergence, and eliminating the major experimental error due to sample displacement, the random errors can then be eliminated by a least squares analysis, to yield accurate lattice parameters for applications such as thermal expansion investigations. This method for detecting and correcting sample displacements is, of course, only applicable to samples with high symmetry, but it could be most effective for locating and correcting the position of a ribbon heater made from Pt or another cubic material, which acts as a sample support for high temperature measurements. This error is very significant in x-ray furnaces, since heater strips are known to be susceptible to buckling at high temperatures. Under these conditions, a properly aligned heater strip could also be used as an internal standard, by making a proper allowance for the displacement of the centre of the powder sample from the heater surface. For these applications, it is fortuitous that the common heater strip materials are Pt, Re and W, all of which generate very small transparency errors, due to their high x-ray absorption coefficients.

Acknowledgments

This work was supported in part by an operating grant from the Natural Sciences and Engineering Research Council. The authors are also grateful to M.B. Stanley for assistance with the experiments, and to A. Chan, P. Gough, R. Govers, W. Mackwood, S. McIntyre, and J. Wallace for their helpful suggestions and comments.

References

1. L.F. Vassamillet and H.W. King, "Precision X-ray Diffractometry Using Powder Specimens", *Adv. X-ray Anal.*, 6 142-157 (1963).
2. W. A. Rachinger, "A Correction for the $\alpha_1\alpha_2$ Doublet in the Measurement of Widths of X-ray Diffraction Lines", *J. Sci. Instrum.*, 25 254-255 (1948).
3. A.J.C. Wilson, "Some Problems in the Definition of Wavelengths in X-ray Crystallography", *Z. Kristallogr.* 111 471-476 (1959).
4. E.R. Pike, "Counter-tube Diffractometer - The Effect of Dispersion, Lorentz and Polarization Factors on the Position of X-ray Powder Diffraction Lines in Terms of the Center of Gravity of the Lines", *Acta Crystallogr.*, 12 87-92 (1959) and 14 53-54 (1961).
5. J. Ladell, M. Mack, W. Parrish and J. Taylor, "Dispersion, Lorentz and Polarization Effects in the Centroid Method of Precision Lattice Parameter Determination", *Acta Crystallogr.*, 12 567-570 (1959).
6. W. Parrish and R.T. Kohler, "Use of Counter Tubes in X-ray Analysis", *Rev. Sci. Instrum.* 27 795-808 (1956).
7. A.J.C. Wilson, "Correction of Lattice Spacings for Refraction", *Proc. Camb. Phil. Soc.*, 36 485-489 (1940).
8. A.J.C. Wilson, "Effect of Absorption on the Mean Wavelength of X-ray Emission Lines", *Proc. Phys. Soc.*, (London), 72 924-925 (1958).
9. J. Cermak, "The Intensity Distribution in the Faces of Curved Crystals Monochromators and an Estimate of its Influence on Precision Measurements of Lattice Parameters", *Acta C ystallogr.*, 13 832-835 (1960).
10. J.A. Beardon, "X-ray Wavelengths", US Atomic Energy Commission, Division of Technical Information Extension, Oak Ridge TN, Publication NYO-10586 (1964).
11. W.L. Bond, "Precision Lattice Constant Determination", *Acta Crystallogr.*, 13 814-817 (1960).
12. E.R. Pike, "Counter-tube Diffractometer - The Effect of Vertical Divergence on the Displacement and Breadth of X-ray Powder Diffraction Lines", *J. Sci. Instr.*, 34 355-363 (1957) and 36 52-53 (1959).
13. W. Wong-Ng and C.R. Hubbard, "Standard Reference Materials for X-ray Diffracion Part II. Calibration using d-Spacing Standards", *Powder Diffraction*, 2 242-248 (1987)
14. H.P. Klug and L.F. Alexander, "X-ray Diffraction Procedures", 2nd Edn., Wiley-Interscience, New York, NY (1974) p.292.
15. E.R. Pike and A.J.C. Wilson, "Counter-tube Diffractometer - The Theory of the Use of Centroids of Diffraction Profiles for High Accuracy in the Measurement of Diffraction Angles", *Brit. J. Appl. Phys.*, 10 57-68 (1959).
16. L. E. Alexander, "The Synthesis of X-ray Spectrometer Line Profiles with Application to Crystallite Size Measurements" *J. Appl. Phys.*, 25 155-161 (1954).
17. A.J.C. Wilson, "Geiger-Counter X-ray Spectrometer - Influence of Size and Absorption Coefficient of Specimen on the Position and Shape of Powder Diffraction Maxima", *J. Sci. Instr.*, 27 321-325 (1950).
18. Standard Reference Materials for X-ray Powder Diffractometry, Office of Standard Reference Materials, National Institute for Standards and Technology, Gaithersburg, MD 20899.
19. H.W. King and C.M. Russell, "Double-Scanning Diffractometry in the Back-Reflection Region", *Adv. X-ray Anal.*, 8 1-10 (1965).

AN EXPERIMENTAL EVALUATION OF COMPUTATIONAL METHODS FOR DETERMINING LATTICE PARAMETERS USING BRAGG-BRENTANO POWDER DIFFRACTOMETRY

E.A. Payzant and H.W. King

Department of Materials Engineering
University of Western Ontario
London, ON, N6A 5B9
CANADA

ABSTRACT

Computational methods for determining precision lattice parameters based on extrapolation, lattice refinement, least squares and trial and error indexing, with intermediate corrections for peak positions using external and internal standards, have been evaluated with respect to the ICDD published values for zincite. Lattice parameters can be routinely determined to an accuracy of one part in ten thousand without the use of external or internal standards, by using computational extrapolation on data with a well aligned and maintained diffractometer. Lattice refinement determination of lattice parameters was only effective, with respect to the ICDD values, when used in conjunction with external and internal standards. Least squares yielded results with low standard deviations, but the use of standards did not reduce the refined sample displacement or zero angle errors, and gave an increased error in lattice parameters with respect to the ICDD values. The trial and error indexing, which can only be used with peak positions corrected with respect to both external and internal standards, gave relatively low deWolff and Smith-Snyder figures of merit, but nevertheless yielded lattice parameters of the highest accuracy of one part in twelve thousand, with respect to the ICDD values.

INTRODUCTION

Random errors in x-ray determinations of lattice parameters have $\cot\theta$ dependence regardless of the geometry of the method, but systematic errors due to geometry and experimental settings are specific to the technique employed. The significant systematic errors for the Bragg-Brentano powder diffractometer method are those which arise from: specimen surface displacement ($\propto \cos\theta\cot\theta$); flat specimen and horizontal divergence ($\propto\cot^2\theta$); and sample absorption and axial divergence ($\propto \cos^2\theta$) [1]. A recent study by the present authors has shown that although the analytical functions for all these errors converge to zero as θ approaches 90 °, linear plots of lattice parameters of test samples of silicon and tungsten against $\cos^2\theta$ and $\cot^2\theta$ were only obtained for Bragg angles greater ~40 °θ, while plots of the same data against $\cos\theta\cot\theta$ were linear over the entire experimental range from 16-71 °θ [1]. These findings for samples with widely different mass attenuation

Advances in X-Ray Analysis, Vol 37, Edited by
J.V. Gilfrich *et al*., Plenum Press, New York, 1994

coefficients indicate that, in the Bragg-Brentano method, the sample displacement error is more significant than the sample absorption error, which is the dominant factor in the Nelson-Riley function for the Debye-Scherrer method. Further, since its angular dependence is midway between the angular variation of $\cos^2\theta$ and $\cot^2\theta$, the function $\cos\theta\cot\theta$ can be used as an extrapolation function for determining precision lattice parameters, even when errors due to absorption, flat specimen and divergence are present [1]. The present paper represents an extension of this study to the evaluation of computational methods for deriving precision lattice parameters from Bragg peak positions using a variety of corrective techniques, including direct comparison to the standard materials characterized by NIST. For an extensive review of present computational methods and commercially available software, the reader is referred to reference [2].

EXPERIMENTAL

A 50:50 mixture of powdered silicon (NIST SRM640b) and zincite (sample from IUCr Commission on Crystallographic Apparatus, Precision Measurements of Lattice Parameters, Feb. 1957) was prepared as a "smear" sample on a plastic slide with silicone grease. Zincite was selected for this study, because the hexagonal crystal structure [3] yields a relatively large number of Bragg peaks when using CuK_α radiation ($\lambda_{CuK_{\alpha 1}}$ = 1.54058 Å) with very few overlaps with the silicon peaks. The hexagonal diffraction pattern of this sample was recorded with a Scintag XDS 2000 x-ray diffractometer set in the θ:θ mode with a 250 mm radius, a 1 mm divergent slit, a 0.3 mm receiving slit and a 0.03 ° step interval, to give an effective scanning speed of 1 °2/min. These settings are not optimized for precision peak measurement, but are fairly representative of settings for routine data acquisition. The prime interest of the present study was whether the different computer analysis methods would compute similar or different lattice parameters from the identical raw data set. The raw data obtained for the diffraction patterns were analyzed in three stages:

In stage one, the Scintag Background Subtraction Program was applied to remove both the background and the α_2 component (using the Rachinger correction [4]).

In stage two, the α_1 peak positions were determined by one of the four methods listed below:

NC No corrections. Peak positions were determined using a profile fitting program based on the Pearson VII function.

EC External standard correction. Using a peak finder program, the peak positions were corrected by comparison with the peaks of NIST silicon SRM640b prepared as a separate "smear" sample, which was step scanned at 2 sec/step with a 0.03 ° step interval. The measured peak positions were corrected to the NIST values by the 4th order polynomial correction function :

$$\Delta 2\theta = A + B(2\theta) + C(2\theta)^2 + D(2\theta)^3 + E(2\theta)^4 \qquad \text{(eqn. 1)}$$

Note: Once the parameters A, B, C, D, and E are determined from the calibration sample, this correction can be applied to any subsequent sample. The correction function involves no assumptions as to the nature of the errors in 2θ, but instrumental errors such as zero 2θ setting may be minimized. The program also models the FWHMs of the peaks as a function of angle, which is useful for other applications, but is not relevant to this study.

IC Internal standard correction. Using a peak finder program, the peak positions were corrected by comparison with the peaks corresponding to the NIST silicon SRM640b (certified lattice parameter a_o = 5.430940 ±0.000035 Å), which was mixed directly with the "smear" sample, to obtain a linear correction function based solely on the sample surface displacement error, $\Delta 2\theta = (S/R)\cos\theta$

EI Both external and internal corrections. Peak positions were determined using a peakfinder program in which first the external (EC) and then the internal (IC) standard corrections were applied.

In stage three, precision lattice parameters were computed from the various uncorrected and corrected values of peak positions, using each of the methods listed below:

EX Extrapolation. A computational method equivalent to graphical extrapolation [1], based on the technique described by Vogel and Kempter [5]. The program requires prior knowledge of the structure (but not the space group) and all of the peaks must be indexed prior to running the program. Lattice parameters were determined using the error function $\cos\theta\cot\theta$ to correct for sample surface displacement, and the drift constant, K_0, was calculated [5]. The version of the program included an internal standard correction option which was not used in the present evaluation.

LR Lattice Refinement. A commercial program [Scintag, Inc.] for either indexing and/or lattice refinement. Lattice parameter refinement requires a knowledge of the structure, but not the space group, and all of the peaks must be indexed prior to running this program option. Since no systematic errors are eliminated, the results are very sensitive to sample surface displacement and transparency errors.

LS Least Squares. A software program LCLSQ (version 8.4), by C.W. Burnham [6], which refines the lattice parameters. It requires a knowledge of the both the sample structure and the space group, and all of the peaks must be indexed prior to running program. The program allows refinement of relevant systematic errors in addition to lattice parameters, and also computes the Smith-Snyder [7] figure of merit, F_N.

TR Treor. A software program TREOR90, by P.-E. Werner [8], for trial and error indexing, which requires a precision of $\leq 0.02°$ in peak position. The program refines lattice parameters, and gives both conventional figures of merit [7,9], M_N and F_N, but as it does not allow refinement of systematic errors it could only be used with the peak position data corrected with respect to external and internal standards (EI).

RESULTS AND DISCUSSION

All four computational techniques were evaluated, for the different 2θ correction methods, by comparing the lattice parameters determined for zincite with the average values of $a_0 = 3.249858 \pm 0.000006$ Å and $c_0 = 5.206619 \pm 0.000002$Å found in the ICDD cardfile [2]. While these values are not necessarily the "correct" values for our sample, they provide a convenient reference standard with which to compare our results. Additional parameters specific to each technique were also used in the evaluation, including the drift constant K_0 for EX, the estimated standard deviation (esd) for LR, the Smith-Snyder figure of merit (F_N) for LS and TR, and the deWolff figure of merit (M_N) for TR. The LS technique also provided estimates of the sample displacement and zero angle errors. For convenience and clarity of presentation, the results obtained for each of the computational techniques are presented in separate tables, and combined in Figures 1 and 2.

As shown in Table 1, the extrapolation method based on the function $\cos\theta\cot\theta$ yielded lattice parameters of zincite to an accuracy of one part in eight thousand, when no correction was applied to the peak positions (EX-NC). This accuracy was marginally improved, to one part in eleven thousand, by the use of an external standard (EX-EC) which corrected for "instrumental errors". The use of an internal standard (EX-IC) gave no improvement in accuracy, which is to be expected since this method is redundant as it corrects for sample surface displacement errors which are minimized by the $\cos\theta\cot\theta$ extrapolation. The use of both internal and external standard corrections was found to be counterproductive, as it

Table 1. Extrapolation Technique (EX)

2θ Correction	Lattice Parameter Accuracy (vs. ICDD value)	Drift Constant K_o
EX-NC	Δa_o = 0.0004 Δc_o = 0.0008	.0041
EX-EC (SRM640b)	Δa_o = 0.0003 Δc_o = 0.0002	.0012
EX-IC (SRM640b)	Δa_o = 0.0005 Δc_o = 0.0008	.0001
EX-EI	Δa_o = 0.0004 Δc_o = 0.0027	.0008

introduces a greater error, particularly in the c_o spacing. The main drawback to the computational technique (EX) is that it cannot be applied to crystal systems of low symmetry, such as monoclinic or triclinic.

As shown in Table 2, the Scintag lattice refinement program (LR) yielded lattice parameters with the relatively low accuracy of one part in sixteen hundred without the use of 2θ corrections (LR-NC). This accuracy was improved to one part in five thousand when the 2θ positions were corrected by using external or external standards, and to one part in nine thousand when both corrections were applied. Even so, this level of accuracy is not much better than that obtained by the extrapolation technique (EX-NC) without the use of standards.

As shown in Table 3, the least squares program (LS-NC) yielded refined lattice parameters with an apparent high accuracy, as indicated by the high Smith-Snyder figure of merit, and provided estimates of the magnitude of the sample displacement and zero angle errors. However, the accuracy of one part in three thousand compared to the ICDD lattice

Table 2. Lattice Refinement Technique (LR)

2θ Correction	Lattice Parameter Accuracy (vs ICDD value)	Estimated Accuracy (from esd)
LR-NC	Δa_o = 0.00199 Δc_o = 0.00257	.0005 .0009
LR-EC (SRM640b)	Δa_o = 0.00079 Δc_o = 0.00087	.0010 .0014
LR-IC (SRM640b)	Δa_o = 0.00051 Δc_o = 0.00077	.0001 .0002
LR-EI	Δa_o = 0.00035 Δc_o = 0.00057	.0001 .0002

Table 3. Least Squares Technique (LS)

2θ Correction	Parameter Accuracy (vs. ICDD value)	Systematic Error Refinement	Smith-Snyder Figure of Merit
LS-NC	Δa_o = 0.0010 Δc_o = 0.0017	S = -0.416 mm zero 2θ = -0.074°	F(23) = 233 (0.004,28)
LS-EC (SRM640b)	Δa_o = 0.0025 Δc_o = 0.0033	S = -0.660 mm zero 2θ = -0.268°	F(22) = 69 (0.011,28)
LS-IC (SRM640b)	Δa_o = 0.0017 Δc_o = 0.0026	S = -0.295 mm zero 2θ = -0.142°	F(24) = 103 (0.008,28)
LS-EI	Δa_o = 0.0026 Δc_o = 0.0040	S = -0.574 mm zero 2θ = -0.272°	F(23) = 96 (0.009,28)

parameter values is significantly lower than that obtained for the extrapolation method without the use of standards (EX-NC). Further, although the systematic error refinement capability of the LS program is intended to limit the need for standards, an internal standard correction only reduced the refined sample displacement error to 295 μm from 416 μm, while an external standard correction actually increased the refined zero 2θ errors. In both cases the Smith-Snyder figure of merit was decreased, and poorer agreement was obtained with respect to the ICDD lattice parameter values. Since neither a sample transparency error nor an axial divergence error could be refined by this method, these errors were fixed at zero by the program.

As shown in Table 4, the TREOR program applied to data corrected with respect to both external and internal standards (TR-EI) yielded a relatively low Smith-Snyder figure of merit, but an accuracy of one part in twelve thousand for lattice parameters compared to the ICDD lattice parameter values. The accuracy of the latter result is greater than that achieved with the extrapolation program with no 2θ corrections (EX-NC) and represents the highest accuracy of obtained for any method in this evaluation. However, as cautioned by Werner [8], the successful operation of the indexing program TREOR90 requires reliable input data, and the use of external and internal standards is thus recommended in order to obtain peak positions of sufficient accuracy.

Differences between the calculated lattice parameters and the ICDD values are less important in this study as compared to the dependence of the calculated lattice parameters on the computational method. Thus, the "correct" lattice parameter of our sample may not be equivalent to the ICDD value, but must be consistent for all the data presented here, since the raw data were identical. As may be seen from the plots of lattice parameters a_o and c_o given in Figures 1 and 2, the extrapolation methods EX-NC, EX-EC, and EX-IC all yielded comparable lattice parameters to within ±0.0003 Å. Similarly the LR-EC, LR-IC, LR-EI, and the TR-EI all agree to within the same scatter as the EX results. For the LCLSQ program, the best agreement with the other methods was obtained with no correction applied to the raw data, LS-NC.

Table 4. TREOR Technique (TR)

2θ Correction	Parameter Accuracy (vs. ICDD value)	de Wolff Figure of Merit	Smith-Snyder Figure of Merit
TR-EI	Δa_o = 0.00026 Δc_o = 0.00052	M(20) = 346	F(23) = 75 (0.0091,34)

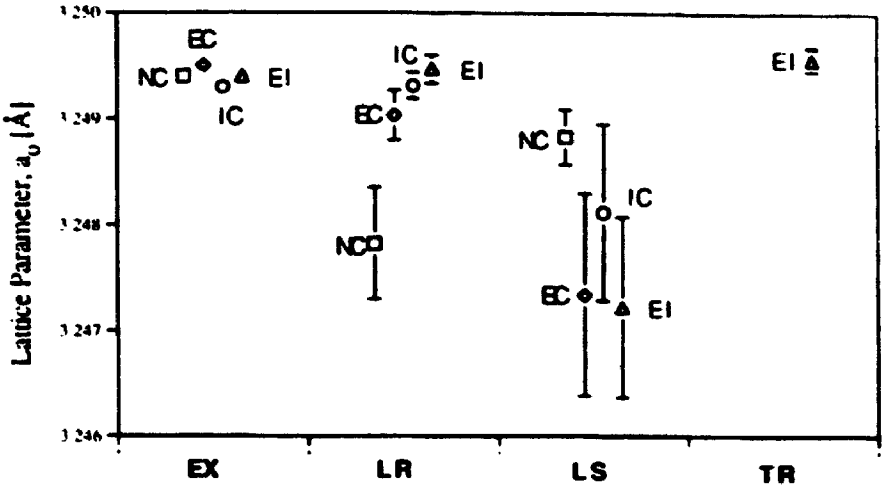

Figure 1. Lattice parameter a_0 as calculated by the four programs (EX, LR, LS, and TR). The error bars represent the estimated standard deviation as calculated by the respective program. The codes NC, EC, IC, and EI may be found in the text.

The overall finding of the present evaluation of various computational techniques is that, for a reasonably well-aligned and maintained diffractometer, lattice parameters can be routinely determined to an accuracy of better than one part in ten thousand by using a computational extrapolation method based on the function $\cos\theta\cot\theta$, without the use of internal and/or external standards, particularly fine slits or slow scanning speeds. An external standard is shown to be effective for eliminating zero 2θ errors, which may be present in a poorly aligned instrument.

On the basis of these results, the use of external and/or internal corrections with an extrapolation-based method, or a least-squares method which refines systematic errors (such as LCLSQ), is not recommended. However, for a least-squares method which does

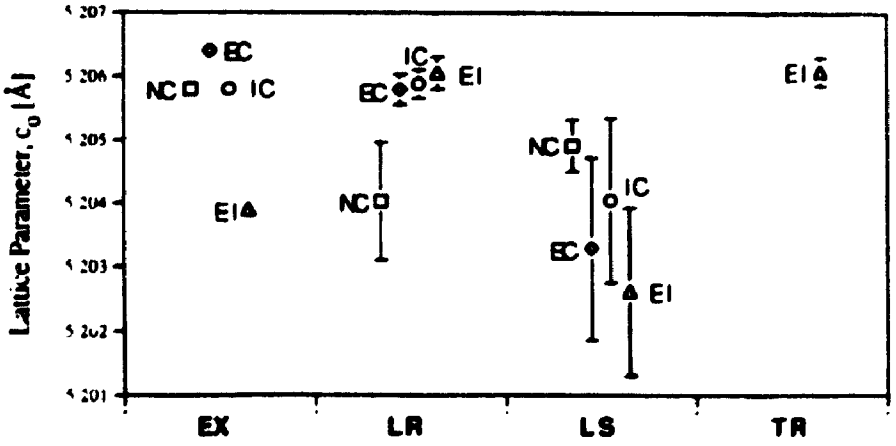

Figure 2. Lattice parameter c_0 as calculated by the four programs (EX, LR, LS, and TR). The error bars represent the estimated standard deviation as calculated by the respective program. The codes NC, EC, IC, and EI may be found in the text.

not refine systematic errors (such as the LR program) use of an internal correction is strongly recommended, and with TREOR90 our experience is that both an internal and external correction is usually required.

Acknowledgment

This work was supported in part by a grant from the Natural Sciences and Engineering Research Council of Canada.

REFERENCES

1. H.W. King and E.A. Payzant, "An Experimental Evaluation of Error Functions for Bragg-Brentano Diffractometry", *Adv. X-Ray Analysis*, **36** 663-670 (1993).
2. D.K. Smith, "Computer Analysis of Diffraction Data", in *Modern Powder Diffraction*, Reviews in Mineralogy Vol. 20, Mineralogical Soc. of America, Washington, DC (1989).
3. S.C. Abrahams and J.L. Bernstein, "Remeasurement of the Structure of Hexagonal ZnO", *Acta Cryst.*, **B25** 1233-1236 (1969).
4. W.A. Rachinger, "A Correction for the $\alpha_1\alpha_2$ Doublet in the Measurement of Widths of X-ray Diffraction Lines", *J. Sci. Instrum.*, **25** 254-255 (1948).
5. R.E. Vogel and C.P. Kempter, "A Mathematical Technique for the Precision Determination of Lattice Parameters", *Acta Cryst.*, **14**, 1130-1134 (1961).
6. C.W. Burnham, "Lattice Constant Refinement", *Carnegie Inst. of Washington Yearbook*, **61** 132-135 (1962).
7. C.W. Burnham, "Refinement of Lattice Parameters Using Systematic Correction Terms", *Carnegie Inst of Washington Yearbook*, **64** 200-202 (1965).
8. G.S. Smith and R.L. Snyder, "F_N: A Criterion for Rating Powder Diffraction Patterns and Evaluating the Reliability of Powder-Pattern Indexing", *J. Appl. Cryst.*, **12**, 60-65 (1979).
9. P.-E. Werner, L. Eriksson and M. Westdahl "TREOR, a Semi-Exhaustive Trial-and-Error Powder Indexing Program for All Symmetries", *J Appl. Cryst.*, **18**, 367-370 (1985).
10. P.M. de Wolff, "A Simplified Criterion for the Reliability of a Powder Pattern Indexing", *J Appl Cryst.*, **1**, 108-113 (1968).

REFERENCES

1 A. Laarif and F. Theobald, "The Lone Pair Concept and the Conductivity of Bismuth Oxides Bi_2O_3", *Solid State Ionics*, **21** (1986) 183-193

2 L.G. Sillén and B. Aurivillius, "Mischoxydphasen mit unvollständigem Sauerstoffgitter", *Die Naturwissenschaften*, **27** (1939) 388-389

3 L.G. Sillén and B. Aurivillius, "Oxide Phases with a Defect Oxygen Lattice", *Zeit. Krist.*, **101** (1939) 483-495

4 B. Aurivillius, "An X-ray investigation of the systems $CaO-Bi_2O_3$, $SrO-Bi_2O_3$ and $BaO-Bi_2O_3$-O. (Mixed oxides with a defect oxygen lattice.)", *Arkiv för Kemi, Mineralogi och Geologi*, **16A** [17] (1943) 1-13

5 P. Conflant, J.-C. Boivin, and D. Thomas, "Etude structurale du conducteur anionique $Bi_{0,765}Sr_{0,235}O_{1,383}$", *J. Solid State Chem.*, **35** (1980) 192-199

6 R.J.D. Tilley, "An Electron Microscope Study of the Rhombohedral Phase Occurring in the Bi_2O_3-BaO System", *J. Solid State Chem.*, **41** (1982) 233-243

7 S.K. Blower and C. Greaves, "A Neutron Diffraction Study of $Ca_{.176}Bi_{.824}O_{1.412}$", *Mater. Res. Bull.*, **23** (1988) 765-772

8 P. Conflant, J.-C. Boivin, and G. Tridot, "Les composés définis du système Bi_2O_3-CaO", *C. R. Acad. Sc. Paris*, **279** (1974) 457-460

9 P. Conflant, J.-C. Boivin, and D. Thomas, "Le Diagramme des Phases Solides du Systeme Bi_2O_3-CaO", *J. Solid State Chem.*, **18** (1976) 133-140

10 R. Guillermo, P. Conflant, J.-C. Boivin, and D. Thomas, "Le diagramme des phases solides du système Bi_2O_3-SrO", *Revue de Chimie minérale*, **15** (1978) 153-159

11 J.-C. Boivin, and D. Thomas, "Structural Investigations on Bismuth-Based Mixed Oxides", *Solid State Ionics*, **3/4** (1981) 457-462

12 J.-C. Boivin and D. Thomas, "Crystal Chemistry and Electrical Properties of Bismuth-Based Mixed Oxides", *Solid State Ionics*, **5** (1981) 523-526

13 P. Conflant, J.-C. Boivin, G. Nowagrocki, and D. Thomas, "Etude structurale par diffractometrie X à haute temperature du conducteur anionique $Bi_{0,844}Ba_{0,156}O_{1,422}$", *Solid State Ionics*, **9/10** (1983) 925-928

14 R.D. Shannon and C.T. Prewitt, "Effective Ionic Radii in Oxides and Fluorides", *Acta Cryst.*, **B25** (1969) 925-946

15 A.D. Neuimin, L.D. Yushina, Y.M. Ovchinnikov, and S.F. Pal'guev, "Nature of the Electrical Conductivity of Solid Solutions of Bi_2O_3-SrO", *Electrochemistry of Molten and Solid Electrolytes*, **2** (1964) 92-96
originally published in Russian as:
Tr. Inst. Ehlektrokhimii Akad. Nauk SSSR Ural'skij Filial, **4** (1963) 111-115

16 T. Takahashi, H. Iwara, and Y. Nagai, "High oxide ion conduction in sintered Bi_2O_3 containing SrO, CaO or La_2O_3", *J. Appl. Electrochem.*, **2** (1972) 97-104

17 T. Takahashi, T. Esaka, and H. Iwara, "Electrical Conduction in the Sintered Oxides of the System Bi_2O_3-BaO", *J. Solid State Chem.*, **16** (1976) 317-323

18 E.M. Levin and R.S. Roth, "Polymorphism of Bismuth Sesquioxide. II. Effect of Oxide Additions on the Polymorphism of Bi_2O_3", *J. Res. NBS - A.. Physics and Chemistry*, **68A** (1964) 197-206

19 N.M. Hwang, R.S. Roth, and C.J. Rawn, "Phase Equilibria in the Systems SrO-CuO and SrO-$1/2Bi_2O_3$", *J. Am. Ceram. Soc.*, **73** (1990) 2531-2533

20 R.S. Roth, C.J. Rawn, B.P. Burton, and F. Beech, "Phase Equilibria and Crystal Chemistry in the Systems SrO-CaO-Bi_2O_3-CuO, Part II - The System SrO-Bi_2O_3-CuO", *J. Res. Natl. Inst. Stand. Technol.*, **95** (1990) 291-335

21 A. Watanabe, "Phase Stability of $Bi_{0.76}Sr_{0.235}O_{1.383}$-Type Bismuth Mixed Oxides With Hexagonal Symmetry", *Solid State Ionics*, 35 (1989) 281-283

22 A. Watanabe and T. Kikuchi, "Cubic-Hexagonal Transformation of Yttria-Stabilized δ-Bismuth Sesquioxide, $Bi_{2-2x}Y_{2x}O_3$ (x = 0.215 - 0.235)", *Solid State Ionics*, 21 (1986) 287-291

23 K.Z. Fung, A.V. Virkar, and D.L. Drobeck, "Massive Transformation in the Y_2O_3-Bi_2O_3 System", *J. Am. Ceram. Soc.*, 77 (1994) 1638-1648

22 J.A. Kilner and J.D. Faktor, "Anion Conductivity in Oxides with the Fluorite and Related Structures", in *Progress in Solid State Electrolytes* [T.A. Wheat, A. Ahmad, A.K. Kuriakose, eds.] Energy, Mines and Resources Canada, Ottawa (1983) 347-390

23 B. Cales and A.M. Anthony, "Fluorite-Type Solid Electrolytes as Oxygen Ion and Mixed Conductors", in *Progress in Solid State Electrolytes* [T.A. Wheat, A. Ahmad, A.K. Kuriakose, eds.] Energy, Mines and Resources Canada, Ottawa (1983) 413-439